Title
Xenon-based Molecular Sensors in Analytical Applications

Author
Meldrum, Tyler

Publication Date
2011

Peer reviewed|Thesis/dissertation

Xenon-based Molecular Sensors in Analytical Applications

by

Tyler Kenneth Meldrum

A dissertation submitted in partial satisfaction of the
requirements for the degree of
Doctor of Philosophy

in

Chemistry

in the

GRADUATE DIVISION
of the
UNIVERSITY OF CALIFORNIA, BERKELEY

Committee in charge:
Professor Alexander Pines, Chair
Professor David E. Wemmer
Professor Steven Conolly

Spring 2011

Xenon-based Molecular Sensors in Analytical Applications

Abstract

Xenon-based Molecular Sensors in Analytical Applications

by

Tyler Kenneth Meldrum

Doctor of Philosophy in Chemistry

University of California, Berkeley

Professor Alexander Pines, Chair

The development of xenon-based molecular sensors over the past decade has traditionally pointed toward applications in clinical diagnostics, with an emphasis on targeted molecular imaging using molecular sensors as a switchable contrast agent. While this would be a tremendous boon to medical physics, the potential for xenon-based MR contrast agents in analytical applications should not be understated. The phenomenal chemical shift range of xenon, dependent both on its chemical as well as its physical environment, coupled with its solubility and hyperpolarizability, makes xenon an excellent candidate for extracting information about a system of interest using NMR on optically opaque, unrefined samples.

To effectively use xenon-based molecular sensors in analytical applications, several changes are necessary to typical experimental protocols. To optimize the detection of xenon in samples containing little analyte, modifications to the Hyper-CEST [1] detection scheme are employed to improve magnetization transfer while simultaneously controlling more precisely the saturation bandwidth and power. These saturation sequences, demonstrated here as a series of d-SNOB shaped pulses, are used in both imaging and spectroscopic modalities, the latter enabling detection of extremely low concentrations of contrast agent.

Xenon-based analysis of biological materials depends on understanding the interactions between the contrast agents, a modified cryptophane cage, and lipids. The interaction of such contrast agents with lipid suspensions is characterized, including the response of both a Xe_{aq} signal and a Xe@cage signal to the lipid concentration, as well as discernible changes in both signals as a result of temperature changes. Furthermore, the selective detection of $Xe@cage_{aq}$ and $Xe@cage_{lipid}$ is demonstrated in both spectroscopic and imaging modes.

In addition, the general temperature response of xenon-based molecular sensors in aqueous solutions is characterized. Because the Hyper-CEST detection scheme relies on exchange of xenon with the contrast agent, controlling the flux through the agent dramatically affects the signal. At increased temperatures (37–40 $^{\circ}C$), analyte can be detected at concentrations much lower than is possible at room temperature. Also, the frequency dependence of the MR signal on temperature is characterized, with the response of xenon in a molecular sensor approximately ten-fold greater than xenon without a molecular sensor, and even more sensitive than the temperature response of protons—the temperature of a sample can be monitored with a resolution of approximately 0.5 K with this approach.

Lastly, the development of a molecular sensor scaffold, termed MS2CA and constructed by conjugating over 100 copies of a cryptophane cage to the interior of a viral capsid, enables dramatically enhanced sensitivity when working with xenon-based contrast agents. By employing the techniques described above, including optimized saturation transfer methods and elevated temperature, MS2CA contrast agents can be detected at 700 fM—far less agent than when using most other MR contrast agents. Furthermore, the MS2CA scaffold allows for increased solubility of the contrast agent in aqueous solutions. The sensitivity limit of this contrast agent is sufficient to detect even trace compounds in a mixture.

The incorporation of all of these developments in xenon-based molecular sensing may lead to integrated MR devices, capable of screening for bulk physiochemical properties of a sample, rather than the identification of unique compounds. Such devices may potentially be miniaturized and operated a low magnetic fields, further increasing the availability and affordability of such analysis using magnetic resonance.

To Juliana Boerio-Goates and Brian Woodfield, for taking a chance on a bright-eyed, would-be physician.

Contents

List of Figures

List of Tables

Acknowledgments

Making acknowledgements in a work whose development has lasted for approximately 17% of my life seems to require acknowledging approximately 17% of the people whom I have had the privilege to know and work and live with—a daunting and numerically impractical task.

Thanks to AP and DEW, two invaluable advisors who have supported me in ways far beyond science and funding. I couldn't have chosen a better lab to work in, nor better scientists and friends to work with. Thanks to AMJ for getting me on my feet when I knew nothing about the lab, and for being understanding when I discovered how much fun it can be to buy science toys. Thanks also to my collaborators, MBF and his crew, including KKP, KLS, LW, and PDG, who have deepened the scientific content of my research immeasurably. And, of course, the myriad Pinenuts who have been a part of my life for so long—I expect our relationships will last longer than our science will be relevant. In particular, I want to thank LS for getting us all going. I'll always reserve the first week of April for the most valuable scientific discoveries. Also, explicit recognition of MAS, DMG, NHM, TZT, FS, VSB, MHD, TJL, TKS, and XZ is appropriate, for their scientific prowess and for disproving the stereotype that scientists are nerds.

Though the time spent on this research was spent mostly in Stanley and Hildebrand, it's the time spent outside of those buildings that has made the end product feasible. Two phenomenal wards have sustained me through the best and the worst of it, and I would fail if I tried to enumerate specific individuals. Special thanks to MMM and PBM, who, by my estimation, have provided approximately 4.5×10^7 J of energy toward this thesis, while only burning roughly 2.5×10^6 J with Agricola.[1] Thanks to LDM and JRM for letting Agricola proceed without too much chagrin.

My family has inspired and supported me tirelessly, never more so than by championing me as I embarked on a crazy adventure to a crazy place to do crazy science. KWM and BFM, I can't thank you enough. I guess it's a love that transcends thanks, so I'll let it do just that. And to the other Ms, EW, JT, AJ, and BG: the world is so much better because of you. Thanks for making your lives a part of mine.

Many thanks and deepest love to my wife, SB, who constantly finds herself as the subject of my continual experiments in patience-trying and button-pushing. I couldn't do what I do without her, nor would I want to try.

[1] These values are entirely fabricated.

Chapter 1

Introduction

> "Why just NMR? Because there is hardly another technique that is so informative for so many different types of applications, and because there is no other technique that provides so much fun."
> —Richard R. Ernst, 1992

In the interest of complete and full disclosure, before introducing what this dissertation will be, it is important to clarify that this dissertation will *not* be a primer on nuclear magnetic resonance (NMR). While understanding this dissertation will require the reader to understand the fundamental principles of NMR, this thesis will only those principles of NMR that are particular to this research. From the largely pictorial overview by Blümich [2], to introductory texts by Levitt [3] and Nishimura [4], to more advanced texts by Cavanaugh [5], Ernst and Bodenhausen [6], Slichter [7], and Abragam [8], there is an abundance of material to study NMR—the reader is referred to these works to learn or revisit necessary topics.

This dissertation will introduce the reader to NMR done with xenon as the nucleus of interest. In particular, Chapter 2 will briefly detail the history of xenon in NMR and MRI, then discuss chemical and physical properties of xenon that are relevant to NMR. Importantly, Section 2.3 will discuss hyperpolarization, a technique whereby the NMR signal of xenon can be enhanced sufficiently for detection in the experiments described here. Chapter 3 will then discuss the interactions of xenon with cryptophanes, small organic cage molecules that interact reversibly with xenon; these cages are routinely incorporated into xenon-based molecular sensors, often called *sensors, biosensors,* or *molecular sensors,* used extensively in the research described here.

Chapter 4 will provide more background relevant to xenon NMR, including chemical exchange saturation transfer (CEST), a method for indirect detection

of NMR signals, and its extension to hyperpolarized (hp) nuclei, Hyper-CEST [1]. Some developments that improve the detection sensitivity and selectivity of Hyper-CEST detection will be detailed in Section 4.2.

The remaining chapters of this dissertation will discuss developments to xenon-based molecular sensors relevant to analytical applications; this work does not encompass *in vivo* studies. Aspects of molecular sensors pertinent to analytical applications that will be discussed here include the use of such sensors in lipid environments (Chapter 5), and harnessing temperature to improve sensitivity in both imaging (Chapter 6) and spectroscopic (Chapter 7) applications. Chapter 8 will discuss the development of a sensor consisting of the coat protein of a viral capsid with many cryptophane molecules carried as the payload of one sensor unit. This sensor scaffold has reduced the detection threshold for xenon NMR to sub-picomolar levels, a first for MR contrast agents. Lastly, Chapter 9 explores future applications of xenon-based molecular sensors to chemical analysis and microfluidic NMR applications.

Chapter 2

History and Physical Properties of Xenon

> "The separation of the xenon from traces of krypton proved to be more tedious than difficult..."
> —Sir William Ramsay, 1901

2.1 History of Xenon in NMR

In 1898, after a process he described as "more tedious than difficult," Sir William Ramsay successfully separated xenon (from the Greek $\xi\varepsilon\nu\phi\varsigma$ [*xenos*], meaning "strange") from krypton [9]. Before its use medically, xenon was used in flash lamps, generating short (1–2 μs) pulses of light for use in high-speed photography [10]. Beginning in 1939, the anesthetic properties of xenon were deduced, as Albert Behnke, a physician in the U.S. Navy, observed that changing the concentration of xenon and other gases in air could make deep-sea divers perceive depth changes. Though his and others' early works on xenon anesthesia were not published [11], in 1946 J. H. Lawrence published his studies on xenon anesthesia on mice [12], and in 1951 Stuart C. Cullen successfully operated on two patients under xenon-induced anesthesia [13].[1] These scientists demonstrated the safety and biocompatibility of xenon, adding it to a repertoire of compounds for clinical use.

While magnetic resonance imaging (MRI), invented by Lauterbur in 1973 [15], facilitates excellent clinical imaging of tissues where proton spin density

[1] Lest the reader worry over the safety of the author, concentrations of xenon above 35% are necessary to induce total anesthesia [14]. The experiments described here use a maximum xenon concentration of 2%.

is high, using MRI to image void spaces, such as the lungs, is not amenable to proton-based MRI. The first demonstration of pulmonary void-space imaging was done by Albert et al. [16] who used hp-^{129}Xe to image an excised mouse lung. Subsequently, pulmonary imaging with MRI was done primarily with ^{3}He, owing to its higher spin polarization, larger magnetic moment, longer relaxation times, and its lack of anesthetic properties, enabling higher concentrations *in vivo* before the onset of catalepsy. However, the primary source of ^{3}He is the decay of tritium (^{3}H), generated for the production of thermonuclear weapons. As production of such weapons has dwindled in recent years, there is now a global shortage of ^{3}He: less than 1000 kg were available in 2001 [17]. Unsurprisingly, this has resulted in a dramatic increase in the cost of ^{3}He, making ^{3}He up to sixty times more expensive than xenon.[2]

Beyond cost and availability, xenon-based NMR offers several advantages over its helium-based counterpart. As just mentioned, ^{3}He is only 0.000 137% of naturally occuring helium, while the NMR-active nucleus ^{129}Xe comprises 26.4% of natural abundance xenon [19]. Though both helium and xenon are gases at room temperature and one atmosphere pressure, the liquid and solid phases of xenon, unlike those of helium, are experimentally accessible without needing specialized equipment. Unlike helium, xenon is soluble in water, with an Ostwald solubility coefficient of 0.11 at $T = 25\,^{\circ}\mathrm{C}$ [20].[3]Moreover, owing to its highly polarizable electron cloud, xenon is strongly hydrophobic, dissolving readily in lipids and other organic solvents. The same polarizability of its electron cloud imparts a huge chemical shift range to xenon: several thousand parts per million (ppm) in xenon-halide compounds, and up to 250 ppm from solvent effects alone. The xenon solubility and chemical shift range will be addressed in greater detail in Sections 2.2 and 2.5, respectively.

2.2 Solubility of Xenon

Because the intensity of the NMR signal is dependent on the spin density, knowing the concentration of NMR-active spins in the sample is necessary for quantitative analysis of the spectra. In particular, for xenon-NMR involving cryptophane-based sensors, the concentrations of both xenon and sensor in solution significantly affect the signal. Solubility constants used to calculate

[2]In June 2009, the Pines lab purchased natural abundance xenon from Airgas, Inc. for approximately $17 per liter, while ^{3}He can cost up to $1000 per liter, according to [18].

[3]The Ostwald solubility indicates the volume of a gas that dissolves into one unit volume of liquid at a given temperature. Hence, at 25 °C and 1 atm pressure, 110 mL of xenon will dissolve into 1 L of water.

the concentration of xenon in a variety of liquids are provided in Table 2.1. Representative experimental conditions for experiments in this thesis are a 2% xenon gas mixture at 60 psi, with water as the solvent. Under those conditions, and assuming that xenon is an ideal gas, the dissolved xenon concentration $[\mathrm{Xe_{aq}}] = 367\,\mu\mathrm{M}$.

Beyond water, the most commonly used solvents for the experiments described here are benzyl alcohol ($\mathrm{C_7H_8O}$) and lipid suspensions. While the Ostwald solubility coefficient of xenon in benzyl alcohol is undetermined (though it is larger than that of xenon in water), the solubility of xenon in some lipid suspensions has been determined, as shown in Table 2.1. For the range of 0–30% lipid content (w/v), the Ostwald solubility coefficient can be approximated by the linear function:

$$\text{Ostwald solubility} = 0.1 + 0.016 \times (\%\text{ lipid content}). \tag{2.1}$$

2.3 Nuclear Hyperpolarization

Where major spectroscopic techniques are concerned, it is easy to see why NMR is considered insensitive. While electronic, vibrational, and rotational transitions of atoms and molecules occur with energies roughly corresponding to ultraviolet (10^7 MHz), visible (10^6 MHz), and infrared (10^4 MHz) light, transitions between spin states of nuclei have radiofrequency (rf) energies of tens to hundreds of megahertz (MHz). As spectroscopic sensitivity improves with increasing frequency, NMR is limited by the very nature of the probe. The energy (E) of a nucleus in an external magnetic field is given by $E = -m\hbar\gamma B_0$, where m is the magnetic quantum number ($\pm\frac{1}{2}$ for NMR), $\hbar$ has the usual value, B_0 is the strength of the externally applied magnetic field, and γ is the gyromagnetic ratio, an intrinsic property of the spin of interest. For ^{129}Xe, the nucleus most relevant to this research, the gyromagnetic ratio is -11.777 MHz/T.

The populations of spins in different energy levels are determined by the Boltzmann distribution, a ratio of the energy of a particular energy level to the thermal energy available to the system, k_BT, where k_B is the Boltzmann constant and T is the absolute temperature. For a two-level system, as with NMR, the ratio of spins up ($m = +\frac{1}{2}$, or $\uparrow$) to spins down ($m = -\frac{1}{2}$, or $\downarrow$) takes

Table 2.1: Solubilities of xenon in various liquids. The Ostwald solubility indicates the volume of a gas that dissolves into one unit volume of liquid at a given temperature.

Liquid	Ostwald solubility	Reference
$T = 25\,^{\circ}\mathrm{C}$		
water (H_2O)	0.11	[20]
hexane (C_6H_{14})	4.8	[20]
benzene (C_6H_6)	3.1	[20]
fluorobenzene (C_6F_6)	3.3	[20]
carbon disulfide (CS_2)	4.2	[20]
dimethylsulfoxide (DMSO)	0.66	[20]
$T = 37\,^{\circ}\mathrm{C}$		
water (H_2O)	0.0834	[21]
0.9% NaCl saline	0.09	[21]
blood plasma	0.10	[20]
erythrocytes (98%)	0.20	[20]
human albumin ($200\,\mathrm{g^{-1}\,L^{-1}}$)	0.099	[21]
human albumin (100%, extrapolated)	0.15	[20]
blood	0.14	[20]
olive oil	1.79	[21]
Intralipid®(30%)	0.6	[22]
Intralipid®(20%)	0.4	[23]
Intralipid®(10%, interpolated)	0.26	
Intralipid®(5%, interpolated)	0.18	
Intralipid®(2%, interpolated)	0.13	
Intralipid®(1%, interpolated)	0.12	

the form

$$\frac{N_\uparrow}{N_\downarrow} = \frac{\exp\left(\frac{\hbar\gamma B_0}{2k_BT}\right)}{\exp\left(\frac{-\hbar\gamma B_0}{2k_BT}\right)} \approx \frac{1+\frac{\hbar\gamma B_0}{2k_BT}}{1-\frac{\hbar\gamma B_0}{2k_BT}}, \tag{2.2}$$

where the approximation results from a Taylor series expansion of the terms and the assumption that $\hbar\gamma B_0/2k_BT \ll 1$, valid for temperatures relevant to solution state NMR. For ^{129}Xe at room temperature (298.15 K) and in an external magnetic field of 7.05 T (the field at which all experiments for this dissertation were performed), this results in

$$\frac{N_\uparrow}{N_\downarrow} = \frac{1.000\,006\,68}{0.999\,993\,32} = 1.000\,013\,36. \tag{2.3}$$

In other terms, typical NMR experiments involving ^{129}Xe detect signal from only thirteen nuclei out of every million, while the net signal contribution from the other 999 987 nuclei, possessing equal quantities of spins up and spins down, is zero.

The polarization of a sample refers to the ratio of the population difference between the two states to the total population. This is represented mathematically as:

$$P = \frac{N_\uparrow - N_\downarrow}{N_\uparrow + N_\downarrow} = \frac{\hbar\gamma B_0}{2k_BT}. \tag{2.4}$$

For ^{129}Xe under the above-mentioned conditions, $P = 6.6834 \times 10^{-6}$. As the signal depends linearly on the polarization, improving the polarization is of primary importance in NMR.

In principle, there are several ways to increase the NMR signal from spins with low polarization. First, if relatively few spins N contribute to the signal, one could simply use more spins. In a standard 5 mm NMR tube, approximately 250 μL of liquid will contribute to the signal. Assuming standard xenon experimental conditions as described earlier and the use of natural abundance xenon (26.4% ^{129}Xe), approximately 3×10^{10} ^{129}Xe spins contribute to the signal in the detectable volume. While larger volumes or higher concentrations could be used, that is often impractical or prohibitively costly. It is also possible to increase the spin polarization either by increasing the magnetic field strength, B_0, or by lowering the temperature, T. While both of these techniques are used routinely, large, high-field magnets are extraordinarily costly and are not

widely available, and freezing either water or xenon is incompatible with many experimental techniques, especially those involving biological samples.

Despite the above limitations, the xenon NMR signal can be increased dramatically if the spin polarization can be forced into a nonequilibrium state. By transferring polarization from a strongly polarized species to xenon, one can dramatically exceed the polarization afforded by the Boltzmann distribution, enabling much more sensitive NMR detection. This technique, known generally as hyperpolarization, has been a hallmark discovery for magnetic resonance for several decades. There are three major variants of hyperpolarization: (1) dynamic nuclear polarization (DNP) [24–26], in which the spin polarization of electrons is transferred to protons via microwave irradiation, (2) para-hydrogen–induced polarization (PHIP) [27–31], in which specially prepared diatomic hydrogen with high spin polarization is chemically added to a species of interest, and (3) spin-exchange optical pumping (SEOP) [32–34], used in hyperpolarizing noble gases. Only SEOP will be discussed here.

2.3.1 Electron Spin Pumping

Spin-exchange optical pumping relies on two fundamental principles. The first, developed by Kastler in the 1950s [32, 35],[4] is the use of circularly polarized light to pump the spin state of the electrons in vaporized metal to non-Boltzmann levels. Though optical pumping of electron spins is a generally applicable technique, alkali metals are preferred because [36]:

- Their resonance wavelengths are available from inexpensive and relatively powerful laser sources.
- Their high vapor pressure allows for high gas densities and correspondingly high absorption of laser light.
- Their ground states, having a single electron in the valence S orbital, have no orbital angular momentum, mitigating some difficulties with depolarization due to collisions.
- Their single-valence-electron structure makes possible comparisons between theory and experiment.

To hyperpolarize electron spins using SEOP, an alkali metal, in our case rubidium, is placed in a glass cell, where it is subject to laser light. Rubidium, whose melting point is 39.3 °C, is heated in the cell to approximately 160 °C,

[4] Kastler was awarded the 1966 Nobel Prize in physics for this development.

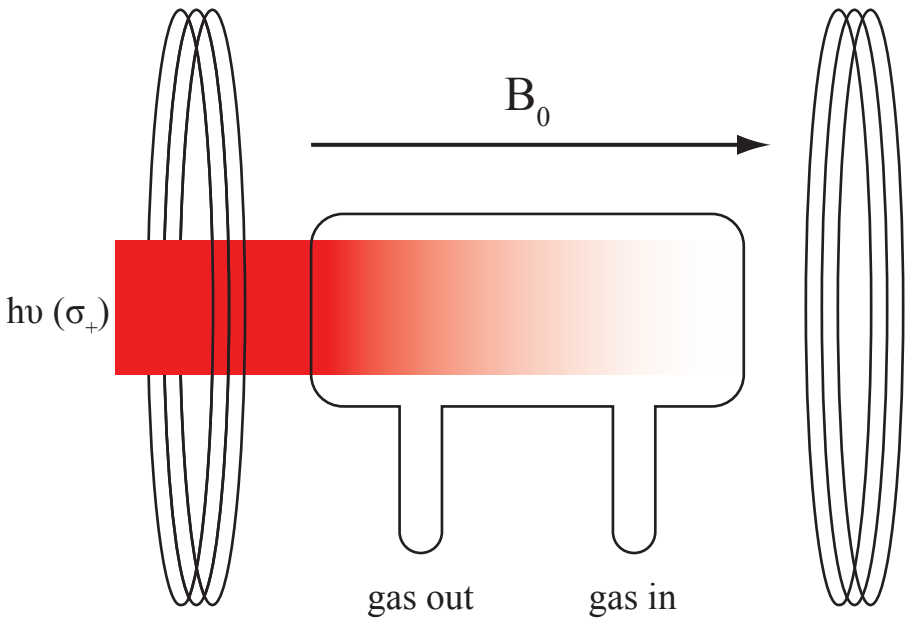

Figure 2.1: A schematic representation of the apparatus used for spin-exchange optical pumping. The glass cell has two arms, one for gas in and one for gas out. Rubidium metal is placed in the cell, which is then heated to ∼160 °C to generate rubidium vapor. The cell is also placed in a magnetic field, ∼25 G, to maintain polarization. Left-circularly polarized laser light, σ_+, irradiates the cell, driving the electronic transitions that ultimately polarize xenon.

at which point its vapor pressure is slightly less than 1 Pa. Besides rubidium, the cell also contains xenon gas (the ultimate target for the polarization), helium, and nitrogen gas. The cell is placed in a magnetic field and irradiated with circularly polarized laser light, generating a non-Boltzmann distribution of electron polarization; see Figure 2.1 for a schematic. Understanding the fundamental mechanisms of polarization requires a brief foray into quantum mechanics; Happer et al. have beautifully explained the details elsewhere [33, 36, 37].

The ground state electron configuration of Rb is [Kr]$5\mathbf{S}^1$, with a single valence electron in an **S** orbital, term symbol $^2S_{1/2}$. In contrast, the lowest electronic excited state has an electron configuration of [Kr]$5\mathbf{P}^1$, with the valence electron in a **P** orbital, $^2P_{1/2}$. The wavelength corresponding to the $^2S_{1/2} \rightarrow {}^2P_{1/2}$ transition in rubidium is 794.978 nm [36];[5] infrared light of this energy is easily produced using a diode laser. Because the laser light is

[5]The transition $^2S_{1/2} \rightarrow {}^2P_{3/2}$ has energy corresponding to light with wavelength 780.241 nm [36] and is not excited in our apparatus.

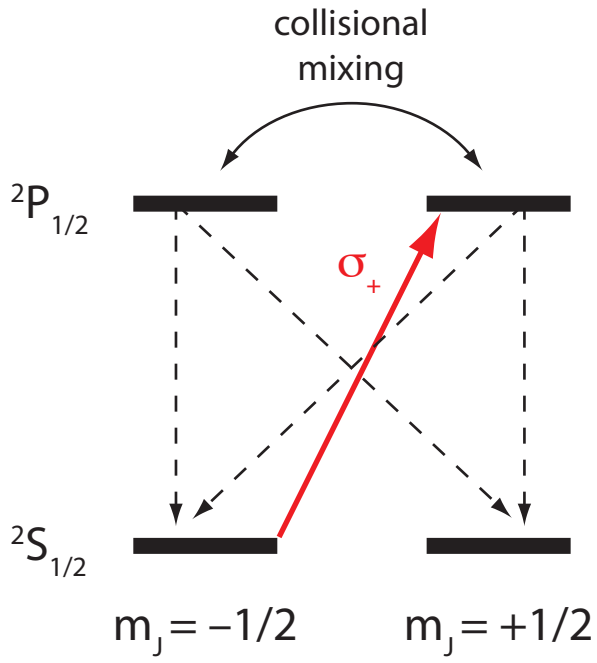

Figure 2.2: The energy level diagram relevant to hyperpolarization of alkali metal electrons. Left-circularly polarized light with wavelength $\lambda = 795\,\text{nm}$ (σ_+, in red), drives the transition from the $m_J = -\frac{1}{2}$ sublevel of the ground state to the $m_J = +\frac{1}{2}$ sublevel of the excited state. Subsequent collisions with buffer gas molecules leads to a mixing of the m_J sublevels, which then relax back to the ground state (dashed lines). After some time, there is a buildup of polarization in the $m_J = +\frac{1}{2}$ sublevel of the ground state, which is subsequently transferred to the nuclear spin of xenon. Adapted from [38].

left-circularly polarized (designated σ_+) with angular momentum $\sigma_+ = +1$, conservation of momentum indicates that only transitions with $\Delta m_J = +1$ are allowed. Consequently, the laser light drives the transition from the $m_J = -\frac{1}{2}$ sublevel of the ground state to the $m_J = +\frac{1}{2}$ sublevel of the excited state. This process is schematically outlined in Figure 2.2.

When the electron is in the $m_J = +\frac{1}{2}$ sublevel of the $^2P_{1/2}$ excited state, it can decay to either m_J sublevel of $^2S_{1/2}$. In the absence of buffer gas, the decay rates to each sublevel are determined by the Clebsch-Gordon coefficients: 0.667 for decay to $m_J = -\frac{1}{2}$ and 0.333 for decay to $m_J = +\frac{1}{2}$ [39]. This would result in radiative decay, with each atom releasing an unpolarized photon upon relaxation, consequently depolarizing other atoms. However, the gas mixture contains two buffer gases in high concentrations which act via collisions with the alkali metal atoms: helium (∼88%), which equalizes the populations of both m_J sublevels in the excited state, and diatomic nitrogen (∼10%), which

provides a mechanism for the excited state to decay by nonradiative processes with 99% probability—the energy is instead deposited into vibrational and rotational states of nitrogen.[6] The result is that there is a net buildup of electron polarization in the $m_J = +\frac{1}{2}$ sublevel of the $^2S_{1/2}$ ground state.

2.3.2 Transfer of Electron Spin Polarization to Noble Gas Nuclei

Much research, originated by others [40, 41] but refined largely by Happer et al. [33, 34, 37, 42–44], demonstrated the transfer of electronic spin polarization to nuclear spin states of noble gases. In brief, Fermi-contact hyperfine interactions facilitate this polarization transfer. These interactions take the form

$$\alpha \mathbf{S} \cdot \mathbf{I} = \frac{\alpha}{2} \left[S_+ I_- + S_- I_+ \right] + \alpha S_Z I_Z, \tag{2.6}$$

where the term in hard brackets is the "flip-flop" term, providing the spin exchange between the alkali metal electron S and the noble gas nucleus I [38, 45]. The coupling constant, α, indicates the probability of finding the alkali metal electron at the nucleus of the noble gas atom. It has the form

$$\alpha = \frac{8\pi}{3} \gamma_S \gamma_I \hbar^2 \delta(r). \tag{2.7}$$

Here, $\delta(r)$ is the Dirac delta function, imparting a strong spatial dependence to the coupling constant.

Because spatial overlap of the alkali metal electron and the noble gas nucleus is crucial to transfer polarization, the mechanism of contact must be understood. In particular, longer-lived alkali-metal–noble-gas complexes will have a higher probability of spin exchange (i.e., a larger spin-exchange cross section) than their shorter-lived counterparts. Two different types of collision are thought to occur between the alkali metal and the noble gas during SEOP: binary collisions with no attractive force between the two atoms and van der Waals complexes, in which the two atoms experience van der Waals attractive forces—the latter occur only with ^{129}Xe and not ^{3}He. Figure 2.3 shows a graphical representation of the two types of interactions. As van der

[6] The probability of radiative decay for rubidium is determined by the branching ratio, ω_γ, as given by [39]:

$$\omega_\gamma \approx \frac{3}{3 + 7.5\,(p_{N_2}/\mathrm{kPa})}. \tag{2.5}$$

For our apparatus, $p_{N_2} \approx 41.4\,\mathrm{kPa}$, resulting in $\omega_\gamma \approx 0.01$. In other words, only 1% of the decay from the electronically excited state occurs via a radiative, depolarizing mechanism.

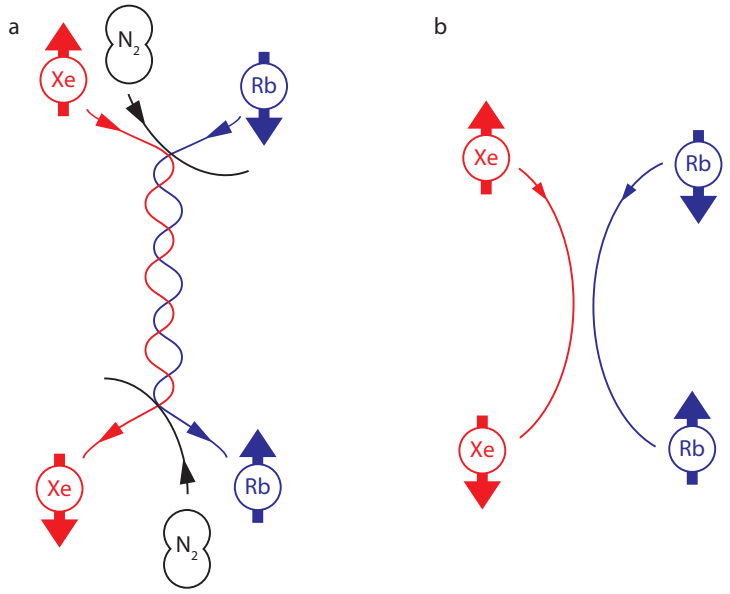

Figure 2.3: Representations of the two types of collisions in spin-exchange optical pumping. a) Formation of a van der Waals complex, which lasts ∼1 ns. These complexes prevail at low pressures (< 10 torr), and are both initiated and destroyed by transfer of momentum resulting from interactions with buffer gas molecules, N_2 in our case. b) A binary collision, with a lifetime of ∼1 ps. These are the most likely types of collisions in our SEOP setup. Unfortunately, they have a lower interaction cross-section and result in lower polarization transfer; however, other experimental conditions demand using higher pressures. Both binary collisions and van der Waals complexes result in polarization transfer from the valence electron of the alkali metal to the nucleus of the noble gas via a Fermi-contact hyperfine interaction. Adapted from [34].

Waals forces are quite weak, these complexes are disrupted by collisions with a third species; hence, these complexes are more prevalent at low pressures, typically tens of torr. According to [34], van der Waals complexes exist for approximately 1 ns, while binary collisions take place over roughly 1 ps. At pressures of approximately 3000 torr, common in our apparatus, it is expected that the majority of collisions exist for 1–100 ps, and thus are binary in nature [46, 47]. The difference in lifetimes between binary collisions and van der Waals complexes is partially responsible for increased polarization at lower pressures; however, other experimental considerations, including the need to increase the solubility of xenon, make the use of high pressure preferable.

It is important to note that the total interaction between the alkali metal and the noble gas is not fully described by Equation 2.6—the Fermi-contact hyperfine interaction can be further separated into an isotropic and an anisotropic

part, yielding a spin-rotation interaction that results in depolarization of the noble gas. These interactions will not be discussed here, but are detailed elsewhere [34, 36].

The benefit of spin-exchange optical pumping is clear—in contrast to Boltzmann polarization of ^{129}Xe, calculated in Equations 2.2–2.4 to be 0.000 12%, samples of hp-^{129}Xe using our apparatus can be polarized to ∼3%, a 25 000-fold enhancement. Other apparatus can generate polarizations exceeding ∼65% [48], an enhancement of more than 500 000 times.

2.3.3 Comparison of Xenon and Proton Signals

With an understanding of hyperpolarization and solubility of xenon, it is worthwhile to compare the xenon and water NMR signals and to explain why xenon is advantageous. At room temperature and in an external magnetic field of $B_0 = 7.05\,\mathrm{T}$, water has a polarization of $P = 2.4162 \times 10^{-5}$ (see Equation 2.4). The detected signal, M, is given as

$$M = \frac{1}{2} N \gamma \hbar P, \tag{2.8}$$

where N is the number of contributing spins. Water, at room temperature and in a field $B_0 = 7.05\,\mathrm{T}$, generates a signal of $M = 2.2605 \times 10^{-5}\,\mathrm{J\,T^{-1}\,L^{-1}}$. Compare this to xenon at 367 μM (from a 2% xenon mixture at 60 psi), which has a thermal polarization of $P = 6.6834 \times 10^{-6}$ and a signal of $M = 5.7632 \times 10^{-12}\,\mathrm{J\,T^{-1}\,L^{-1}}$; the water signal is almost four million times larger than the thermally polarized xenon signal. Even the signal from hyperpolarized xenon is much weaker than that of water—at $P = 2\%$, the hp-Xe signal is still only $M = 1.7246 \times 10^{-8}\,\mathrm{J\,T^{-1}\,L^{-1}}$, or approximately 1300 times weaker than the water signal. In fact, to make the xenon signal equal to the water signal, one would need either a xenon concentration of 481 mM, achievable in water with a partial pressure of 1570 psi, or a polarization of $P = 2620\%$, a physical impossibility. The practical limit is to use pure, isotopically enriched (100%) ^{129}Xe at 60 psi with high polarization ($P = 65\%$). Though unimaginably costly, under these circumstances it is possible to produce a xenon signal comparable to that of water, with $M = 2.8041 \times 10^{-5}\,\mathrm{J\,T^{-1}\,L^{-1}}$, and it is not even clear that such a polarization could be generated in a xenon gas mixture that does not contain any buffer gases.

The obvious question, given the signal limitations of xenon, is why bother? If the xenon signal is at best comparable to and practically much lower than that of water, why use xenon? An comparison of imaging resolution may make this point most emphatically: imagine a three-dimensional proton image with

a resolution of 250 μm on a side, for a voxel volume of 1.56×10^{-11} L. From this volume, the magnetic moment, as determined from the signal above, is $3.5320 \times 10^{-16}\,\mathrm{J\,T^{-1}}$. To get a comparable magnetic moment from hp-Xe with $P = 2\%$ and at a concentration of 367 μM, one would need a voxel volume of 2.0480×10^{-8} L, or an isotropic voxel edge length of approximately 2.7 mm.

Xenon does have many attractive NMR properties, including its relaxation and chemical shift properties, which will be discussed below. Also, its interaction with host molecules (see Chapter 3) makes molecular imaging using xenon possible, if at lower resolution than with protons. However, because the amount of signal *per spin* is much greater in xenon than in water, it is possibly to be spectroscopically more sensitive using xenon than water. Consider the signal from protons in water, $M = 2.2605 \times 10^{-5}\,\mathrm{J\,T^{-1}\,L^{-1}}$. One liter of water contains 6.624×10^{25} spins, for a signal per spin of $3.4125 \times 10^{-31}\,\mathrm{J\,T^{-1}}$. In contrast, at 367 μM, there are 2.2101×10^{20} ^{129}Xe spins per liter of water, yielding a signal per spin for hp-Xe at $P = 2\%$ of $7.8033 \times 10^{-29}\,\mathrm{J\,T^{-1}}$; over 200 times more signal per spin than with water.[7] This means that each encoded xenon spin carries much more information than a comparably encoded proton spin. Furthermore, as will be detailed in Chapter 4, it is much easier to affect the entire population of exchanging xenon spins than it would be with proton spins having the same exchange characteristics.

2.4 Relaxation of Hyperpolarized Spins

Relaxation in NMR refers to processes whereby a system of spins, following some perturbation, returns to its equilibrium state. There are two mechanisms for relaxation in NMR: spin-lattice relaxation, wherein a spin ensemble returns to the population distribution defined by the Boltzmann distribution (see Equation 2.2), and spin-spin relaxation, which causes a decoherence of the net precession of spins due to their interactions with one another. Both types of relaxation are exponential in nature, characterized by relaxation times, T_1 for spin-lattice relaxation and T_2 for spin-spin relaxation. Because the times T_1 and T_2 reflect an exponential process, after one time period (either T_1 or T_2), the return to equilibrium is 63% complete, after two time periods it is 86% complete, and only after five time periods is it more than 99% complete. While much more detailed accounts of relaxation are available [3–8], here we will discuss the consequences of relaxation on hyperpolarized systems.

In proton NMR, thermal polarization is usually sufficient to generate a large signal; consequently, spin-lattice relaxation serves as the *source* of the

[7] Of course, the signal per spin is simply proportional to γP.

detectable signal. To illustrate more explicitly, a proton-based sample is placed in a magnet, where it is left undisturbed for several times T_1. This waiting period, rarely longer than 30 seconds, allows T_1 relaxation to bring the spins to a detectable thermal polarization. At this point, the spin system can be perturbed using a variety of pulse techniques; however, the maximum signal is detected if the whole population of spins is converted into detectable coherences. Following such complete conversion of spin populations into coherences, the polarization is zero. Because protons in thermal equilibrium generate readily detectable signal, the sample is then allowed to sit unperturbed again for several times T_1 until, due to spin-lattice relaxation, it is in a (nearly) Boltzmann distribution of spin populations and the experiment can be repeated.

When using hyperpolarized spins, the effect of spin-lattice relaxation must be considered differently. As discussed in Section 2.3, while the thermal polarization of ^{129}Xe is extremely low—insufficient to be useful in typical experiments—the hyperpolarized signal is easily detectable. Consequently, as spin-lattice relaxation acts to restore a hyperpolarized system of spins to a Boltzmann distribution, signal is lost, not restored. The time that elapses between the generation of hp-^{129}Xe in the optical pumping cell and the detection of the signal in the magnet is limited to avoid excessive spin-lattice relaxation. In other words, the delivery time of xenon to the sample needs to be less than T_1. Additionally, as in proton NMR, the maximum signal is acquired when all populations are converted to coherences and are subsequently lost. Thus, to refresh the xenon signal, new hp-^{129}Xe must be introduced into the sample; this is easily accomplished with a set of capillary tubes that bubble xenon gas into the sample.

While the need to move xenon from the polarizer to the sample within T_1 may appear to impose large experimental obstacles, the T_1 of xenon is quite long: around 50 seconds in the gas phase and up to many hours in the solid phase.[8] In typical experiments discussed here, xenon remains in the gas phase until it is dissolved into the sample, traveling from the polarizer to the sample through a series of teflon tubes. The total travel time is estimated to be 10–20 s, depending on the flow rate. One consideration for transporting a sample of hyperpolarized nuclei is the need for a persistent magnetic field during transport. Thermal polarization is a ratio of the difference between energy levels to the amount of energy available thermally. If there is no external magnetic field, the nuclear spin states become degenerate, T_1 is reduced to zero, and the populations immediately equilibrate. Helmholtz coils surrounding

[8]Solid xenon is easily produced using liquid nitrogen, at which temperature T_1 is approximately 3 hr. At liquid helium temperatures, the T_1 increases to over 100 hr [49, 50].

the optical pumping cell produce a magnetic field that allows xenon to remain polarized following collisions with alkali metal atoms, while the fringe field of the superconducting NMR magnet maintains an energy level splitting during travel to the sample.

Many properties of xenon make it an attractive candidate for *in vivo* studies, including its large chemical shift range, its solubility in blood, its biocompatibility, and its ability to transgress the blood-brain barrier. To date, hp-^{129}Xe has been used in lung imaging of both animals and humans [16, 51, 52]. However, while in gas and condensed phases the T_1 of xenon is quite long, it is dramatically reduced in blood: approximately 10 s in arterial (oxygenated) blood and only 3–5 s in venous blood, the difference owing to the exposed paramagnetic center of hemoglobin in deoxygenated blood [53].[9] With a blood circulation time of 10–15 s in humans [56], it seems unlikely that injections of hp-^{129}Xe will be easily detectable *in vivo*. Several proposals to deliver xenon to patients exist, including trapping xenon in vesicles of lipid or perfluorocarbons; many of these proposals are reviewed in [57]. Though some show promise in animal studies, none of these techniques has yet been demonstrated in humans, and *in vivo* experiments are not included in this work.

2.5 Chemical Shift of Xenon

One of the most valuable aspects of NMR spectroscopy is the ability to resolve the magnetic environment of a particular spin within a molecule by the chemical shift. Because the frequency of precession depends linearly on the field strength as $\omega = -\gamma B$, differences in the local magnetic fields surrounding individual nuclei produce different frequencies. The chemical shift accounts for local changes in the magnetic field due to interactions between the electrons surrounding the spin and the external magnetic field, B_0. This change in the precession frequency is represented by the chemical shift term σ as

$$\omega = -\gamma\,(1-\sigma)\,B_0. \tag{2.9}$$

The polarizability of the electron cloud of an atom or molecule, defined as the response of the electrons to an external field, is largely responsible for the magnitude of the chemical shift range. Protons, with a typical chemical shift

[9] For completeness, the T_2 of xenon in blood is also dependent on oxygenation: at 9.4 T, T_2 decreases from 1.9–5.5 ms to 1.4–2.5 ms upon deoxygenation [54]. However, a similar decrease is not observed at 1.5 T [55], indicating that the xenon T_2 is dominated by chemical exchange between different chemical environments in blood. The same is likely true for xenon exchanging in other host systems.

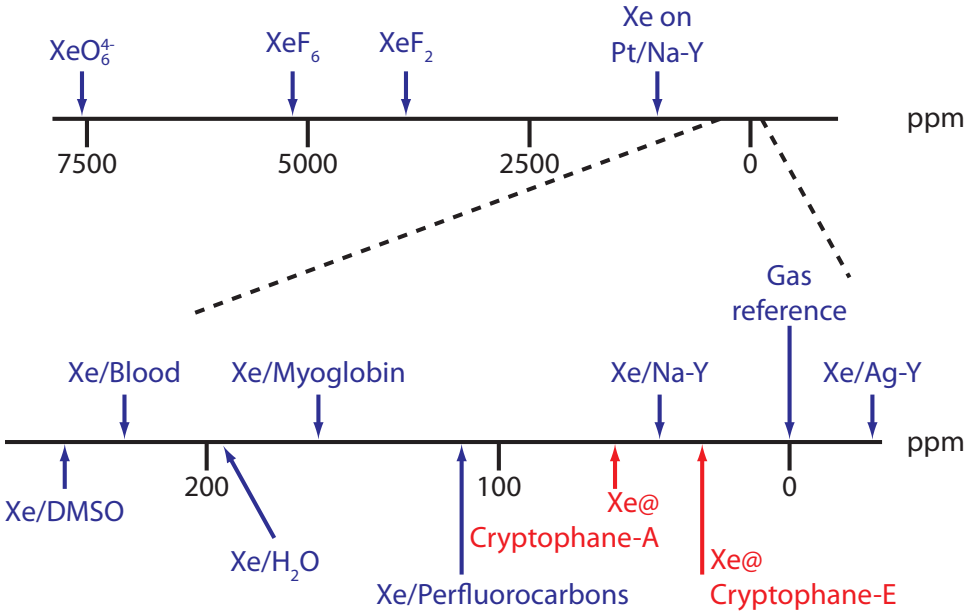

Figure 2.4: Chemical shift values of xenon in different chemical environments. Values in blue adapted from [38, 58].

range of ∼15 ppm, have a polarizability approximately one-sixth that of xenon [19]. Unsurprisingly, xenon exhibits a much larger range of chemical values than protons—up to 250 ppm for atomic xenon and up to several thousand ppm in xenon-halide and xenon-oxide compounds. Some notable chemical shift values of xenon in various chemical states are identified in Table 2.2 and in Figure 2.4.

The data for xenon dissolved in *n*-alkanes, shown in Table 2.2, reveal an interesting trend: the chemical shift of xenon increases linearly with an increase in the percent methylene character of the alkane. For example, of the seven carbons in *n*-heptane, five of them are methylene (–CH_2–) carbons, resulting in 71.4% methylene character. As shown graphically in Figure 2.5, the chemical shift changes by just over 1 ppm per percentage point of methylene character. While it is difficult to make predictions about the magnitude of the xenon chemical shift in other solvents based on this *n*-alkane data, it nicely illustrates the sensitivity of the xenon chemical shift to its local chemical environment. This sensitivity will be examined in greater detail in Section 3.2.

In addition to being sensitive to its chemical environment, the chemical shift of xenon is highly sensitive to the physical state it is in, including temperature and, for xenon gas, density. Jameson et al. [62] described the density dependence

Table 2.2: The chemical shift of xenon in different solvents, as taken from various literature sources. Multiple shift values were given for some solvents; all are listed.

Solvent	Chemical shift (ppm)	Reference	Solvent	Chemical shift (ppm)	Reference
ethane	93.1	[59]	*n*-hexadecane	182.8	[59]
propane	125.7	[59]		186.	[60]
n-butane	145.4	[59]	*n*-heptadecane	183.3	[59]
methanol	148.	[60]	1-octanol	187.	[60]
methyl chloride	153.	[60]	nitrobenzene	189.	[60]
n-pentane	154.1	[59]	toluene	190.	[60]
	156.	[60]	2,2,4-trimethylpentane	192.	[60]
tetramethylsilane	158.	[60]	methylene chloride	192.	[60]
cyclopentane	158.	[60]	saline	192.	[57]
diethyl ether	160.	[60]	oleic acid	193.	[60]
n-hexane	160.3	[59]	intralipid 20%	194.	[57]
cyclohexane	163.7	[61]	intralipid 30%	194.5	[57]
ethanol	165.	[60]	benzene	195.	[60]
ethyl acetate	168.	[60]	water	196.	[60]
n-heptane	166.0	[59]	pyridine	197.	[60]
	168.	[60]	olive oil	198.	[60]
n-octane	169.8	[59]	ethylene glycol	199.	[60]
	171.	[60]	chlorobenzene	200.1	[61]
n-nonane	171.7	[59]	*m*-dichlorobenzene	207.	[60]
acetone	175.	[60]	methyl iodide	209.	[60]
n-decane	175.6	[59]	chloroform	215.0	[61]
	177.	[60]	bromobenzene	219.	[60]
1-butanol	176.	[60]	carbon tetrachloride	221.0	[61]
fluorobenzene	176.	[60]	carbon disulfide	225.	[60]
n-undecane	176.0	[59]	DMSO	245.8	[57]
n-dodecane	176.6	[59]	iodobenzene	246.7	[61]
n-tridecane	179.5	[59]	bromoform	285.	[60]
n-tetradecane	180.7	[59]	methylene iodide	333.0	[61]
n-pentadecane	181.7	[59]			

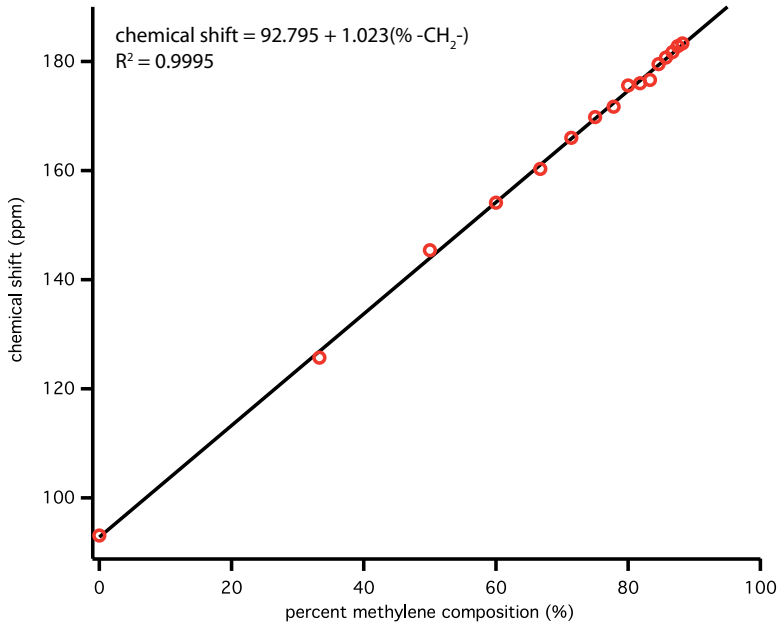

Figure 2.5: Chemical shift values of xenon in a series of n-alkanes. Adapted from [59].

of the chemical shift in terms of virial coefficients:

$$\sigma = \sigma_0 + \sigma_1\rho + \sigma_2\rho^2 + \ldots \tag{2.10}$$

Here, ρ is the density in amagats,[10] σ_0 is the reference shift (typically 0 ppm), $\sigma_1 = -0.553\,\mathrm{ppm}\cdot\mathrm{amg}^{-1}$, and $\sigma_2 \approx -0.17 \times 10^{-3}\,\mathrm{ppm}\cdot\mathrm{amg}^{-2}$; σ_1 shows some temperature dependence [63]. The temperature dependence of the xenon chemical shift in solution will be discussed in Chapter 7.

[10] One amagat (amg) is the density of an ideal gas at 1 atm and 298.15 K, corresponding to a particle density of approximately $2.69 \times 10^{19}\,\mathrm{cm}^{-3}$.

Chapter 3

Xenon in Cryptophane

> "All science is interdisciplinary, from magnetic moments to molecules to men."
> —Paul Lauterbur, quoted by R. R. Ernst, 2003

Several physical properties of xenon make it an interesting candidate for molecular imaging: its solubility in many solvents, its large chemical shift range, its hyperpolarizability, and, for *in vivo* applications, its biocompatibility. As xenon is not naturally present in most samples of interest, it cannot be used for MR imaging the same way protons can—while proton MRI can image the spatial distribution of endogenous spins in water or fat, xenon MR cannot. However, there are sensor molecules that interact strongly with xenon, facilitating measurement using xenon MRI. Furthermore, the sensitivity of xenon to its local chemical environment as measured by NMR can yield functional information about the sensor molecule, further augmenting the utility of xenon NMR.

3.1 Requirements of Xenon Hosts

In a 2009 review on biosensing using xenon NMR, Berthault et al. aptly identified several requirements for a xenon host molecule [64]. Three of those requirements that are particularly relevant to this research are:

1. A high affinity for xenon.
2. An appropriate exchange rate for replacing xenon bound in the sensor molecule with new, freshly polarized xenon.
3. Minimal relaxation for xenon in the host molecule.

The importance of balance between the first two items, a high affinity and an appropriate exchange rate for xenon in the host, cannot be understated. Without a high binding affinity, few host molecules would encapsulate xenon atoms, leading to a weak signal from bound xenon. However, most host-guest systems with high binding affinity only reluctantly dissociate, restricting new guests from entering the host. This is particularly problematic for hyperpolarized systems, since hp-^{129}Xe atoms that remain in the host molecule for times longer than T_1 lose their hyperpolarization and can no longer be detected. The third item, minimal relaxation in the host molecule, is crucial to maintain signal from the hyperpolarized spins throughout the experiment.

Apart from the influence of temperature on the binding interaction, the properties relevant to the above requirements for a host-guest system are intrinsic properties of the host molecules used; the effect of temperature will be explored in greater detail in Chapters 6 and 7. Several molecules and materials have been proposed as xenon hosts, including cyclodextrins, calixarenes, porous materials, hemicarcerands (including cryptophanes), proteins [65], and a hexa-10-carboxydecyl ether of 10,15-dihydro-5H-tribenzo[a,d,g]-cyclononene-2,3,7,8,12,13-hexol, mercifully abbreviated *hexapus* [66]. The research discussed in dissertation concerns the host molecule that has been investigated most thoroughly: cryptophane. The merits of other hosts are concisely reviewed by Berthault [64].[1]

3.2 Cryptophanes

Originally developed in 1981 by André Collet et al. [67], cryptophanes are small, organic, cage-like molecules whose original intent was to temporarily bind uncharged guest molecules, facilitating subsequent reactions. Reports demonstrating binding between cryptophane molecules and methane [68], acetylcholine [69], and bromochlorofluoromethane [70] represent early progress in developing such host-guest systems. The use of cryptophane as a xenon host was first reported in 1998 [71], enabling research on xenon-based molecular sensors that continues today.[2]

[1] In 2008, Naoko Kotera, a visitor to the Pines and Wemmer laboratories, conducted the first known investigation of hexapus as a xenon host molecule. While her final report is unpublished, the results are available from Prof. David Wemmer at DEWemmer@lbl.gov.

[2] Research on xenon-based molecular sensors in the Pines laboratory uses monoacid cryptophane-A (see Table 3.1), purchased from Dr. Kang Zhao in Tianjin, China. The ambitious reader is referred to [72] for details pertaining to the synthesis of cryptophanes.

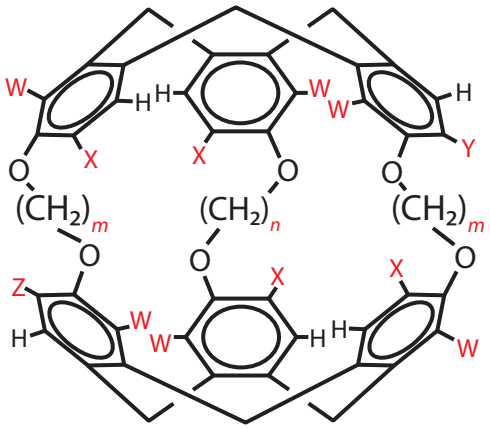

Figure 3.1: A schematic representation of a generic cryptophane molecule. Various cryptophanes exist, distinguishable by the sites labeled in red. Table 3.1 identifies several types of cryptophane based on the notation used in this figure.

Cryptophane molecules consist of two primary components: two cyclotriveratrylene "caps", each containing three aromatic rings connected by methylene bridges, and a series of linkers holding these two caps together. A generic cryptophane molecule is illustraed in Figure 3.1; differences between substituents on both the caps and linkers (marked in red) give rise to different types of cryptophane. For example, cryptophane-A consists of two cyclotriveratrylene caps, each bearing three methoxy groups, connected by three ethyl linkers. When propyl linkers are used instead of ethyl linkers, the resulting molecule is cryptophane-E. A summary of several types of cryptophanes is given in Table 3.1; the abbreviations shown there will be used throughout this dissertation.

Given the large range of chemical shift values of xenon in different solvents (see Section 2.5), it is unsurprising that xenon is exquisitely sensitive to the particular type of cryptophane in which it is bound. For example, Brotin et al. reported that the chemical shift of xenon decreases as the internal cavity size of the host cryptophane molecule increases [74]. In fact, a chemical shift range of almost 40 ppm can be accessed by changing only the volume of the cryptophane; Table 3.2 lists several such chemical shift values. Changing the substituents on the cryptophane molecule, for example, changing X and Y in Figure 3.1 from —OCH_3 to —H, can change the xenon chemical shift by up to 16 ppm [78]. Additionally, when cryptophane is attached to a chemical binding unit, a chemical shift range of over 2 ppm is accessible by titrating protein into the solution [77]. Furthermore, even the chirality of the cryptophane itself, a consequence of the *anti* configuration of the linkers, can produce peaks that are distinguishable in an NMR spectrum, provided that there is another chiral

Table 3.1: Several types of cryptophane are produced by altering the chemical substituents at various positions within the molecule. Ordered roughly by increasing size, these substituents listed in this table correspond to the schematic shown in Figure 3.1.

Name	Abbreviation	Molecular Formula	Molecular Mass (g/mol)	m	n	W	X	Y	Z
cryptophane-1,1,1	Cry111	$C_{51}H_{48}O_{12}$	852.92	1	1	H	H	H	H
cryptophane-A	CryA	$C_{54}H_{54}O_{12}$	895.00	2	2	H	OCH_3	OCH_3	OCH_3
monoacid cryptophane-A	CryA	$C_{55}H_{54}O_{14}$	939.01	2	2	H	OCH_3	OCH_3	OCH_2COOH
diacid cryptophane-A	CryA	$C_{56}H_{54}O_{16}$	983.02	2	2	H	OCH_3	OCH_2COOH	OCH_2COOH
cryptophane-223	Cry223	$C_{55}H_{56}O_{12}$	909.02	2	3	H	OCH_3	OCH_3	OCH_3
cryptophane-233	Cry233	$C_{56}H_{58}O_{12}$	923.06	3	2	H	OCH_3	OCH_3	OCH_3
cryptophane-224	Cry224	$C_{56}H_{58}O_{12}$	923.06	2	4	H	OCH_3	OCH_3	OCH_3
cryptophane-E	CryE	$C_{57}H_{60}O_{12}$	937.08	3	3	H	OCH_3	OCH_3	OCH_3
cryptophane-4,4,4	Cry444	$C_{60}H_{66}O_{12}$	979.16	4	4	H	OCH_3	OCH_3	OCH_3
dodecamethoxy cryptophane-A	ddCryA	$C_{60}H_{66}O_{18}$	1075.16	2	2	OCH_3	OCH_3	OCH_3	OCH_3
dodecamethoxy cryptophane-E	ddCryE	$C_{63}H_{72}O_{18}$	1117.24	3	3	OCH_3	OCH_3	OCH_3	OCH_3
dodecamethoxy cryptophane-4,4,4	ddCry444	$C_{66}H_{78}O_{18}$	1159.32	4	4	OCH_3	OCH_3	OCH_3	OCH_3
cryptophane-O	CryO	$C_{63}H_{72}O_{12}$	1021.24	5	5	H	OCH_3	OCH_3	OCH_3

Table 3.2: The chemical shift of xenon in various cryptophanes depends on both the solvent and on the internal cavity size of the cryptophane. Berthault et al. have shown that external substituents on the cryptophane (W, X, Y, Z) have a negligible effect on the internal cavity size [64]; the major determinant in cavity size is the number of methylene groups m and n in the linkers.

	chemical shift ppm	cavity size (Å^3)
Xe@Cry111$_{C_2D_2Cl_2}$	31.1 [73]	81 [73]
Xe@CryA$_{C_2D_2Cl_2}$	68 [74]	95.0 [74]
Xe@CryA$_{aq}$	64 [75]	
Xe@CryA$_{lipid}$	73 [76]	
Xe@Cry223$_{C_2D_2Cl_2}$	60 [74]	102.1 [74]
Xe@Cry223$_{aq}$	52 [75]	
Xe@Cry233$_{C_2D_2Cl_2}$	47 [74]	117.2 [74]
Xe@Cry233$_{aq}$	42 [75]	
Xe@Cry224		109.9 [74]
Xe@CryE$_{C_2D_2Cl_2}$	30 [77]	120.9 [74]
Xe@CryE$_{aq}$	35 [75]	

center present in the molecule [79]. This phenomenal range of frequencies accessible by using variants of cryptophane illustrates the exquisite sensitivity of xenon to its local chemical environment.

More surprising still, xenon not only reports its own local chemical environment (the host molecule), but on the local chemical environment of its host molecule. In 2010, the chemical shift of xenon in diacid CryA was measured both in aqueous and in 1–10% lipid suspensions [76]. Remarkably, the introduction of lipid to the solution changes the chemical shift of xenon in CryA up to 10 ppm. The interactions of xenon with lipids are discussed in Chapter 5. Truly, the variety of methods for affecting the frequency of xenon in NMR experiments is remarkable.

Besides its significant effect on the chemical shift, the length of the linkers used to hold the caps of cryptophane together greatly influences the strength of the binding interaction between the cryptophane and xenon. In 1998, Mecozzi and Rebek showed that the strongest binding between host and guest moleucles occurs when the guest occupies 55% of the volume of the host [80]. Xenon atoms, approximately 4.3 Å in diameter, have a volume of 42 Å^3, indicating that the optimum host will have a cavity volume of approximately 76 Å^3. The smallest cryptophane yet synthesized, Cry111, has an internal cavity volume

of 81 Å^3, just a few percent larger than the optimum. Unsurprisingly, Cry111 shows a high binding affinity for xenon in organic solvent, approximately 10 000 M^{-1} [73]; about 2–3 times greater than CryA, the next larger xenon host. In water, a similar dependence of the binding affinity on the size of the xenon host is apparent [75].

The consequences of binding affinity on NMR detection of caged xenon merit a brief look at the thermodynamics of binding. In aqueous samples at room temperature and with a gas pressure of 60 psi, a 2% xenon gas mixture provides only 367 μM Xe—roughly one million times fewer nuclei than there are protons in water (110 M). Relying on a previously published value of $K = 6800\,\mathrm{M}^{-1}$ as the binding constant for xenon with cryptophane-A cage [75], the reaction

$$\mathrm{Xe} + \mathrm{cage} \rightarrow \mathrm{Xe@cage}$$

indicates that only 70% of cryptophane molecules bind xenon atoms.[3] Of those bound xenon atoms, arising from a natural-abundance distribution of xenon, only 26% are ^{129}Xe, the NMR-active isotope. Thus, for a reasonably high cryptophane concentration of 30 μM, the signal from xenon bound in the cage comes from only 5.5 μM ^{129}Xe. Despite the low concentration, the Xe@cage signal is detectable in several acquisitions, shown in Figure 3.2.

In xenon-based NMR studies, it is not the binding affinity alone that affects the spectroscopic result, but also the average time a xenon atom spends in a cryptophane cage before exchanging back into the bulk solution. When considering this average residence time, it is reasonable to assume that the average residence time is inversely proportional to the binding affinity; in other words, xenon that is more tightly bound in a cryptophane cage is likely to stay there longer. Literature values for the residence time of xenon in cage range from 30–300 ms in CryA in aqueous solution [75, 81], to 11 ms for CryE in water [75]. It is expected that the residence times in organic solvent will be dramatically different than in aqueous solution, considering the hydrophobic nature of xenon. An unpublished report by Ramirez et al.[4] documents the use of a model that fits several NMR parameters to a series of data sets, ultimately producing information including the residence time. These models, in excellent agreement with experimental data, indicate a residence time of 20–40 ms for xenon in CryA in water at room temperature, and 5–7 ms at 37°C. While these values are somewhat dependent on the concentration of both xenon and cryptophane in solution, their close agreement with many data sets lends to their use in this dissertation.

[3] Calculations showing this conclusion are shown in Appendix A on page 109.

[4] Available from Matt Ramirez at mramirez@berkeley.edu.

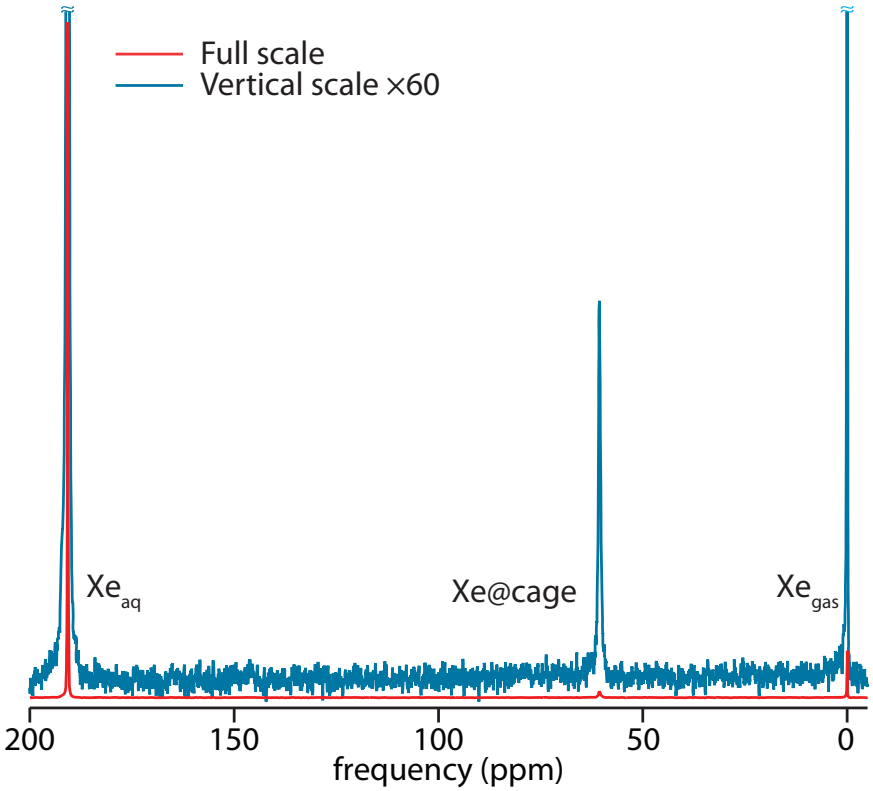

Figure 3.2: A ^{129}Xe NMR spectrum of xenon and cryptophane-A in water. The cryptophane is solubilized by attachment to a 12-amino acid peptide and is present at 30 μM. Three peaks are apparent in the spectrum: Xe_{aq} at 190.7 ppm. Xe@cage at 60.6 ppm, and Xe_{gas}, which is used as a reference to 0 ppm. The Xe_{aq} peak is approximately 100 times more intense than the Xe@cage peak. This spectrum is signal averaged over 64 acquisitions.

Chapter 4

Detecting Xenon with NMR: Hyper-CEST

> "I have not yet lost a feeling of wonder, and of delight, that this delicate motion should reside in all the things around us, revealing itself only to him who looks for it. I remember, in the winter of our first experiments, just seven years ago, looking on snow with new eyes. There the snow lay around my doorstep—great heaps of protons quietly precessing in the earth's magnetic field. To see the world for a moment as something rich and strange is the private reward of many a discovery."
> —Edward M. Purcell, 1952

As has been mentioned previously, sensitivity is the perpetual plague of NMR and, despite advances in hyperpolarization, of xenon NMR in particular. One highly successful approach to overcoming sensitivity limitations is to rely on the in-and-out exchange of xenon with its host cage. Xenon resides in the cage only temporarily, typically tens of milliseconds. Consequently, an encoding pulse that lasts several seconds will encode many xenon spins, resulting in a correspondingly large increase in signal sensitivity. Such an encoding method was originally termed Magnetization Transfer Contrast [82]. (Later the same technique became referred to as Chemical Exchange Saturation Transfer or CEST.) While originally developed for, and still widely used in, proton NMR, the incarnation of this technique for hp-^{129}Xe is termed Hyper-CEST, developed in the Pines lab in 2006 [1].[1] Since its development, Hyper-CEST has facilitated

[1] A similar technique was developed by Ruppert et al. in 2000 [83]. However, that study was limited by xenon diffusion in the gas phase; the 2006 report is more general and is used as an example here.

detection of less than 100 pM cage and even more sensitive detection of certain macromolecular constructs optimized for sensitivity.

4.1 Hyper-CEST

The successful CEST experiment requires two distinguishable signals arising from populations that are in chemical exchange. While the exchange rate of the populations and the distinguishability of their NMR signals may at first seem orthogonal, in fact there is a strong correlation that can limit information available from NMR analysis of exchanging systems. Let us define k as the rate of exchange between two populations, and $\Delta\omega$ as the difference in precession frequency between those populations. On average, the length of time that one can observe a spin precessing at one frequency is $1/k$; after that time, the spin will exchange and begin precessing at the other frequency. If the exchange time is slower than $1/\Delta\omega$, the two signals are resolvable; if it is much faster than $1/\Delta\omega$, a single resonance is observed at the population-weighted mean between the two signals. For CEST experiments, having a rapid exchange rate is desirable, since it facilitates the encoding of a large number of spins in a short time. However, this is only feasible if the difference in chemical shifts, $\Delta\omega$, is sufficiently large; otherwise, the resonances are indistinguishable. These parameters define the NMR timescale for chemical exchange—slow exchange results in distinguishable signals, while fast exchange does not. Fortunately, Xe_{aq} and Xe@cage are separated by a remarkably large frequency difference of approximately 130 ppm, for which, at a field strength of 7.05 T, $\Delta\omega/2\pi = 1700$ Hz. This separation facilitates Hyper-CEST experiments with systems in rapid exchange; in most experiments, xenon resides in cryptophane for no less than 5 ms ($k = 200$ Hz), but residence times as low as 1 ms ($k = 1000$ Hz) are easily accessible.

Having established that the system of interest has appropriate exchange rates, employing the Hyper-CEST sequence is straightforward. Following delivery of hp-^{129}Xe to the sample, one applies a saturation pulse at the Xe@cage frequency, followed by excitation and readout of the Xe_{aq} signal; the pulse sequence is shown in Figure 4.1. Xenon spins that experienced the saturation pulse prior to acquisition do not contribute to the final signal—their contribution is saturated. Because saturated Xe@cage spins are in chemical exchange with the bulk Xe_{aq} pool, the net Xe_{aq} signal will decrease as the saturation pulse is applied.

One acquisition is insufficient to characterize a Hyper-CEST experiment; since the Xe_{aq} signal is depleted following saturation at the Xe@cage frequency,

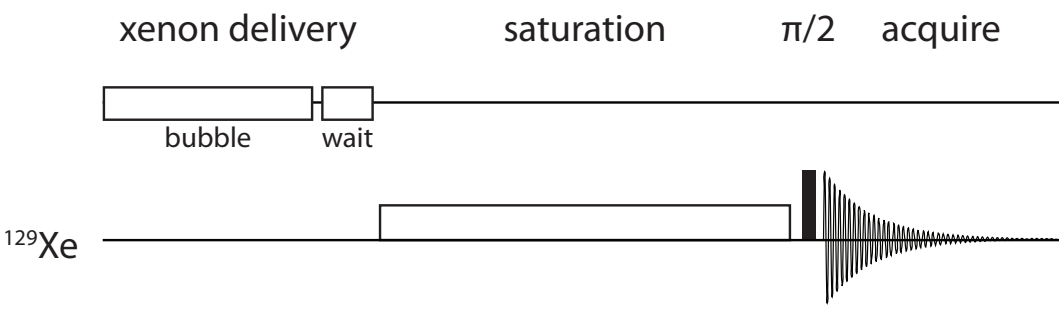

Figure 4.1: A schematic showing the Hyper-CEST pulse sequence. Following the delivery of hp-^{129}Xe to the sample (indicated here with a bubble period followed by a wait period), a saturation pulse is applied at the frequency corresponding to Xe@cage. Following saturation, a hard $\pi/2$ excitation pulse is applied and the resultant signal is detected. Hyper-CEST is a highly modular approach and can be used with many other detection schemes, including both imaging and remote detection methods.

it is impossible to distinguish a single saturation experiment from one that simply has low signal. Consequently, a control experiment is conducted wherein the saturation pulse is applied at a frequency off-resonant with the Xe@cage spins. Typically, the frequency chosen is one with the same frequency shift between the Xe_{aq} and Xe@cage signals, but on the opposite side of the Xe_{aq} signal, shown schematically in Figure 4.2. This accounts for any potential "spillover" or direct saturation of the Xe_{aq} peak. Following the acquisition of both the control and the on-resonant spectra, the difference in signal intensity between the Xe_{aq} signals in the two experiments reveals a signal corresponding to the presence of xenon at the Xe@cage frequency. This subtraction method is illustrated in Figure 4.3.

The biggest advantage of Hyper-CEST over direct detection is the accrual of encoded xenon spins over time. Hypothetically, if there was one cryptophane cage in the detection volume of the NMR probe, only one xenon spin would be excited and detected at the Xe@cage frequency. However, if the average residence time of xenon in the cage is 20 ms and the Hyper-CEST saturation pulse is applied for five seconds (an experimentally accessible duration), approximately 250 spins will pass through the cage and become encoded by the saturation pulse, increasing the signal response correspondingly. The factor of two-hundred fifty is not entirely accurate: some spins will enter the cage more than once, reducing the number of unique spins that are encoded, and requiring two acquisitions introduces excess noise into the spectra. (The issue of noise is analogous to the advantage in signal-to-noise ratio (SNR) for Fourier transform NMR (FT-NMR) over frequency-swept cw-NMR.) Still, the mini-

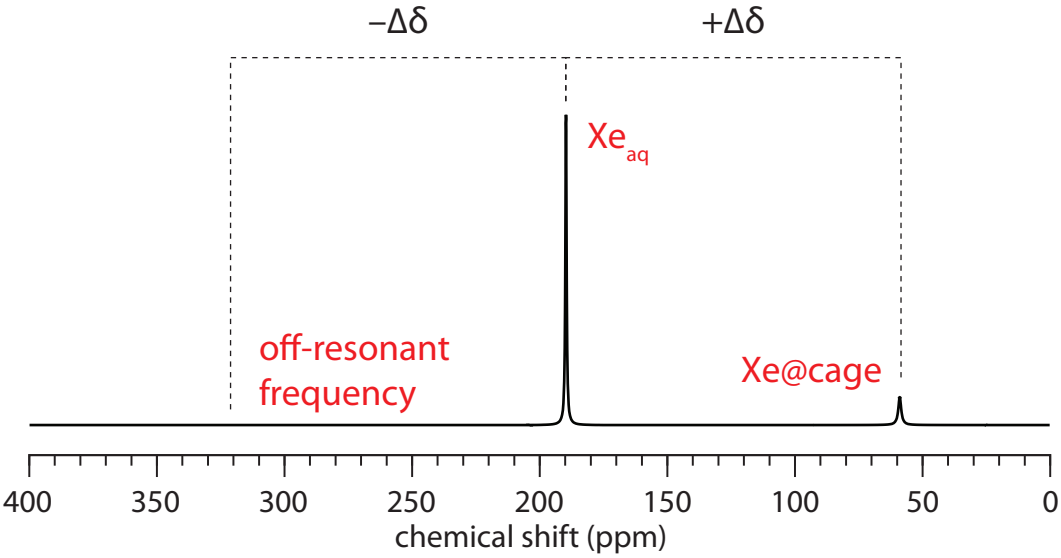

Figure 4.2: Hyper-CEST experiments require two acquisitions to verify the source of contrast is encapsulated xenon: an on-resonant saturation pulse at the Xe@cage frequency ($+\Delta\delta$), and an off-resonant pulse applied at a frequency separation equal to the separation between the Xe_{aq} and Xe@cage peaks, but in the opposite direction ($-\Delta\delta$). Any direct saturation of the Xe_{aq} will be accounted for in both the off-resonant and on-resonant acquisitions and will not contribute to the total contrast.

mum concentration of cage needed for detection is dramatically reduced by utilizing the time-integration of encoding afforded by Hyper-CEST. There are two primary limits on the duration of the saturation pulse and, consequently, on the enhancement of detection using Hyper-CEST. T_1 relaxation times place a fundamental limit on the length of saturation—if the hyperpolarized signal decays, there is nothing to detect. Fortunately, as has been discussed earlier, the T_1 of xenon in solution is quite long; we have successfully used saturation pulses of up to 20 s, though longer pulses could be used. The other limit is technical in nature: the power deposited into the probe must not exceed the limits of the probe's integrity.[2]

The Hyper-CEST detection method is highly modular, meaning it can be incorporated into many other pulse sequences for detection. For example, experiments using remote detection [84, 85] with Hyper-CEST are currently being investigated in the Pines lab. Different forms of refreshing hp-^{129}Xe are compatible with Hyper-CEST, including continuous flow of xenon-saturated

[2]From experience, the author notes that significant noise spikes and DC offsets begin to appear in the spectra when the probe's integrity is compromised. Fortunately, only data, not the apparatus itself, was irrecoverably damaged during such acquisitions.

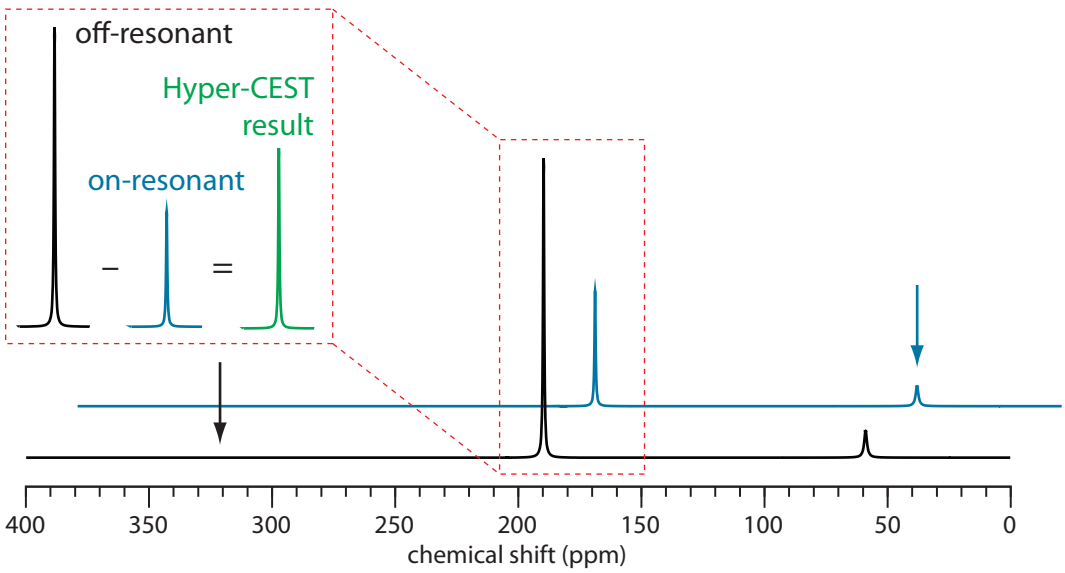

Figure 4.3: A schematic showing the subtraction method used to generate Hyper-CEST contrast. Following on-resonant (blue) and off-resonant (black) saturation, the former signal is subtracted from the latter to generate the positive-contrast spectrum (green). If on-resonant saturation results in complete annihilation of the Xe_{aq} signal, the subtraction results in 100% contrast between the on- and off-resonant experiments.

water. In addition, Hyper-CEST can be incorporated into imaging sequences, as demonstrated in Figure 4.4. The compatibility of Hyper-CEST with many other NMR techniques makes it broadly applicable to varied investigations using xenon.

It is worth mentioning that, unlike in FT-NMR, improving signal detection using Hyper-CEST depends on increasing the contrast-to-noise ratio (CNR) rather than the SNR. If one were interested simply in increasing the SNR, one could use a higher partial pressure of xenon in the sample to increase the number of xenon atoms present. While this would shift the thermodynamic equilibrium toward having more xenon atoms encapsulated in cages, resulting in more encoded spins over the duration of the saturation pulse, there would also be a larger pool of Xe_{aq} spins to saturate. Since a given encoding pulse can only saturate a fixed number of spins in a given time and at a given cage concentration, a larger pool of xenon results in a larger percentage of unencoded spins at the end of the experiment, reducing the contrast of the acquisition. In order to increase the CNR, one must increase the signal (the saturation generated using Hyper-CEST) without a concomitant increase in the number of spins. This can be achieved by either increasing the cage concentration, often at odds with the goal of detecting signals at low concentrations, or by increasing

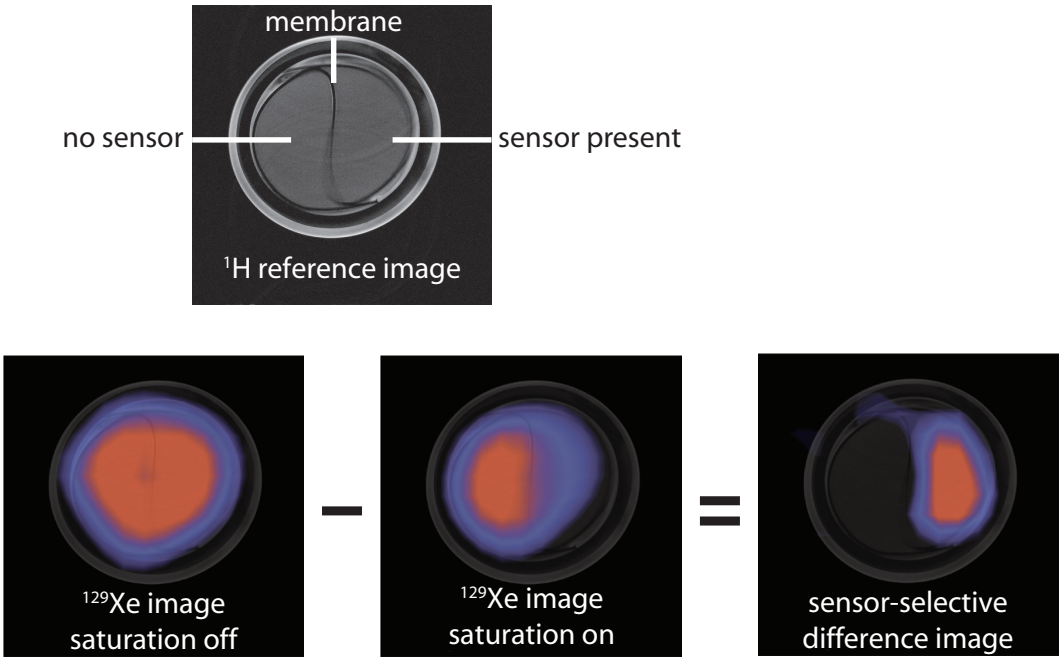

Figure 4.4: A demonstration of Hyper-CEST applied to imaging. A two compartment phantom, top, consists of a left chamber that contains no cryptophane cage, while the right chamber contains cage at approximately 5 μM. When saturation is applied off resonance (bottom left), neither component shows any saturation. When saturation is applied on resonance with the Xe@cage frequency (bottom center), the compartment containing cage is saturated, while the compartment lacking cage shows no change. Subtraction of the two images (bottom right) results in the positive control image showing the location of the cage. A chemical shift imaging (CSI) sequence was used for these images, and the subtraction was performed on the spectra (8×8 matrix), not the images themselves. Adapted from [1].

the polarization per spin. The saturation of highly polarized spins will have a greater effect on the depletion of the Xe_{aq} signal than will the saturation of less polarized spins. Mathematically, the CNR can be expressed in terms of the Xe_{aq} signal, S, from the off-resonant and on-resonant experiments as:

$$CNR = \frac{S_{\text{off-res}} - S_{\text{on-res}}}{S_{\text{off-res}}}. \tag{4.1}$$

Hyper-CEST detection is compatible with generating indirectly detected spectra: while varying the frequency of the saturation pulse, ω_{sat}, the signal from the Xe_{aq} peak is proportional to the concentration of encapsulated xenon at the frequency ω_{sat}. One routinely used application of this approach is to detect the presence of cryptophane cage at concentrations below the threshold for direct detection. The resultant, indirectly acquired spectrum is often

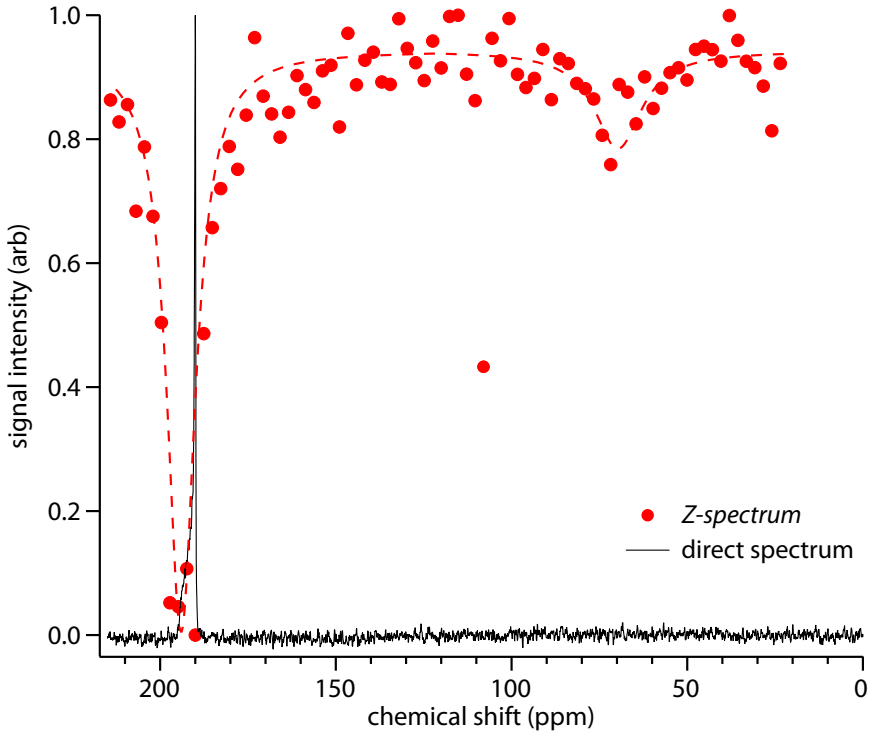

Figure 4.5: Directly acquired spectrum (black) and indirectly acquired *Z-spectrum* (red) of a 50 nM sample of CryA in water. The indirect spectrum was collected in a point-by-point manner, and the intensity after saturation is plotted. The presence of a xenon signal at a particular frequency is manifest by a negative peak, indicating saturation. The peak at 60 ppm, corresponding to Xe@cage, is detectable using indirect (Hyper-CEST) acquisition with 15 s saturation (approximately 20 s acquisition time per point); after 16 acquisitions it is still indistinguishable from the noise in the direct spectrum. Both spectra are normalized to their respective maximum signal points, and the dashed red line is provided only to guide the eye.

referred to as a *Z-spectrum*, a term coined by Grad and Bryant in 1989 [86]; an example *Z-spectrum* is shown in Figure 4.5.

4.2 Selective Saturation Transfer Pulses[3]

To date, Hyper-CEST has been conducted with strong continuous wave (cw) rf fields for frequency-selective saturation. There are several limitations with this approach. First, such experiments must be designed such that the saturation field perturbs only the desired resonance and not others, a task

[3]This section is based on [87].

that is complicated by the strong dependence of saturation transfer on the applied saturation power. Hyper-CEST saturation transfer is optimized for cw pulse powers that result in partial saturation of the $Xe_{solvent}$ resonance, necessitating a second reference experiment and the use of kinetic modeling for quantification of the analyte. Further, multiplexing with xenon-based molecular sensors, a technique to resolve multiple variants of the sensor simultaneously [77], relies on small frequency separations between xenon bound in slightly different host molecules, precluding the use of broad saturation pulses. A related problem involves the spatial multiplexing of arrays of xenon chemical assays on, for example, a microfluidic device; in that case, the optimum imaging approach might involve spectral-spatial selective saturation [88] or multispectral saturation pulses with Hadamard encoding [89]. Finally, the time-averaged sensitivity of these experiments obviously depends on highly efficient saturation, but is constrained *in vivo* by limits on the specific absorption rate (SAR) of the applied pulses [90]. These constraints cannot be simultaneously satisfied in cw-based saturation experiments.

To address these concerns, we have applied band-selective saturation pulse trains in lieu of cw pulses ordinarily used in Hyper-CEST experiments. These pulses have much greater frequency selectivity than cw pulses, obviating the need for separate control experiments. They deliver comparable saturation efficiency at much lower powers, but, depending on the choice of pulse, allow for narrow-bandwidth saturation at high pulse powers. Finally, they are compatible with slice selection and therefore with imaging sequences that depend on spatial-spectral preparation or multispectral excitation or saturation. We demonstrate the application of these saturation pulses to both spectroscopy and imaging experiments employing xenon-based molecular sensors.

Bloch simulations of frequency-selective saturation

As a preliminary to our experimental investigation of saturation transfer phenomena in solutions of xenon molecular exchange agents, we conducted Bloch equation simulations of cw and multiple pulse saturation. These simulations involved numerical solution of the Bloch equations for an exchanging spin system subject to rf irradiation of two different pulse profiles: cw and d-SNOB [91]; The amplitude profile for a d-SNOB pulse is shown in Figure 4.6, while the MATLAB code and explanations detailing the simulations are presented in Appendix B. The simulation took relaxation and other parameters as defined by the experimental measurements and explored parameters including multiple pulse bandwidth, B_1 amplitude, saturation time, and residence time of xenon in the cryptophane-xenon complex. Because the xenon binding kinetics are

not known accurately from our measurements or others (5–50 ms, depending on temperature, concentration, and solvent), these simulations are merely a guide to the parameter space, and not a rigorous route to optimize saturation parameters.

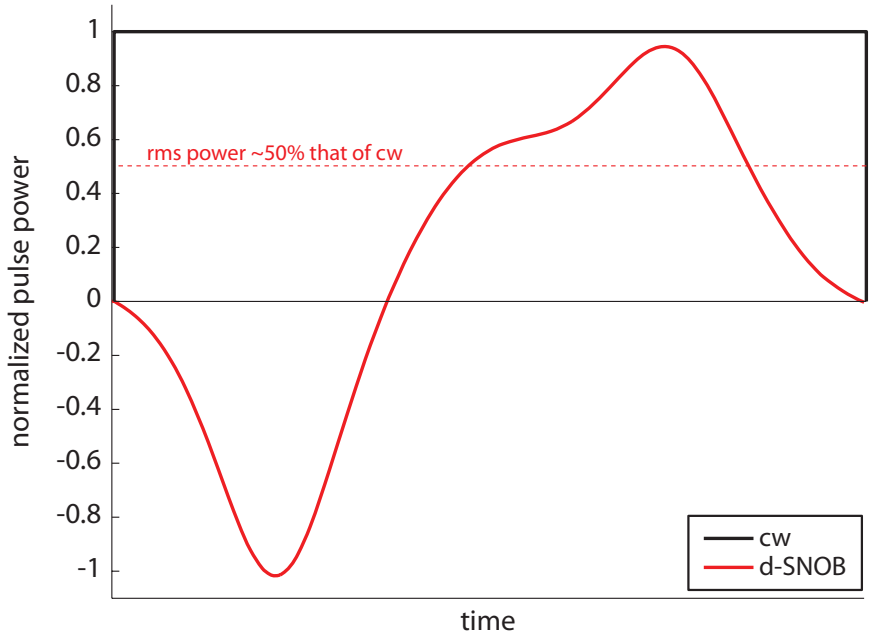

Figure 4.6: The amplitude profiles for both cw (black) and d-SNOB [91] (red) pulses. The rms power of a d-SNOB pulse is 50.26% of the power of a cw pulse with the same peak power, B_1.

In Figure 4.7a, we present a contour plot which relates the observed saturation to B_1 field and residence time (inverse of the exchange rate) for cw saturaion; for saturation using other pulse shapes, the plots are visually similar. For saturation using cw pulses, the power at which optimum saturation is obtained (red circles) decreases roughly exponentially with increasing residence time, as shown in Figure 4.7b. The functional dependence for multiple pulse sequences based on d-SNOB elements is more complicated, by contrast, and is characterized by an initial region in which the power dependence is approximately flat, also in Figure 4.7b. Figure 4.8 illustrates this idea further, showing that in the optimal case, multiple pulse d-SNOB saturation performs better than cw decoupling for a range of relevant residence times. However, the powers at which these optimal saturations are achieved can be up to an order of magnitude higher for cw decoupling.

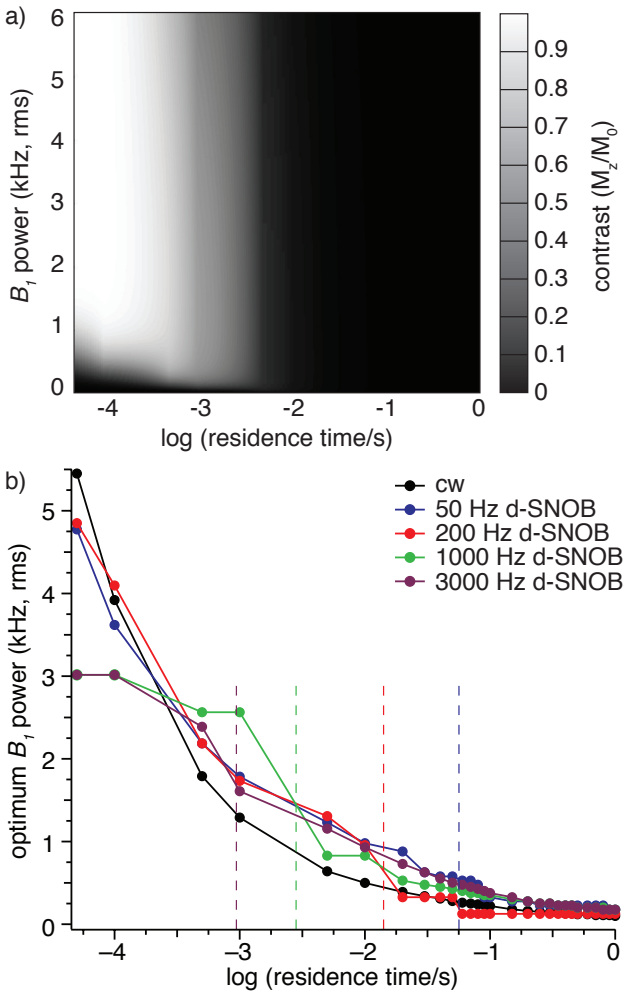

Figure 4.7: Bloch equation simulations indicating contrast generated by various saturation parameters. a) A contour plot illustrating the contrast generated by a cw pulse with various saturation powers, B_1, and on exchanging systems with difference residence times. Black indicates no contrast, while white indicates perfect contrast between the off- and on-resonance experiments. Contour plots for d-SNOB saturation pulses are visually comparable to this. b) The best contrast is not necessarily generated by saturation pulses with the highest power, but rather the saturation pulse power for optimum contrast depends strongly on the residence time of the guest in the host. Five different saturation pulses were simulated (cw, and four d-SNOB pulses corresponding to 50, 200, 1000, and 3000 Hz bandwidth) for a range of residence times from 50 μs to 1 s. For each pulse, the power for optimum contrast decreases with increasing residence time. While the cw pulse shows primarily exponential behavior, the d-SNOB pulses have irregular behavior, including discontinuities in the power-residence time curve. The vertical dashed lines indicate the length of time each unique d-SNOB pulse lasts: 56.4, 14.1, 2.82, and 0.94 ms for the 50, 200, 1000, and 3000 Hz bandwidth d-SNOB pulses, respectively.

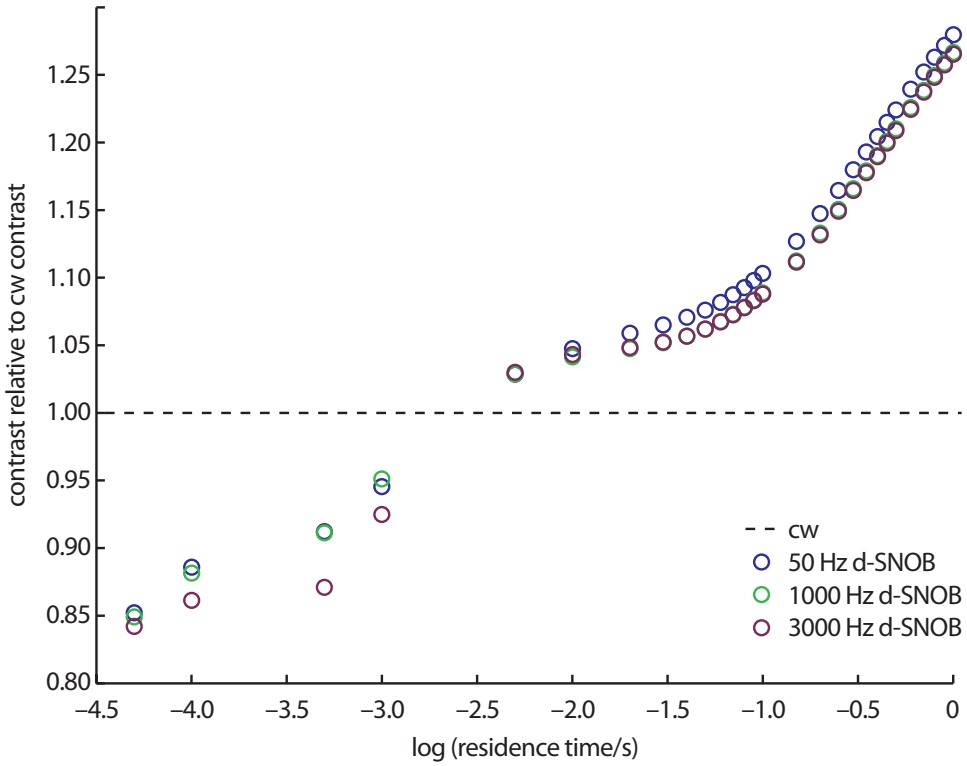

Figure 4.8: A comparision of the simulated contrast generated by power-optimized d-SNOB pulses relative to a cw pulse acting under the same conditions. The best contrast for each pulse at each exchange time was selected and normalized to the cw contrast at that point. At exchange times of approximately 2.5 ms, all d-SNOB saturation pulses can generate more contrast than cw pulses, with the improvement increasing with longer residence times.

Saturation of water

Not only did we assess the experimental behavior of the cw and d-SNOB pulses, as simulated previously, but also of a Gaussian inversion pulse [92], and a SEDUCE pulse [93]. To determine the effective saturation bandwidth for cw pulses of different powers, we applied them to an aqueous solution of 1 mM Gd-DTPA, a concentration of paramagnetic dopant which yielded a ^{1}H T_1 of approximately 1 s for experimental convenience. Each saturation pulse was applied at frequencies ranging from +5 kHz to −5 kHz of the ^{1}H resonance frequency. The strength of the applied field B_1 was varied between 15 and 950 Hz. A contour plot of these saturation data is provided in Figure 4.9. For the highest pulse powers, saturation of 10% or more of the water signal extends ±3 kHz from the ^{1}H resonance frequency, corresponding to a 20 ppm range at an external magnetic field strength $B_0 = 7.05$ T. The contrast in xenon sensor experiments may be one order of magnitude lower (∼1%) for the lowest detectable concentrations.

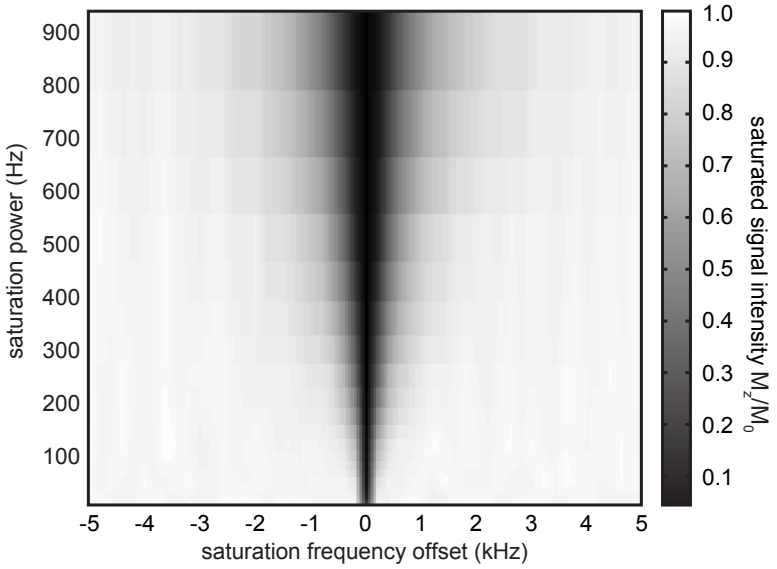

Figure 4.9: Effective bandwidth of cw saturation. Continuous wave pulses of varying applied field strengths B_1 were applied at the ^{1}H resonance frequency of an aqueous sample of 1 mM Gd-DTPA for 500 ms each. Black shading indicates complete saturation of the water signal. As the cw pulse power is increased, the effective bandwidth of saturation increases—at $B_1 \approx 900$ Hz, 10% or more of the signal is saturated over a bandwidth of ∼6 kHz.

In our saturation experiments using the 1 mM Gd-DTPA aqueous solution, pulses calculated to have 50 Hz and 200 Hz bandwidth at canonical power levels

were used. Each pulse pattern was repeated without any inter-pulse delays for the duration of the saturation period. The saturation profiles for each of these pulses are shown in Figure 4.10. Despite a slightly longer pulse duration and higher power deposition than the Gaussian and SEDUCE pulses, the d-SNOB pulse provides the most efficient saturation in the narrowest bandwidth. For the 200 Hz d-SNOB pulse, 90% saturation extended ±325 Hz from the center frequency with 85% saturation being achieved within the desired bandwidth of the pulse; for the 50 Hz d-SNOB pulse, 90% saturation extended ±75 Hz from the center frequency with 80% saturation being achieved within the desired bandwidth. We investigated the effects of the pulse phase supercycle MLEV-4 on the saturation profile [94] and found them to be insignificant for this arrangement of hardware and sample. Consequently, we did not rigorously investigate the effect of phase supercycles on exchanging xenon systems. Finally, because our goal was primarily to compare cw saturation transfer to multiple pulse saturation sequences, we decided to investigate only a subset of the many similar pulse shapes that might be used as building blocks of other saturation pulse trains. Parameters for all pulses are detailed in figure captions.

Saturation of ^{129}Xe

We performed similar saturation experiments on an aqueous solution of a xenon host molecule, cryptophane-A cage, and observed magnetization transfer via CEST. The cage, modified to bear an acetate group as a chemical handle for covalent functionalization, was conjugated to the pentapeptide EEEEK to increase the aqueous solubility of the molecule [95]; the solutions used in these experiments had a cage concentration of 50 μM. Hyperpolarized xenon was bubbled into the cage solution prior to each acquisition. At external field strength B_0 = 7.05 T, the frequency corresponding to xenon in cage (Xe@cage) is approximately 11 kHz upfield of the resonance of xenon dissolved in water (Xe_{aq}). Saturation profiles were collected by applying both d-SNOB and Gaussian pulses at frequencies near the Xe@cage frequency; the SEDUCE pulse was not tested because of its larger saturation bandwidth in the control experiments using water.

For comparison of the effective saturation bandwidth, both a high power and a low power cw pulse were applied at the Xe@cage frequency. Their effects are shown in Figure 4.11. The cw pulses have 90% saturation bandwidths of 5800 Hz and 1200 Hz for high and low power, respectively. In contrast, the 200 Hz bandwidth pulses had 90% saturation bandwidths of 1300 Hz (Gaussian) and 1000 Hz (d-SNOB), and the 50 Hz bandwidth pulses had 90% saturation bandwidths of 475 Hz (Gaussian) and 1275 Hz (d-SNOB). The results of these

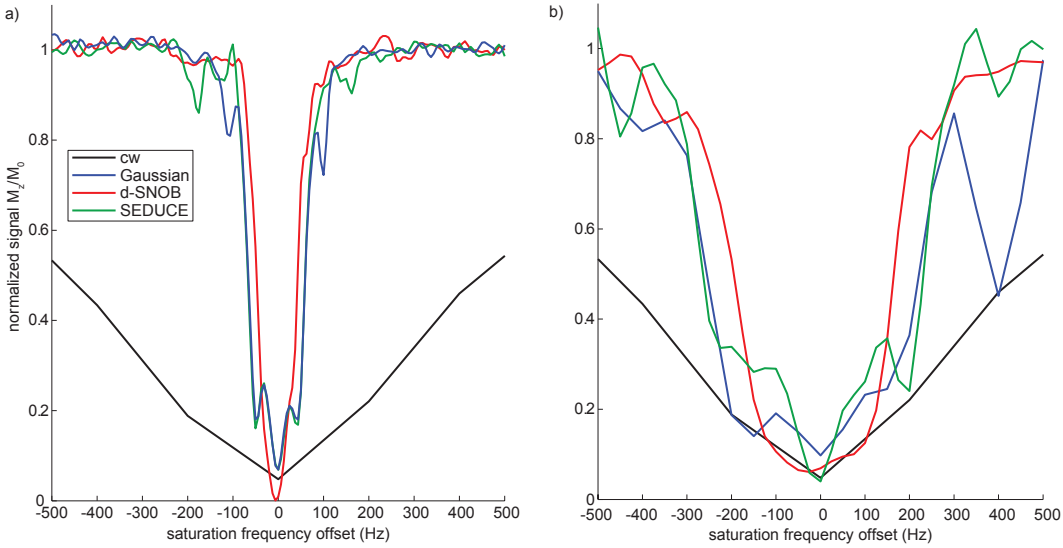

Figure 4.10: Effective saturation bandwidth for shaped and cw saturation pulses in water with frequency offsets relative to the ^{1}H resonance frequency. The cw pulse was applied for 500 ms with an applied field strength $B_1 = 498$ Hz. a) 50 Hz Gaussian (18.0 ms, $B_1 = 70.3$ Hz, 900 ms total saturation time), d-SNOB (56.4 ms, $B_1 = 62.6$ Hz, 564 ms total saturation time), and SEDUCE (17.25 ms, $B_1 = 62.6$ Hz, 431 ms total saturation time) pulses show at least 10% saturation of the water signal in an aqueous solution of 1 mM Gd-DTPA over ∼200 Hz. b) 200 Hz Gaussian (4.5 ms, $B_1 = 314$ Hz, 225 ms total saturation time), d-SNOB (14.1 ms, $B_1 = 249$ Hz, 423 ms total saturation time), and SEDUCE (4.31 ms, $B_1 = 249$ Hz, 129 ms total saturation time) pulses show at least 10% saturation of the water signal in the same solution over >600 Hz.

experiments are shown in Figure 4.11. We note that saturation transfer is optimized when these sequences are applied slightly off-resonance (approximately 125 Hz) from the expected Xe@cage resonance frequency. In addition, as illustrated in Figure 4.12, multiple pulse decoupling sequences can generate similar or even more contrast than can cw pulses at a lower average power level.

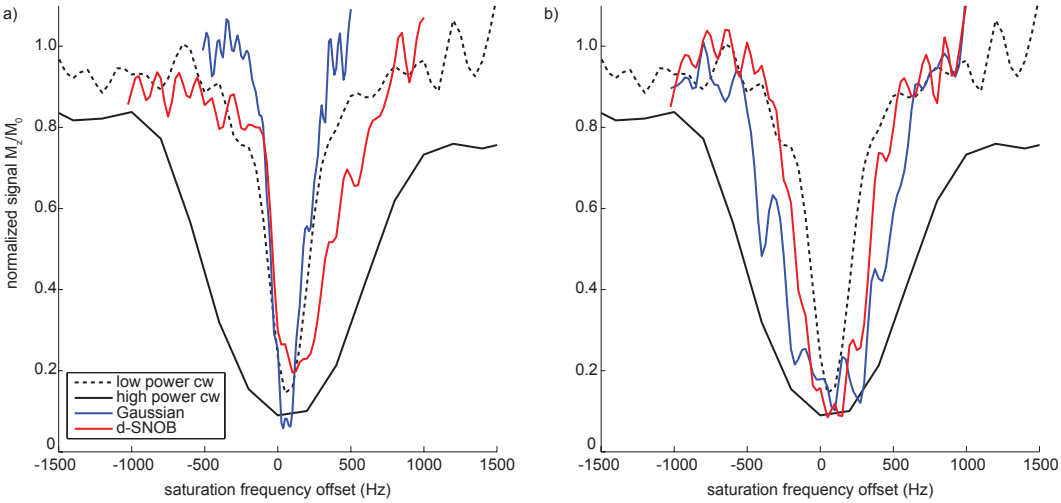

Figure 4.11: Effective saturation bandwidth for shaped and cw saturation pulses in the solution containing hp-^{129}Xe and cryptophane-A. Offsets are relative to the Xe@cage resonance frequency. For comparison, two cw pulses are shown: a low-power pulse (B_1 = 113 Hz, 1.5 s saturation) and a high-power pulse (B_1 = 449 Hz, 2.0 s). a) 50 Hz Gaussian (18.0 ms, B_1 = 80.0 Hz, 2.52 s total saturation time) and d-SNOB (56.4 ms, B_1 = 63.3 Hz, 2.26 s total saturation time) pulses show at least 10% saturation of the Xe_{aq} signal in an aqueous solution of 50 μM cryptophane-A over >475 Hz. b) 200 Hz Gaussian (4.5 ms, B_1 = 318 Hz, 1.35 s total saturation time) and d-SNOB (14.1 ms, B_1 = 252 Hz, 1.13 s total saturation time) pulses show similar saturation over >1000 Hz.

We next demonstrated the utility of band-selective saturation transfer in an exchanging xenon sensor system subject to homogeneous and inhomogeneous broadening. This conjugate, called MS2CA, is an engineered nanoparticle in which approximately 125 cryptophane cages have been covalently attached to an MS2 viral capsid scaffold [96]. (See also Chapter 8.) The capsid surface has 32 pores, each 2 nm in diameter, that facilitate solvent exchange in and out of the capsid. The resulting particle inherits all the favorable properties of the viral capsid, including biocompatibility, stability, and host targeting, and so is important in our effort to use xenon molecular sensors for *in vivo* bioimaging. We used a 7 nM solution of MS2CA (assembled capsids, corresponding to 900 nM cryptophane-A cages). To this solution, we applied saturation pulses,

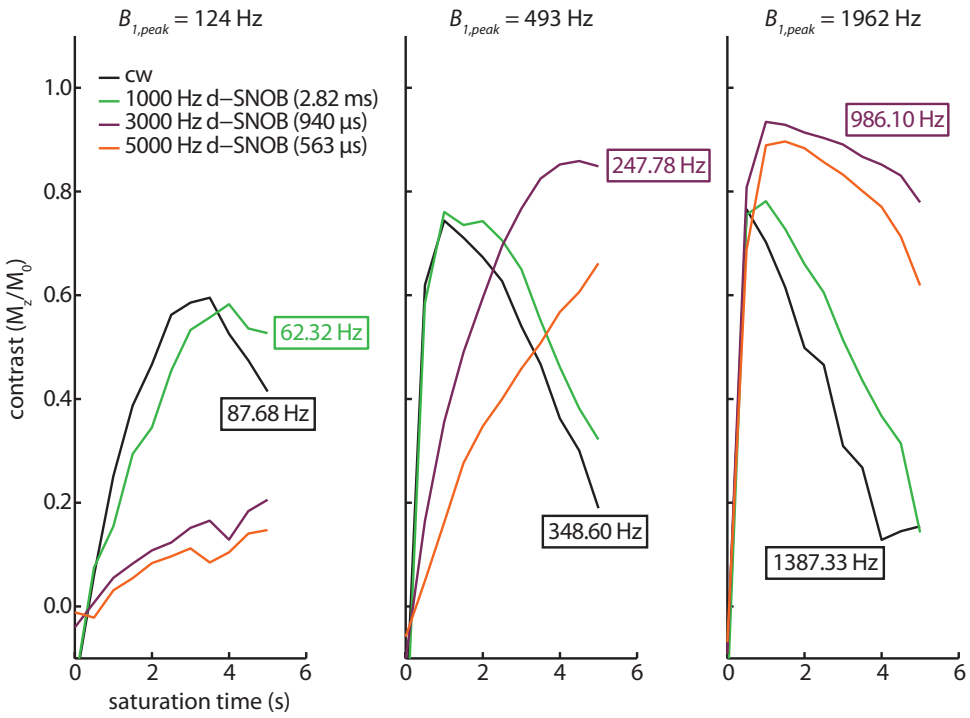

Figure 4.12: Experimental results showing the contrast generated using cw and d-SNOB pulses at different pulse powers. At lower pulse powers, lower bandwidth d-SNOB (1000 Hz bandwidth) and cw pulses provide the best contrast, while at higher powers, shorter d-SNOB pulses (3000 and 5000 Hz bandwidth) provide the greatest contrast. Saturation was applied on-resonant to a sample of 70 μM CryA in benzyl alcohol at the peak power B_1 and saturation time indicated. The rms power of the cw pulse is 70.7% of the peak power, and the rms power of the d-SNOB pulses is 50.3% of the peak power; the rms power for both cw and d-SNOB pulses is indicated in the boxes.

both cw and d-SNOB (100 Hz bandwidth), incrementally varying the frequency to measure saturation transfer spectra. Collected at frequencies between the Xe_{aq} and Xe@cage resonances, these indirectly detected spectra are shown in Figure 4.13.

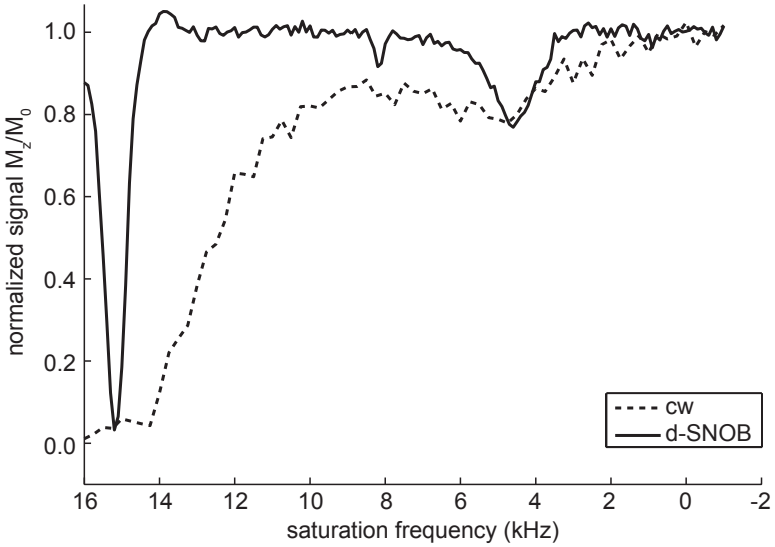

Figure 4.13: The resolution of a z-spectrum showing magnetization transfer after saturation is greatly improved by using frequency selective d-SNOB pulses. The z-spectra collected with both cw ($B_1 = 622$ Hz, 20 s saturation) and d-SNOB (100 Hz bandwidth, $B_1 = 78.3$ ms, 10.2 s total saturation) show comparable saturation of both the Xe_{aq} peak (∼15 kHz) and the Xe@cage peak (∼4 kHz). However, only in the d-SNOB z-spectrum is the baseline between the two resonances clearly discernible. Furthermore, the d-SNOB saturation sequence deposits approximately thirty times less power into the sample than does cw saturation.

When optimized, the saturation transfer contrast under cw irradiation at the Xe_{aq} frequency was comparable to that resulting from the d-SNOB saturation; however, the d-SNOB saturation required much less power and a shorter saturation timein fact, the power deposited with the d-SNOB pulses was approximately thirty times less than that deposited with the cw pulse. In addition, the resolution of the indirectly detected spectrum is superior, as evidenced by the visibility of the baseline between the Xe_{aq} and Xe@cage peaks in the d-SNOB spectrum.

Hyper-CEST Imaging Experiments

To demonstrate the utility of these frequency selective saturation pulses in saturation transfer imaging, we conducted prototype imaging experiments

of a phantom consisting of two tubes of water, placed in a one-dimensional gradient for excitation and detection of one-dimensional images. Specifically, we placed two 10-mm NMR tubes (phantoms) adjacent to one another in a 30-mm probe, following the manner in [76], as shown schematically in Figure 4.14a. The solvent in both phantoms was benzyl alcohol to increase the solubility of both xenon and cryptophane-A. The left phantom (#1) contained 0.5 mM cryptophane-A while the right phantom (#2) contained none. The spectra are excited and detected in the presence of a linear magnetic field gradient to produce a one-dimensional image of the phantom. Figure 4.14b shows a one-dimensional ^{129}Xe NMR profile, verifying separation between the two phantoms. We applied a series of 200 Hz bandwidth d-SNOB pulses at various points in the spectrum as shown in Figures 4.14c–4.14h. When saturation was applied at the frequency corresponding to xenon dissolved in benzyl alcohol ($Xe_{solvent}$), a hole was burned into the profile of the appropriate phantom (Figures 4.14c and 4.14d). When saturation was applied at the Xe@cage frequency (11 kHz upfield of the $Xe_{solvent}$ frequency) a hole was burned into the profile of phantom #1, which contained cryptophane-A, but not into that of phantom #2. To verify that the hole burning in the above experiments was not due to direct saturation of the $Xe_{solvent}$ peak, we applied off-resonant saturation pulses at frequencies 11 kHz downfield of the $Xe_{solvent}$ resonances (Figures 4.14g and 4.14h). Neither off-resonant case showed saturation of the ^{129}Xe signal. We therefore anticipate that these band-selective saturation transfer sequences can form the basis of spectral-spatial selective imaging or Hadamard imaging schemes based on multispectral excitation.

We have demonstrated that band-selective saturation sequences allow independent optimization of the parameters governing chemical shift saturation transfer experiments. The selectivity and efficiency of saturation using the sequences demonstrated above is superior to conventional approaches based on cw radiation, and the effective bandwidth of saturation is tunable over a wide range by manipulating the pulse duration and power. While we have only examined d-SNOB and Gaussian pulse trains for xenon systems, it is possible that other sequences based on rotating frame saturation or dephasing will yield superior results. Also, Shinnar-Le Roux pulses, algorithmically designed to have well defined excitation bandwidths and low peak powers, merit investigation in xenon-exchange experiments [97, 98]. In addition, the power required to achieve saturation with these shaped pulses is significantly reduced, which may be relevant in applications where SAR limitations become restrictive. Alternatively, in experiments *in vitro* in which SAR is not limiting, new detection thresholds for xenon-based molecular sensors may be achieved by generating more saturation per time in the magnetization transfer system.

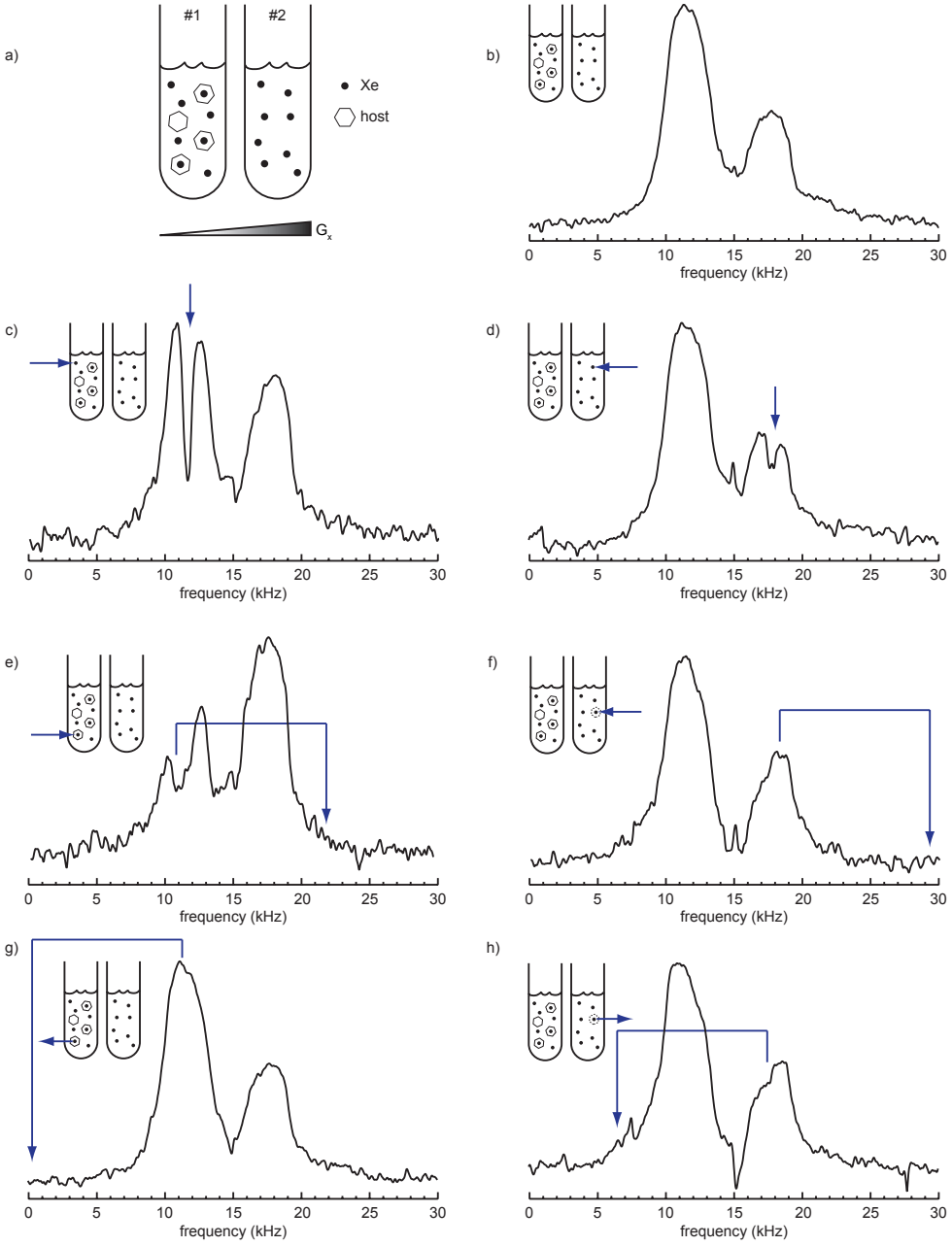

Figure 4.14: Frequency selective saturation transfer pulses applied to imaging. a) The apparatus consists of two 10-mm NMR phantoms side-by-side in a 30 mm probe. Only the left phantom (#1) contains cryptophane-A. b) A one-dimensional profile of the two phantoms. The difference in intensity is due to a mismatch in the delivery of hp-^{129}Xe to the two phantoms. c–h) Saturation applied at various frequencies as indicated by arrows in the figure, or explained in the text. The vertical scale is not constant for (b) through (h).

Such sequences may also form the building blocks of imaging methods that require simultaneous control over the spectral and spatial extent of saturation, or those which require saturation at multiple simultaneous frequencies. We did not explore applications to conventional CEST contrast agents here but anticipate that similar considerations will apply in those experiments.

Experimental Details

All experiments were performed using a 7.05 T NMR spectrometer (Varian Inc., Palo Alto, CA) with 5 mm (saturation profiles, MS2CA) and 30 mm (imaging) probes. The imaging probe was highly optimized for xenon performance at the expense of performance on the ^{1}H channel. Imaging experiments were conducted using a gradient coil assembly (Resonance Research Inc., Billerica, MA) for spatial encoding. For the one-dimensional profiles, the applied gradient field strength was 3.4 G cm^{-1}. Gaussian, SEDUCE, and d-SNOB pulse profiles were generated using the default pulse profiles and the *pxshape* tool in the VNMR software package (Varian Inc.). Each pulse was checked for proper behavior, either excitation or inversion, and the pulse power was adjusted by up to $\pm$1 dB accordingly. Individual pulse durations and powers are given in appropriate figure captions.

Hyperpolarized ^{129}Xe ($P \approx 4\%$) was generated with a XenoSpin polarizer (Amersham Health, Durham, NC) using a mixture of 1% (saturation profiles) or 2% (MS2CA, imaging) xenon (natural abundance ^{129}Xe), 10% N_2, and the balance He (Airgas, Radnor, PA). Xenon was delivered to the NMR phantoms using a bubbling setup as previously described [99]. When performing imaging experiments, the xenon delivery system was modified to deliver pressurized gas to two phantoms simultaneously. For the saturation profile experiments, shown in Figure 4.14, xenon was bubbled into the phantoms at $\sim$70 psi pressure for 10 s at 0.35 standard liters per minute (SLM), followed by a 1 s stopped-flow delay to allow dissipation of bubbles in the phantom prior to acquisition. For experiments involving MS2CA, xenon was bubbled at $\sim$70 psi pressure for 20 s at 0.3 SLM, followed by a 4 s settling delay prior to acquisition. For imaging experiments, xenon was bubbled at $\sim$60 psi pressure for 10 s at 0.65 SLM, followed by a 2 s settling delay prior to acquisition.

For xenon experiments involving saturation profiles and the MS2CA conjugate, the Xe@cage resonance was not directly visible in the spectra. Consequently, the Xe@cage frequency was found by incrementally varying the frequency of a saturation pulse in the region between the $Xe_{solvent}$ resonance and the Xe_{gas} resonance (0 ppm) and monitoring saturation transfer to the

$Xe_{solvent}$ signal. Using this method, the frequency of the Xe@cage resonance was determined to an accuracy of ±25 Hz (saturation profiles) or ±50 Hz (MS2).

For each acquisition, the appropriate excitation pulse was followed by an acquisition time of 1 s (^{1}H experiments), 500 ms (xenon saturation profiles), 200 ms (MS2), or 100 ms (xenon imaging). Four transients were collected for xenon saturation profiles and for imaging experiments. Post-processing was performed in NMRPipe [100] and included the following procedures:

- baseline correction of the FID
- left-shifting of points at the beginning of the FID, as necessary
- application of a cosine-bell apodization filter
- application of line broadening
- zero filling
- Fourtier transformation
- phasing of the spectrum
- baseline correction of the spectrum

A representative NMRPipe script showing this procedure as well as export of the data to a text file is shown below.

```
#!/bin/csh

nmrPipe -in test.fid \
  | nmrPipe  -fn POLY -auto -ord 1 \
  | nmrPipe  -fn LS -ls 3 \
  | nmrPipe  -fn SP -off 0.5 -end 1.00 -c 0.5 \
  | nmrPipe  -fn EM -lb 11 \
  | nmrPipe  -fn ZF -auto \
  | nmrPipe  -fn FT -auto \
  | nmrPipe  -fn PS -p0 129.8  -p1 -227.2 -di \
  | nmrPipe  -fn POLY -auto -ord 2 \
     -out 01Mar2011_3.ft2 -verb -ov

pipe2txt.tcl -real 01Mar2011_3.ft2 > \
 01Mar2011_3.txt
```

Similar scripts are used for all NMRPipe processing.

Following spectral processing in NMRPipe, integration and normalization of the $Xe_{solvent}$ peak area for *Z-spectra* was done using MATLAB® (The MathWorks Inc., Natick, MA).

Chapter 5

Xenon-based Molecular Sensors in Lipids[1]

> "The more people go out of their way to tell you that you are wrong or what you're doing can't possibly work, the more likely you are onto something big."
> —Paul Lauterbur, quoted by Jeff Tsao, 2008

Xenon-based molecular sensors can be conjugated with a moiety that confers chemical specificity for binding to a particular analyte; examples of such binding moieties are biotin or avidin [77], oligonucleotides or aptamers [101, 102], or enzyme substrates [103]. Binding to a molecular target causes localization of the sensor in regions containing the analyte, making it possible to image the target of chemical interest [104]. While there is great potential in using these sensors for targeted molecular imaging *in vivo*, for example, in the determination of distributions of cell surface receptors [102], their non-specific interactions with many biological materials are poorly understood. Some interaction between the hydrophobic xenon-binding moiety (a cryptophane molecule) that has been targeted to a cell surface receptor and the hydrophobic interior of the cell membrane is likely. Studies have been conducted on cryptophanes in hydrophobic organic solvents [71, 78] and in human plasma [105], but there has been no previous report on the interaction of cryptophanes with lipid vesicles.

We investigated interactions between cryptophane and lipid vesicles that are comparable in size and composition to cell membranes [22] using xenon NMR; the system is shown schematically in Figure 5.1. Lipid vesicles have been successfully used as carrier agents for xenon (without cryptophane-based sensors) in MR angiography [22] and in MR imaging of the rat brain [106];

[1] This chapter is based on [76].

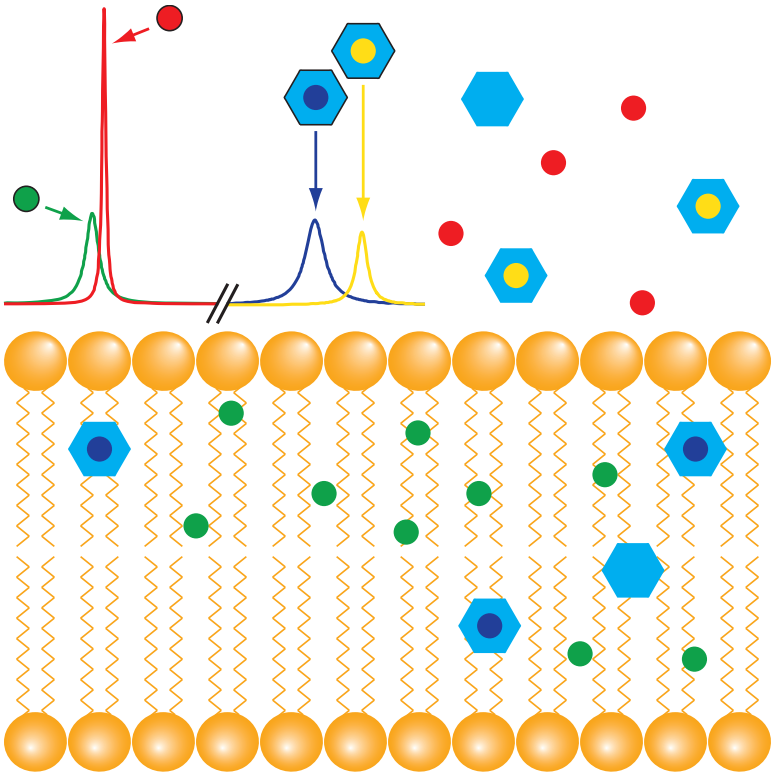

Figure 5.1: A schematic of the various pools of xenon in this study. Xe_{lipid} (green) and Xe_{aq} (red) correspond to unbound xenon. $Xe@cage_{lipid}$ (dark blue) and $Xe@cage_{aq}$ (yellow) appear ∼130 ppm upfield of the Xe_{aq} peak.

these and other reports [107, 108] indicate that xenon is more soluble in lipids than in water. (Table 2.1 quantifies xenon solubility in emulsions that mimic natural lipids.) In addition, we hypothesized that cryptophane, a hydrophobic molecule, would show greater solubility in a lipid emulsion than in pure water. The increased solubility of both xenon and the sensor is advantageous in maximizing signal. Furthermore, we hoped to resolve the signals corresponding to free xenon dissolved in both aqueous and lipid environments, as well as the signals corresponding to xenon bound in the sensor in both aqueous and lipid environments. We wanted to extend other work [95, 109] involving the temperature dependence of the chemical shift values for these signals. Lastly, we predicted that we could selectively image the sensor in aqueous and lipid environments, illustrating the application of xenon-based molecular sensors to targeted imaging in biological mixtures.

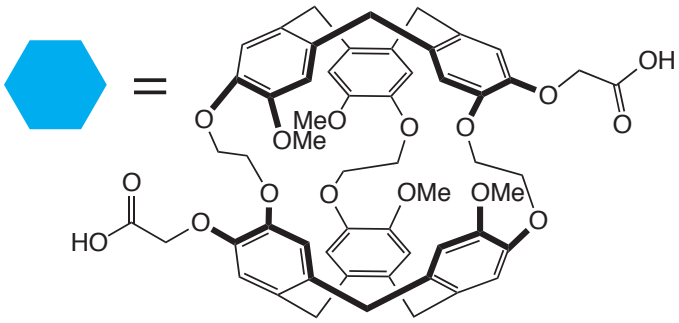

Figure 5.2: The cage is represented by the light blue hexagon in Figure 5.1. The modified cryptophane cage used in these studies is termed "diacid cage". The introduction of two acetate groups confers some water solubility to this otherwise hydrophobic molecule.

Lipid Suspensions and Aqueous Solutions

In all experiments reported here, we used a variant of cryptophane-A cage (Figure 5.2) as a xenon host. This cage molecule has acetate groups chemically attached to its exterior, conferring partial solubility in the aqueous phase of the suspension; we refer to this cryptophane compound as diacid cage. A saturated aqueous solution has 15 ± 5 μM of the diacid cage, as determined by UV-vis absorbance ($A_{287\,nm} = 8000\,M^{-1}cm^{-1}$) [81].

The NMR spectrum of xenon bubbled into pure water shows peaks corresponding to gaseous xenon (referenced to 0 ppm) and to xenon dissolved in water (Xe_{aq}) at 189 ppm. Figure 5.3 shows the xenon NMR spectrum of diacid cage in water (black), with resonances at 62 and 189 ppm, corresponding to xenon bound in the cryptophane cage in an aqueous environment ($Xe@cage_{aq}$) and free xenon in aqueous solution (Xe_{aq}), respectively. These shifts are consistent with those reported elsewhere [77].

The spectrum of diacid cryptophane in a 1% lipid suspension (red in Figure 5.3) showed three resonances: the two found in the pure aqueous solution and a third resonance at 73 ppm. We attribute this third resonance to that of xenon bound in the cryptophane cage in a lipid environment ($Xe@cage_{lipid}$). The integrated areas of the Xe@cage peaks in the 1% lipid suspension give relative signal intensities of 1:2 ($Xe@cage_{lipid}$:$Xe@cage_{aq}$). Because this ratio is much larger than the lipid/water volume ratio (1:100), we estimate that diacid cage is at least fifty times more soluble in lipid than in water. As previous data show that the binding affinity of xenon for the cage in water is greater than in an apolar solvent [75], it is unlikely that the 1:2 ratio of the $Xe@cage_{lipid}$:$Xe@cage_{aq}$ signals can be explained by a greater fraction of cages containing xenon in the lipid phase. With 5% and 2% lipid suspensions, both $Xe@cage_{aq}$ and

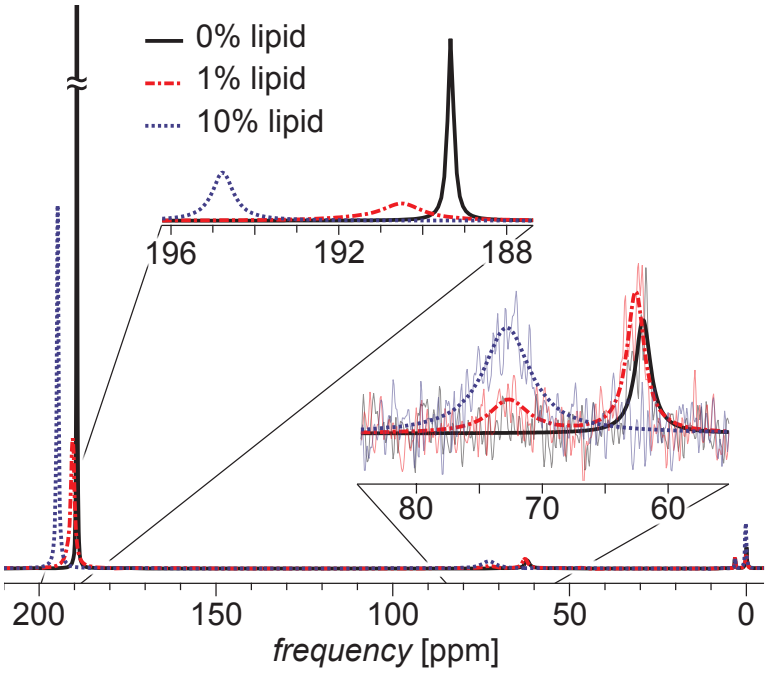

Figure 5.3: Xenon NMR spectra of the diacid cage in samples of 0% (black), 1% (red), and 10% (blue) lipid content. The peaks at ∼190 ppm correspond to the Xe_{aq} and Xe_{lipid} peaks, while the peaks at 63 and 73 ppm correspond to $Xe@cage_{aq}$ and $Xe@cage_{lipid}$, respectively.

the $Xe@cage_{lipid}$ peaks were clearly visible, but when the lipid content was increased to 10%, only one peak was observed: $Xe@cage_{lipid}$ at 73 ppm (blue in Figure 5.3). The ratio of peak intensities, $Xe@cage_{lipid}$:$Xe@cage_{aq}$, for the 2% and 5% lipid suspensions was 0.9:1 and 1.6:1, respectively. This increase of the $Xe@cage_{lipid}$:$Xe@cage_{aq}$ ratio with lipid content verifies the preferential partitioning of cage and xenon into the aliphatic lipid environment.

Beyond the changes in the Xe@cage peaks due to lipid content, we note that the peak at 189 ppm shifts downfield and is broadened upon addition of the lipid. We fitted this region of the spectrum using two Lorentzian curves, representing the Xe_{aq} and Xe_{lipid} peaks. These fits show a broad peak ∼1 ppm downfield of a narrower, more intense peak. We attribute the more intense peak to Xe_{aq} because it has a chemical shift value closer to that of Xe_{aq} from the 0% lipid solution. The chemical shift value for the Xe_{aq} peak increases with increasing lipid content; this effect, reported previously with proteins [65], is a result of weak surface interactions between xenon atoms and other molecules in solution. The observation of distinct Xe_{aq} and Xe_{lipid} peaks indicates that these two pools exchange slowly on the chemical shift timescale. While the integrated

areas of the solvent peaks do not show a quantitative relationship with the lipid content of a given sample, a trend of increasing Xe_{lipid} peak area with increasing lipid content is observed. The lack of quantitative agreement is probably due to error in the fits resulting from the large difference in the intensities of the two fitted peaks. Nevertheless, the fit parameters yield systematic trends for the chemical shift values of both the Xe_{aq} and Xe_{lipid} peaks, supporting the validity of the fits; a graphical example of the fits used is shown in Figure 5.4, while tables detailing all fit parameters are shown in Appendix C. Interestingly, we note that the chemical shift separation between the xenon signals in aqueous and lipid environments without the cage (∼1 ppm) is ten times smaller than the separation with the cage (∼10 ppm). This ability of a host molecule to amplify the chemical shift separation may be useful in determining the local chemical environment of the cage and other molecules to which the cage may be bound.

Temperature Dependence

We explored the temperature dependence of xenon-based molecular sensors in lipid suspensions at temperatures from 5 °C to 40 °C. Following initial equilibration at room temperature, samples were allowed to equilibrate for 5 min at each temperature point before data acquisition. At temperatures below 25 °C, the Xe_{lipid} peaks for the 1%, 2%, and 5% lipid suspensions were distinguishable from the Xe_{aq} peaks, as shown in Figure 5.5. However, at temperatures above 25 °C the peaks overlapped and could not be fitted unambiguously. Generally, the position of the Xe_{aq} peak varied quadratically with temperature, as has been reported previously [110], while the position of the Xe_{lipid} peak decreased with increasing temperature. The chemical shift values of the $Xe@cage_{aq}$ and $Xe@cage_{lipid}$ peaks showed a linear increase with temperature—the slope of the $Xe@cage_{aq}$ shift was consistent with previous results at 0.31 ± 0.01 ppm $°C^{-1}$ [95], and that of the $Xe@cage_{lipid}$ peak was 0.18 ± 0.03 ppm $°C^{-1}$. Plots of chemical shift values at different temperatures are available in Figures 5.6 and 5.7.

Saturation transfer

When using xenon-based molecular sensors in mixed aqueous/lipid environments, exchange among four distinct xenon pools affects the system, illustrated schematically in Figure 5.1. To qualitatively characterize these exchange pathways between the different pools, we used the Hyper-CEST detection method [1], in which a decrease in the Xe_{aq} signal following saturation at the Xe@cage

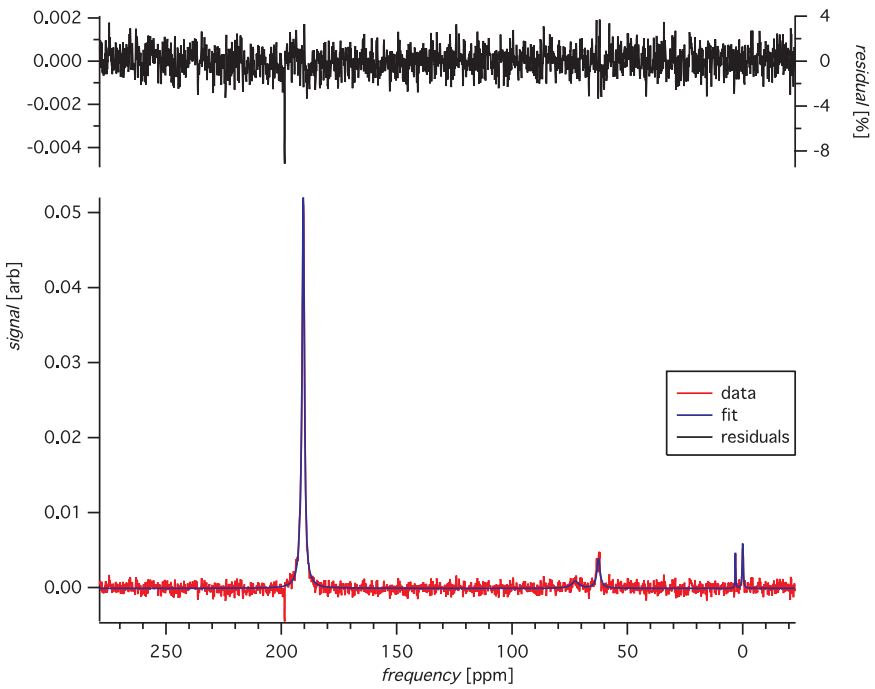

Figure 5.4: An example of the fits used for these data. The multiple Lorentzian peaks are fit to a ^{129}Xe spectrum of a 1% lipid suspension at 25 °C. The peak referenced to 0 ppm is the Xe_{gas} signal. The smaller peak at ∼3 ppm is Xe_{gas} trapped in the capillaries that are used for delivering gas to the sample. This peak is not in exchange with the rest of the system and does not affect the exchange properties under investigation. The two small peaks at ∼65 and ∼75 ppm are the Xe@cage$_{aq}$ and Xe@cage$_{lipid}$ signals, respectively. The large peak at ∼190 ppm is the signal from xenon dissolved in suspension, either Xe_{aq} or Xe_{lipid}. Fits were made with the built-in fit routines in the IGOR Pro 6.1 software package (WaveMetrics Inc., Lake Oswego, OR).

frequency occurs in the presence of the molecular sensor. In our experiments, saturation pulses were 500 ms in duration, much longer than the 30 ms residence time of xenon atoms reported for cryptophane cage in water [81], and were designed to have a bandwidth of ∼1.8 ppm (150 Hz at 7.05 T) [87].

As shown in Figure 5.8, when a saturation pulse was applied at a frequency far off resonance from the Xe@cage signals (spectrum f), no change was observed in the signal intensity of any peak. When the pulse was applied at frequencies at or near the Xe@cage peaks, saturation was observed to varying degrees in other peaks. The results of these saturation transfer experiments are summarized in Table 5.1. The transfer of saturation between the lipid and aqueous pools indicates chemical exchange of xenon between these two environments on the time scale of the applied saturation pulse (500 ms). The difference in

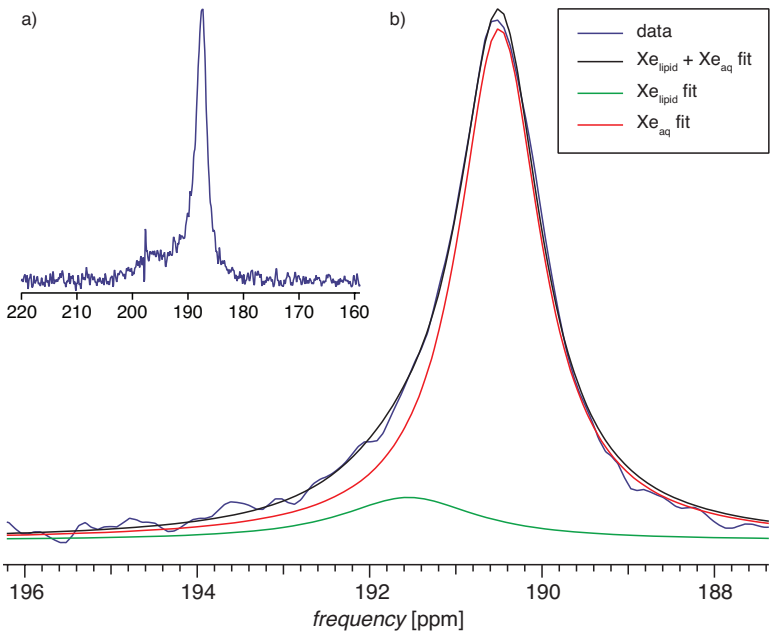

Figure 5.5: A spectrum of a 2% lipid sample cooled to 1 °C. Two peaks around 190 ppm, corresponding to Xe_{aq} and Xe_{lipid}, confirm that these two chemical environments are distinguishable. The spike at ∼198 ppm is an artifact from the spectrometer. (b) An example of the multiple-peak fits used to distinguish the Xe_{aq} and Xe_{lipid} peaks around 190 ppm. The data (blue) are fit to a sum of Xe_{aq} (red) and Xe_{lipid} (green) peaks. The total fit is shown in black.

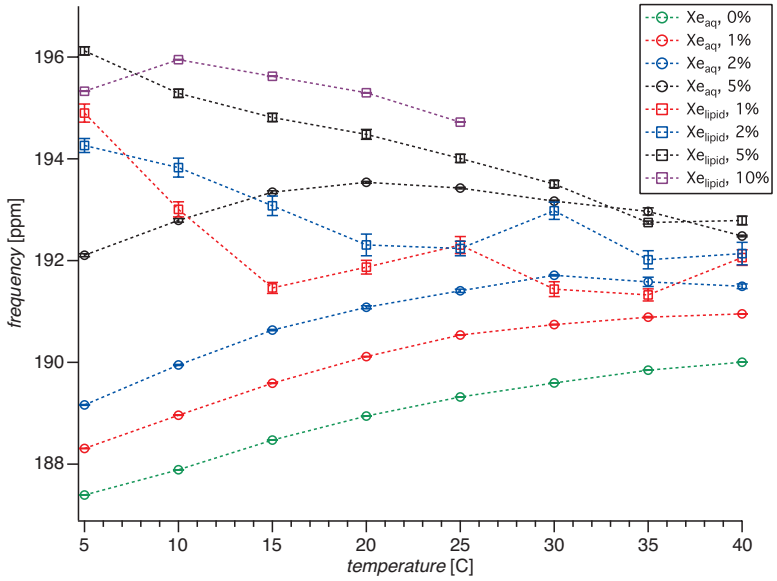

Figure 5.6: The chemical shift values of the Xe_{aq} and Xe_{lipid} peaks in 0%, 1%, 2%, 5%, and 10% lipid samples as a function of temperature. The peak positions are determined from multiple peak fits shown in Appendix C. The position of the Xe_{aq} peak varies quadratically with temperature.

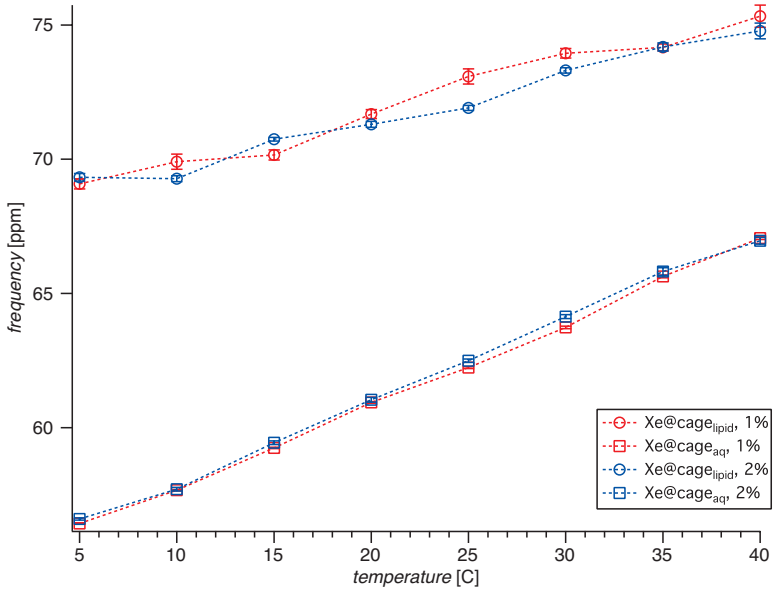

Figure 5.7: The chemical shift values of the Xe@cage peaks in the 1% and 2% lipid samples as a function of temperature. The peak positions are determined from the fits given in Appendix C. Both the $Xe@cage_{aq}$ and $Xe@cage_{lipid}$ peaks increase with increasing temperature at 0.31 ± 0.01 ppm $°C^{-1}$ and 0.18 ± 0.03 ppm $°C^{-1}$, respectively.

the degree of saturation as a result of pulses applied at the Xe@cage$_{aq}$ vs. Xe@cage$_{lipid}$ frequencies indicates more rapid exchange of xenon in and out of the cage in the lipid phase than in water. This observation is consistent with the linewidths of the Xe@cage peaks; the linewidth of the Xe@cage$_{lipid}$ peak, a property indicative of the exchange rate, is two to five times wider than that of the Xe@cage$_{aq}$ peak in both the 1% and 2% lipid samples (see Appendix C). Ultimately, higher concentrations of both xenon and cage in the lipid environment, together with more rapid exchange, result in more efficient Hyper-CEST saturation in lipid environments using xenon-based molecular sensors. This increased saturation efficiency could be used to improve xenon NMR detection sensitivity in lipophilic systems.

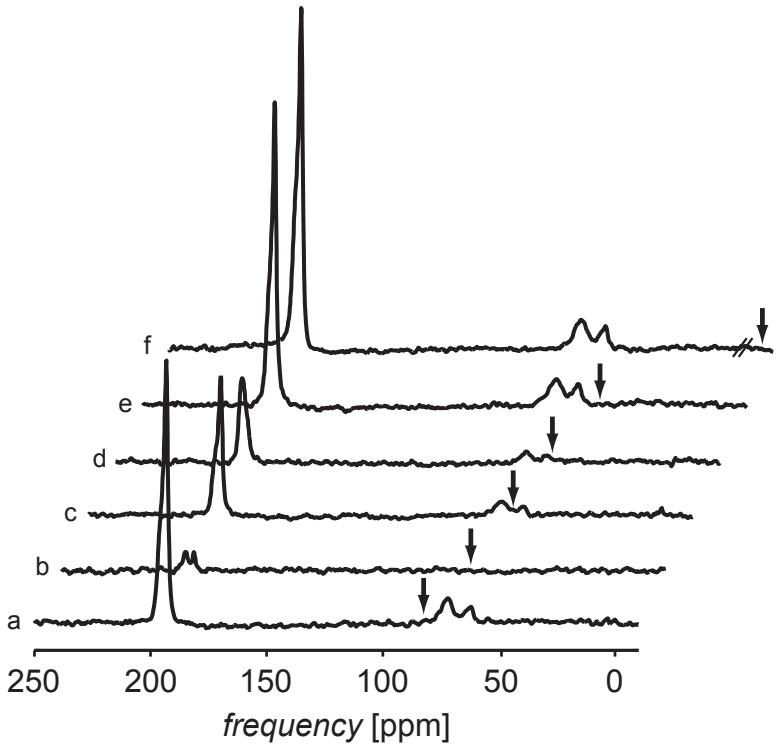

Figure 5.8: The xenon NMR spectra following Hyper-CEST saturation at different saturation frequencies as indicated by the small arrows. Saturation is most apparent when saturating directly on the Xe@cage peaks (spectra b and d), especially the Xe@cage$_{lipid}$ peak. When saturating the Xe@cage$_{lipid}$ peak (spectrum b), the individual Xe$_{aq}$ and Xe$_{lipid}$ peaks become apparent due to the reduction in peak intensity.

Table 5.1: Integrated peak areas of a xenon-NMR spectrum of a 1% lipid suspension following saturation at various frequencies. Letters designating the saturation frequency correspond to the spectra in Fig. 5.8.

Saturation frequency	Xe_{lipid}	Xe_{aq}	$Xe@cage_{lipid}$	$Xe@cage_{aq}$
a (-432.8 ppm)	1.00[a]	0.93	0.36	0.18
b (49.7 ppm)	0.82	0.81	0.39	0.15
c (59.4 ppm)[c]	0.58	0.05	0.11	0.09
d (64.3 ppm)	0.40	0.37	0.21	0.06
e (69.1 ppm)[d]	0.10	0.05	0.00[b]	0.00[b]
f (88.6 ppm)	0.82	0.65	0.32	0.14

[a] All peak areas normalized to this value.
[b] No observable peak at this frequency.
[c] This frequency corresponds to $Xe@cage_{aq}$.
[d] This frequency corresponds to $Xe@cage_{lipid}$.

Imaging

To demonstrate the applicability of frequency-selective Hyper-CEST detection to imaging, we combined saturation with phase-encoded imaging, as shown in Figure 5.9. When weak saturation pulses were applied resonant with either $Xe@cage_{lipid}$ or $Xe@cage_{aq}$, the response was total saturation of the Xe_{aq} and Xe_{lipid} peaks, verifying the presence of diacid cage (Figure 5.9a, c). In contrast, when saturation was applied at a frequency directly between those of the two cage peaks, insufficient contrast was generated to verify the presence of cage in the Hyper-CEST images (Figure 5.9b). This demonstrates the utility of frequency-selective saturation for detecting multiple molecular sensors with small frequency separations. Based on the unique response of the $Xe@cage_{aq}$ and $Xe@cage_{lipid}$ signals to saturation, we anticipate the development of multiplexing using xenon-based molecular sensors. Incorporating multiplexing with previously reported work on the detection of low concentrations of sensor [95] may provide a facile way to characterize an analyte with NMR in a way analogous to multiplexed optical detection using fluorophores.

The NMR signal enhancement resulting from increased amounts of xenon and sensor in lipid environments reduces sensitivity requirements for detection of analytes typically found in lipophilic media. The response of the Xe_{aq} and Xe_{lipid} peaks to saturation at frequencies corresponding to $Xe@cage_{aq}$ and $Xe@cage_{lipid}$ reduces these sensitivity requirements even further. In addition, differences in the chemical shift of xenon in the presence of molecular sensor facilitate the discrimination of the chemical environment of xenon, either

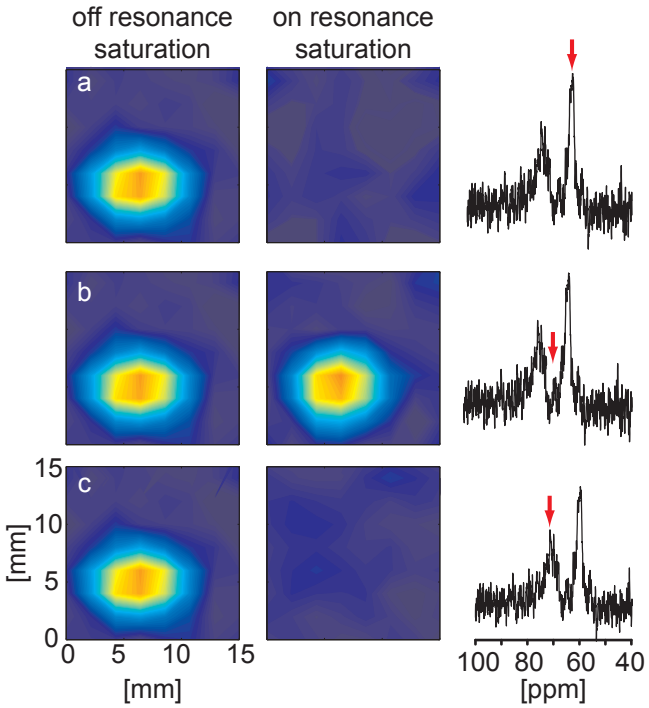

Figure 5.9: A demonstration of the selectivity of Hyper-CEST for imaging with the diacid cage in a 1% lipid suspension. When saturation is applied to either the Xe@cage$_{aq}$ (a) or Xe@cage$_{lipid}$ (c) peak, the response is diminished in the on-resonant case. When saturation is applied at a frequency between the two Xe@cage peaks (b), there is no apparent saturation in the image. The applied radio frequency field in these imaging experiments is approximately one-fifth the amplitude of that used in Fig. 5.8, giving increased selectivity.

aqueous or lipid, with greater frequency resolution than in the absence of sensor. Interestingly, xenon-based molecular sensors in lipid emulsions show a quantitative dependence on temperature; it is possible that a similar dependence on other solvent properties, for example, pH, will emerge in future experiments. By exploiting the response to both magnetization transfer and to physical and chemical properties of the local environment, sensors could be designed that simultaneously analyze several properties of a system of interest, for example, biological or other chemical markers, that appear in different concentrations in lipophilic and hydrophilic regions of the body.

Experimental Details

Dilute suspensions of lipid vesicles were prepared from a pharmaceutical grade lipid suspension (Intralipid 20%, Pharmacia) that contains vesicles

100–500 nm in diameter [106]. Lipid emulsion was diluted with water/D_2O (minimum 30% D_2O for frequency locking in the spectrometer) to 1%, 2%, 5%, and 10% lipid content. To each aliquot of this dilute lipid suspension (4.0 mL) was added a variant of cryptophane-A (2.0 ± 0.4 mg), termed diacid cage, with two methoxy groups each replaced by methyl carboxylic acid groups for increased water solubility. The concentration of diacid cage in the lipid suspension could not be directly measured during sample preparation because the lipid vesicles strongly scatter light. By allowing the sample to settle for ∼10 min after shaking and by pipetting from the top of the suspension, we avoided introducing powder into the NMR sample tubes; thus, the amount of dissolved cage was fixed for any given lipid concentration.

Data were recorded on a 7.05 T NMR spectrometer (Varian, Palo Alto, CA) using 5 mm and 10 mm (spectroscopy) and 30 mm (imaging) probes. Hyperpolarized xenon ($P \approx 4\%$) [34, 43] was generated with a XenoSpin polarizer (Amersham Health, Durham, NC) from a gas mixture of 89% He, 10% N_2, and 1% xenon with natural-abundance isotopes (Praxair) at ∼70 psi. Gas containing hp-^{129}Xe was bubbled (15–20 s, 0.45 SLM) into the NMR tubes containing sample (∼2.5 mL for the 10 mm probe, ∼1.0 mL for the 5 mm probe). Gas flow was interrupted using a stopped-flow system [99], followed by a delay (5–15 s) to allow the bubbles to dissipate. The temperature of the system was controlled using the variable temperature unit of the spectrometer. The Hyper-CEST experiments (5 mm probe) were conducted using a cw saturation period (500 ms, applied radio frequency field strength $B_1 = 2.23\,\mu$T), followed by a hard 90° pulse and readout of a free induction decay (50 ms). After application of an apodization filter and Fourier transformation, the xenon gas peak was referenced to 0 ppm in each spectrum for which a gas peak was present. All other spectra used the same reference for 0 ppm. Peaks were fitted to the data using the built-in fit routines in the IGOR Pro 6.1 software package (WaveMetrics Inc., Lake Oswego, OR).

Imaging experiments were conducted using a gradient coil assembly (Resonance Research Inc., Billerica, MA) for spatial encoding. Two 10 mm NMR tubes, one containing a 1% lipid suspension and the other containing a 5% lipid suspension, were each connected to the gas delivery system and placed side-by-side in a 30 mm NMR probe. When using two phantoms, the flow output of the polarizer was increased to 0.65 SLM. No attempt was made to compensate for differences in polarization output with increased flow. Hyper-CEST images were acquired using a cw saturation pulse (6 s, applied field strength $B_1 = 0.44\,\mu$T) and a slice-selective 90° pulse along the z-dimension (1.2 ms, SINC shape, 13.5 mm slice-thickness) with subsequent 2-dimensional phase encoding (15×30 mm^2 field-of-view, matrix size 4×8). Each point in k-space was read

out once for 1024 ms with 5 kHz spectral width. Post-processing using MATLAB®(The MathWorks Inc., Natick, MA) included two-dimensional FT for spatial reconstruction after zero-filling to an 8×16 dataset and one-dimensional FT for spectral reconstruction. Images showing the spatial distribution of the xenon signal at $\delta \approx 190$ ppm, shown in Figure 5.9, were generated by summation of the signal intensity over 5 data points ($\sim$0.74 ppm) in the absolute spectrum and subsequent color-encoding of these values; the whole image is cropped from a field-of-view of 30 mm $\times$ 15 mm to 15 mm $\times$ 15 mm to highlight only the phantom containing the 1% lipid suspension.

Chapter 6

Development of Temperature Imaging using Xenon-based Molecular Sensors[1]

> "Fortunately science, like that nature to which it belongs, is neither limited by time nor by space. It belongs to the world, and is of no country and of no age. The more we know, the more we feel our ignorance; the more we feel how much remains unknown; and in philosophy, the sentiment of the Macedonian hero can never apply—there are always new worlds to conquer. "
> —Sir Humphry Davy, 1825

Using simple chemical exchange of nuclei of a hyperpolarized reservoir in combination with a mechanism of gated transfer onto the molecule of interest, such as with Hyper-CEST, would provide optimized, controlled utilization of the hyperpolarization (Fig 6.1a), hence avoiding polarization losses during transfer reactions. Since exchange rates depend on the ambient temperature, this parameter allows for tuning the amplification achieved by transferring information from a low-concentration target pool onto the high-concentration reservoir pool. Here, we demonstrate implementation of this concept using molecular cages to host hp-^{129}Xe and apply this approach to non-invasive molecular temperature sensing.

When using temperature to control depolarization transfer, three effects should be considered: First, increasing temperature increases the exchange rate of xenon with the cage molecules [71, 75, 112]. Second, the binding constant of the cage-xenon complex tends to increase as temperature increases [105],

[1] This chapter is based on [111].

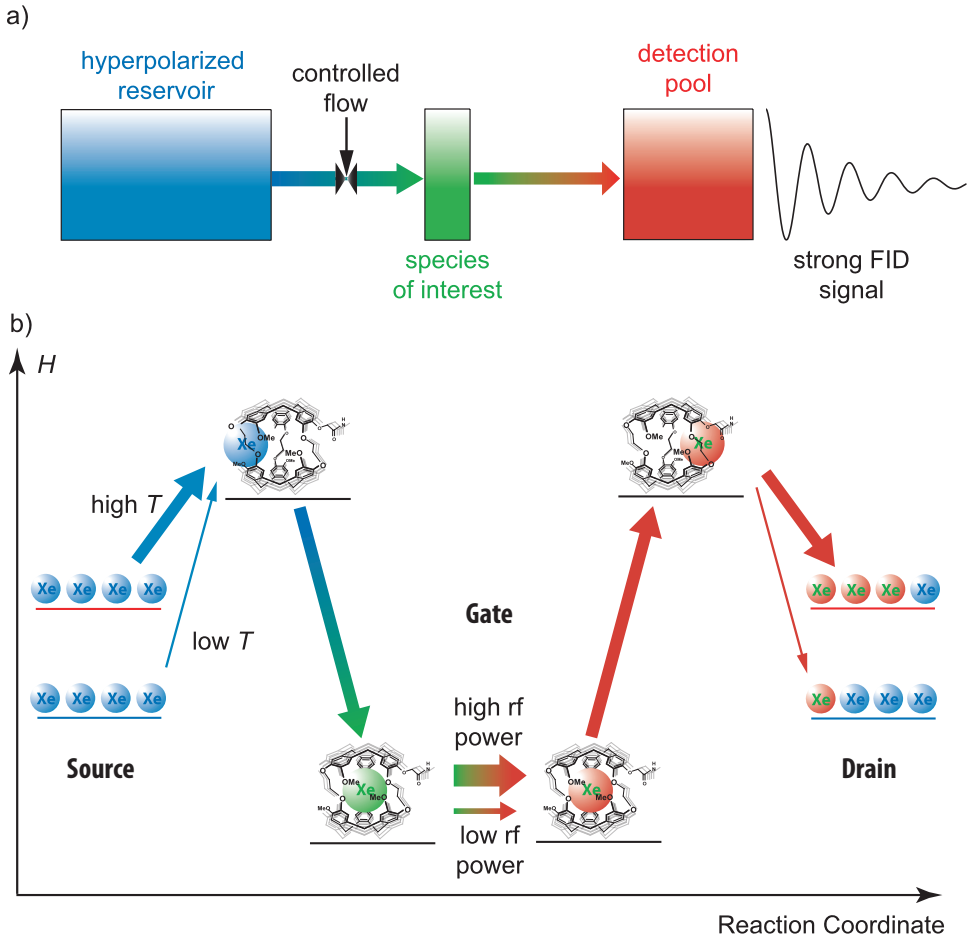

Figure 6.1: NMR signal enhancement through transfer of magnetization and its implementation for hp-^{129}Xe atoms (transpletor concept). a) Magnetization transfer using a hyperpolarized reservoir picks up information from a molecule of interest at low concentration. Controlling the flow from the reservoir allows gated transfer of the information into the detection pool. b) Flow diagram of hyperpolarized magnetization using a molecular host for controlled depolarization of ^{129}Xe guest atoms. Free hyperpolarized atoms (blue) represent the source of magnetization and can flow into the gate where they resonate at a different frequency (green) and can be saturated by a selective rf pulse. The depolarized nuclei (red) leave the cage and accumulate in the drain. Accessibility to the gate is determined by the activation barrier to enter the cage and can thus be controlled by temperature.

making more xenon susceptible to selective saturation. Third, as the solubility of xenon in water decreases with increasing temperature up to approximately 310 K, the resulting smaller reservoir pool is easier to saturate.

However, temperature changes will only be of advantage if the significantly reduced residence time of the xenon inside the host will not cause a dramatic loss in saturation efficiency. The biosensor together with a selective rf pulse is expected to act in a similar fashion to a transistor. Figure 6.1b illustrates the concept of such a transpletor that transfers magnetization depletion by adjusting the flow of saturated xenon. Initially, the pool of free atoms represents the source. Entering the host makes them sensitive to selective depolarization. The cage therefore represents the gate that must be passed to enter the pool of depolarized nuclei that corresponds to the drain. Changes of the flow into the drain contain combined information about changes in the exchange rate and the saturation efficiency. Ultimately, increasing the temperature should induce a stronger source-to-drain current.

This temperature-gated amplification was demonstrated by a set of signal depletion curves at different temperatures. These curves display the decrease in bulk xenon magnetization as a function of saturation time, t_{sat}. Here, we used a molecular sensor that tracks avidin via its biotin moiety in aqueous solution [113]. Figure 6.2a shows the significant acceleration in reaching the maximum Hyper-CEST effect for the transition from 290 to 310 K. Using the function $I_{norm}(t_{sat}) = I_0 \exp(-t_{sat}/\tau)$ to model the data, the depolarization flow is proportional to the inverse of the time constant, τ. Figure 6.2b demonstrates that τ^{-1} increases by more than ten-fold upon heating the sample by 20 K.

The above-mentioned problem of decreasing saturation efficiency is reflected by the observation that the increase of flow into the drain depends more on saturation power at higher temperatures. The shorter residence time causes homogenous line broadening which makes an rf pulse amplitude of $B_1 = 29.1\,\mu$T at 310 K almost two times more efficient than a pulse of $3.7\,\mu$T (Figure 6.2b). However, there is a temperature-gated amplification effect even for the low power pulse. This principle becomes relevant in two cases: First, the Hyper-CEST saturation power might be limited for SAR safety reasons in biomedical imaging. Second, application of low-bandwidth pulses is an important step for reading out different sensor signals in the same system [75, 77]. Both of these issues may be mitigated by implementing low-power, high-selectivity saturation pulses, such as those described in Chapter 4.

The transpletor concept was implemented with a biosensor imaging setup at 7.05 T using a pulse sequence with a saturation bandwidth of approximately 30 Hz ($B_1 = 1.6\,\mu$T). This should yield ineffective saturation at $T \approx 300$ K, but effective depletion transfer at slightly increased temperatures. ^{129}Xe MRI

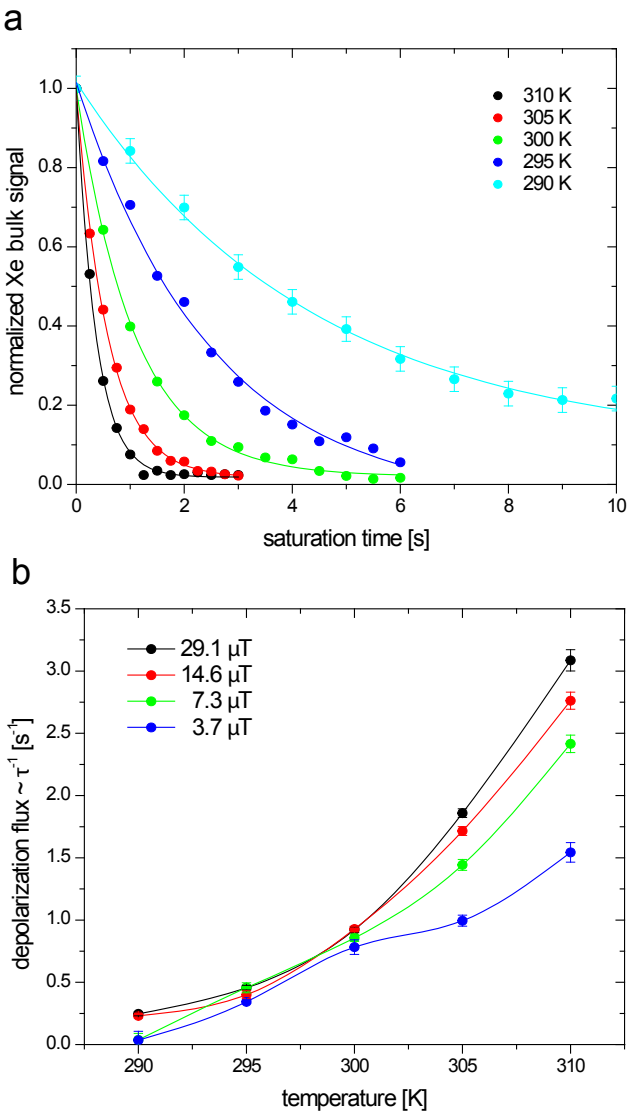

Figure 6.2: Source-to-drain depolarization flow control using Hyper-CEST with a cryptophane-A cage at different temperatures. a) Saturation curves for the normalized solution peak intensity, I_{norm}, of free dissolved ^{129}Xe in the presence of sensor with a concentration of 20 mm and saturation power $B_1 = 14.6\,\mu$T at different temperatures. The time constant τ varies between 4.34 s for 290 K and 0.36 s for 310 K. b) Plot of τ^{-1} from saturation curves as in (a) as a function of temperature. Insufficient saturation occurs at high temperatures, as seen from the differences in τ^{-1} for different saturation powers. The pulse with $B_1 = 3.7\,\mu$T has a bandwidth of $\Omega \approx 72$ Hz and is therefore only marginally wider than the resonance to be saturated at 310 K. Using the high power pulse ($B_1 = 29.1\,\mu$T) with $\Omega \approx 614$ Hz ensures complete saturation even at high temperatures and reflects highly efficient transfer of depleted magnetization owing to increased xenon flow.

datasets were collected using a setup described below. Figure 6.3a shows a coronal ^{1}H MR image of the system with two samples of agarose beads, one sample labeled with the biosensor. The Xe_{aq} signal at 193.6 ppm (aqueous solution with agarose) can be detected in a single-shot, slice-selective spectrum (Figure 6.3b), and allows selective display of the spatial distribution of the microscopic beads (Figure 6.3c). In contrast, substantial line broadening (Figure 6.3d) and low concentration make the biosensor signal at approximately 65 ppm undetectable without substantial signal averaging (Figure 6.3e).

Figure 6.4 illustrates the expected temperature-gated amplification for sensor detection. At room temperature (299 K), the Hyper-CEST depletion is ineffective, as demonstrated by the SNR in a spectrum from the sensor-labeled compartment: when comparing on resonance with off resonance saturation, the SNR changes only by 8% (within the noise level). Increasing the temperature by 3 K yields a 28% decrease in SNR. Further heating to 305 K results in a significant rise in flow through the gate and, consequently, a 46% signal depletion, clearly highlighting the sensor-free compartment.

These data illustrate that despite the reduced exposure time of nuclei to the cage environment, there is a significant increase in signal contrast for higher temperatures. Substantial line broadening of bead-associated sensor—the resonance is over 200 Hz wide [1]—is not an issue in this case since inhomogeneous broadening, caused by immobilization, does not impede efficient saturation. Detecting structures of micrometer size becomes feasible with this technique, whereas conventional NMR readout fails to acquire sufficient proton signal for localization of macromolecules.

In summary, we demonstrated temperature-controlled molecular gates for optimized use of hyperpolarized nuclei in liquid state NMR. Biosensor detection now includes features of MRI thermometry [114], which could be used to monitor hyperthermia in oncologic therapy [115]. (Work conducted by others in the Pines lab after this research was published indicates that xenon-based thermometry may have thermal resolution equal to or better than typical proton resonance frequency [PRF] imaging currently used clinically [109].) Moreover, the concept of an NMR transpletor illustrates increased sensitivity at body temperature. Moreover, this concept can be applied to other problems that rely on exchangeable NMR-detected guests to reveal properties of the host structure or indirect detection of competing guests [69, 71, 75, 116]. Such experiments would facilitate studies of the exchange dynamics of other nanostructure hosts such as alternative cages, carbon nanotubes, zeolites, etc. . . [117] In addition, both competing molecules (e.g. methanol or chloroform in solution) with comparable or higher binding constants and parameters that change the host accessibility of the hyperpolarized guest (e.g. solvation of xenon) will influence

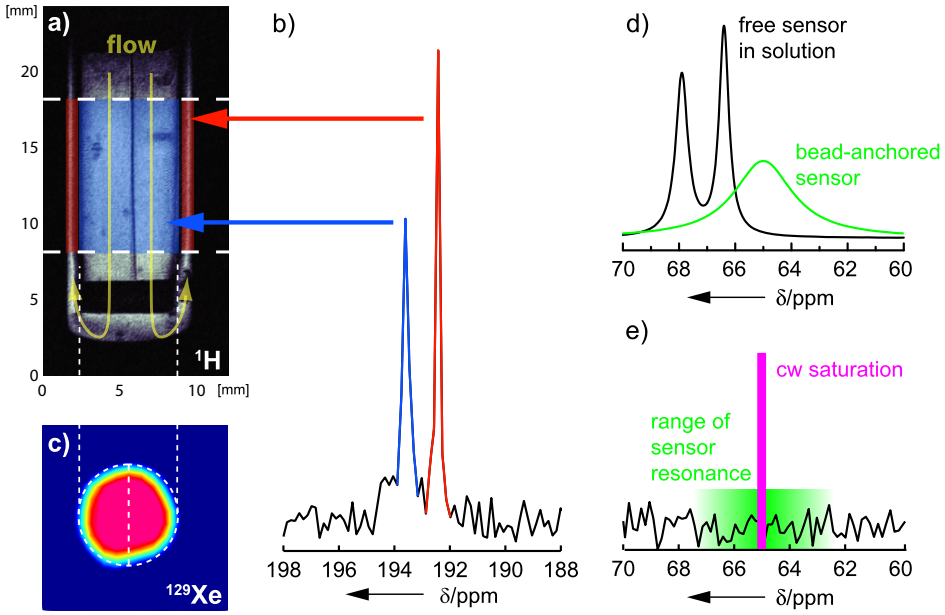

Figure 6.3: Conditions for ^{129}Xe MR imaging of functionalized cryptophane cages targeting microscopic beads. a) ^{1}H coronal image ($12 \times 24\,\mathrm{mm}^2$ field-of-view) of the perfusion phantom showing the 10 mm transverse slice for xenon imaging (colored overlays). The center volume with the agarose beads is split in two compartments, only one of which contains the functionalized cryptophane-A cage. The agarose-filled part of the slice (blue) is the source of a resonance at $\delta = 193.6$ ppm, and the surrounding part of the outlet gap (red) is the source of a peak at $\delta = 192.5$ ppm. b) Single-shot slice-selective ^{129}Xe-NMR spectrum showing the signals from the two colored regions in (a). c) Transverse ^{129}Xe image ($12 \times 12\,\mathrm{mm}^2$ field of view) generated from the peak at $\delta = 193.6$ ppm showing distribution of the agarose beads. d) Lineform changes of the biosensor signal upon immobilization to microscopic structures such as agarose beads. The schematic spectra with representative line widths are reported in [112] and [1]. e) The biosensor resonance of approximately 210 Hz linewidth at $\delta = 65$ ppm (green box) is below the noise threshold (high-field part of the spectrum in (b)). However, low-power saturation with $B_1 = 1.6\,\mu$T (corresponding to a saturation bandwidth of about 30 Hz; pink bar) will yield efficient saturation transfer at high temperature (see Figure 6.4).

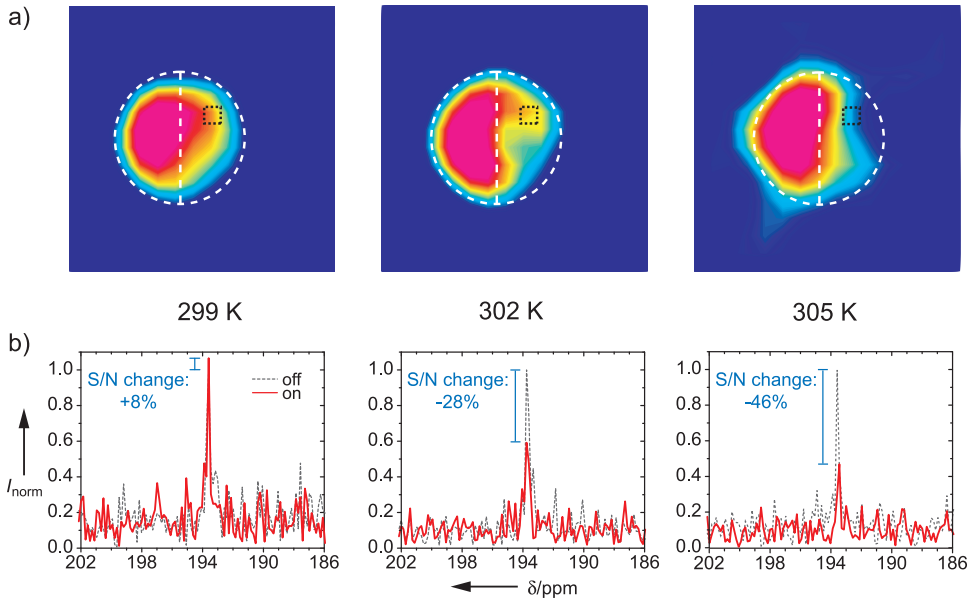

Figure 6.4: Application of the transpletor concept for temperature-sensitive molecular imaging. Compartments are indicated by white dotted lines. a) Transverse ^{129}Xe images show increasing contrast when the temperature is raised from 299 K to 305 K. The right compartment contains the biosensor with the functionalized cryptophane-A cage that responds only weakly to on resonance saturation with $B_1 = 1.6\,\mu$T for 1.5 s at 299 K. A higher temperature enhances the Hyper-CEST contrast and leads to significantly more efficient saturation. b) Corresponding spectra from the center of the right compartment (black dotted square) show the signal change for on resonance saturation (red spectra; compared to black data for off resonance saturation) at different temperatures. Whereas the SNR is almost unchanged at 299 K, a signal decrease of 46% can be achieved after increasing the sample temperature by 6 K.

the flow of hyperpolarized nuclei through the gate and could be detected with the transpletor. In this way, depolarization transfer enables sensitivity-enhanced detection of molecules even if they usually cannot directly benefit from hyperpolarization techniques.

Experimental Details

Datasets were recorded on a 7.05 T NMR spectrometer (Varian, Palo Alto, CA) with a 10 mm probe. Hyperpolarized xenon ($P \approx 4.6\%$) was generated with a XenoSpin polarizer (Amersham Health, Durham, NC) using a mixture of 89% He, 10% N_2 and 1% non-enriched xenon (Isotec, Sigma Aldrich). For evaluating the signal depletion upon increasing saturation time at different temperatures, this mixture was bubbled for 25 s at 0.45 SLM into an NMR tube containing roughly 2.5 mL of 20 μM biosensor solution. Gas flow was then interrupted using a stopped-flow system [99], followed by a 5 s delay to wait for disappearance of any bubbles. Next, the Hyper-CEST experiment started with a variable cw-saturation delay and subsequent readout of a single 300 ms free induction decay. The temperature of the system was controlled with the variable temperature unit of the spectrometer. After application of an apodization filter and Fourier transformation, the xenon solution peak at 192.5 ppm was integrated to determine signal depletion.

Imaging experiments were conducted with a gradient coil assembly (Resonance Research Inc., Billerica, MA) for spatial encoding. A two-compartment phantom, described elsewhere [1], contained avidin-labeled agarose beads (Immobilized Avidin, Pierce Biotechnology, Rockford, IL) and was perfused with water (6 mL min^{-1}) that was heated before entering the magnet with a two-foot-long heating cable (5 W ft^{-1} power output; BH Thermal® Corporation, Columbus, OH) and saturated with the polarizer gas mixture (0.65 SLM gas flow) immediately before entering the phantom [104]. One compartment contained the biosensor at 50 μM. A thermocouple attached to the outlet channel of the phantom was used to read the temperature of the water directly after leaving the bead volume. The maximum achievable temperature of the water was 305 K due to the need to keep the heating cable outside of the magnet and because of poor thermal conductance of the tubing guiding the water.

^{129}Xe Hyper-CEST images were acquired using a 1.5 s cw pulse of 1.6 μT amplitude and a slice-selective 90° pulse along the z-dimension (2 ms, SINC shape, 10 mm slice-thickness) with subsequent two-dimensional phase encoding (12×12 mm^2 field-of-view, matrix size 8×8, 10.8 min acquisition time). Each point in k-space was read out once for 64 ms with 100 kHz spectral width. Post-processing using MATLAB® (MathWorks, Inc., Natick, MA) included

two-dimensional FT for spatial reconstruction after zero-filling to a 16 × 16 dataset and one-dimensional FT for spectral reconstruction. Images showing the spatial distribution of the bead signal at 193.6 ppm were generated by summation of the signal intensity over five data points (approximately 0.74 ppm) in the absolute spectrum and subsequent color-encoding of these values.

Chapter 7

Temperature-enhanced Sensitivity[1]

"I shall attack Chemistry, like a Shark."
—Samuel Taylor Coleridge, letter to Sir Humphry Davy, 1800

As demonstrated in Chapter 6, chemical exchange rates are very sensitive to temperature; consequently, the response of the Hyper-CEST effect upon changes in temperature is a promising tool to achieve high-sensitivity detection of the *in situ* environment and of the concentration of caged ^{129}Xe. Xenon atoms have been shown to reside in cryptophane cages in water for a few milliseconds at room temperature [71]. An increase in temperature significantly decreases this lifetime [112] and should amplify the Hyper-CEST effect. Here, we describe the direct response of the xenon reservoir signal intensity, $I_{res}(t)$, in such a system to a temperature input function $T(t)$ in order to determine the sensitivity, dI_{res}/dT, of the ^{129}Xe NMR signal to temperature changes and to push the detection limit of functionalized cages into the nanomolar concentration range.

A gas mixture of 89% He, 10% N_2, and 1% xenon (natural abundance of ^{129}Xe: 26%) was passed through a hyperpolarizer (XenoSpin™, Amersham Health, Durham, NC) where spin exchange with optically pumped rubidium vapor [57] generates a ^{129}Xe nuclear spin polarization of approximately 5%. This mixture was delivered into an aqueous solution as described previously [99].

Figure 7.1 illustrates the ^{129}Xe NMR spectrum in D_2O of a cryptophane-A cage that has been functionalized by attaching the short peptide EEEEK

[1] This chapter is based on [95].

to the carboxylic acid "handle" present on the cryptophane;[2] this peptide provides solubility and an overall negative charge that mitigates electrostatic interactions with the glass wall of the NMR phantom that would otherwise prevent the cage construct from being detected at low concentrations. Data were recorded on a NMR spectrometer (Unity Inova, Varian Inc., Palo Alto, CA) at 7.05 T with a 10 mm ^{129}Xe NMR probe. The resonance of the dissolved, uncaged xenon at $\delta_1 = 193.8$ ppm can be detected with an SNR of 185 after 8 acquisitions at 295 K, whereas the diluted encapsulated xenon signal (33 μM cage concentration) at δ_2 =62.7 ppm gives only an SNR of 11.

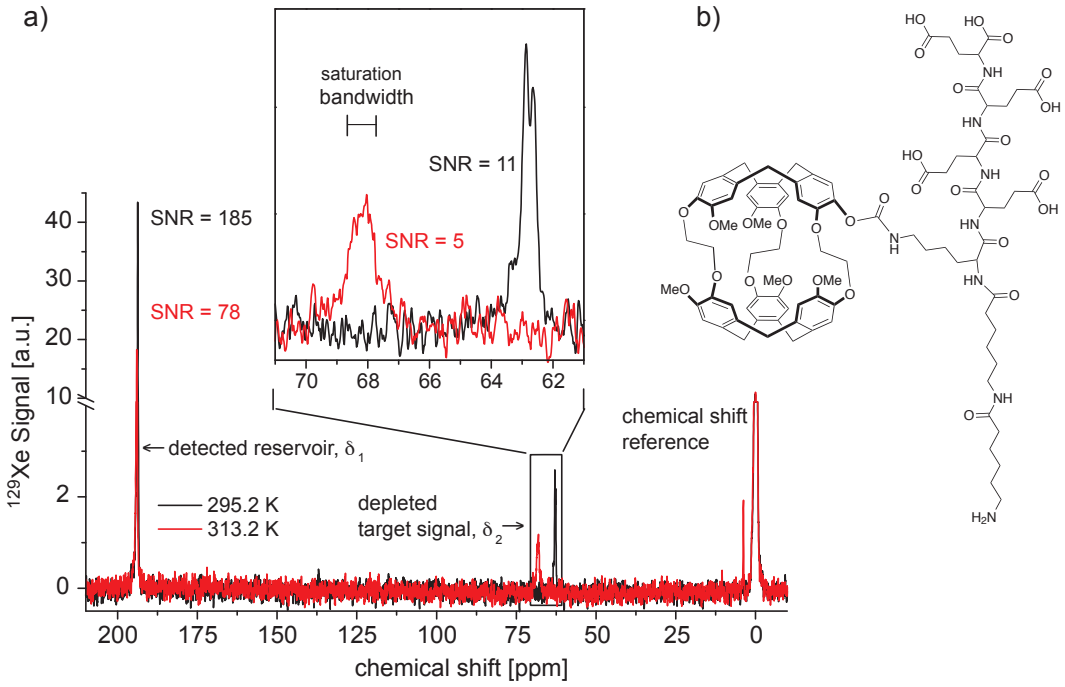

Figure 7.1: a) ^{129}Xe NMR spectrum illustrating that only a small fraction of xenon is associated with a functionalized cryptophane cage at 33 μM cage concentration. Increasing T from 295 K (black spectrum) to 313 K (red spectrum) shifts the signal of encapsulated xenon by approximately 5.5 ppm and induces accelerated chemical exchange that causes line broadening and decreases SNR. b) Chemical structure of the functionalized cryptophane molecule, EEEEK-cage, used in this study. The addition of the EEEEK peptide increases solubility of the cryptophane and confers an overall negative charge to the molecule, reducing interactions between the cage and the charged glass walls of the NMR phantom.

[2]The peptide was made using conventional solid-phase peptide synthesis (SPPS) protocols [118]. Attachment of the cryptophane cage to the peptide was done according to previously published procedures [81].

Table 7.1: Frequency offsets of line positions of the reservoir signal (ω_1) and caged xenon (ω_2) relative to the ^{129}Xe standard frequency of the spectrometer.

T [K]	ω_1 [Hz]	ω_2 [Hz]
295	14 972.0	4110.7
313	15 025.5	4590.0
$\Delta T = 18$ K	shift = 3.0 Hz K^{-1}	shift = 26.6 Hz K^{-1}

For this experiment, Hyper-CEST detection used a frequency-selective saturation pulse of 500 ms (amplitude $B_1 = 6.48\,\mu$T, bandwidth $\Omega = 0.93$ ppm) centered at δ_2, followed by observation of the subsequent change in the reservoir signal. Previous studies showed that the resonance frequency of the caged xenon shifts linearly with temperature [112]. This effect requires that the saturation carrier frequency, ω_{sat}, be swept to ensure optimum activation of the Hyper-CEST effect when studies extend over substantial temperature ranges and use narrow bandwidth saturation pulses. Comparing spectra at 295 and 313 K showed a shift of 26.6 Hz K^{-1} for the resonance of caged xenon (Table 7.1) for this molecule. In contrast, the reservoir signal shift of 3 Hz K^{-1} is insignificant and should not require parameter adjustments for this system.

The substantial exchange line broadening associated with increasing temperature causes a linewidth for trapped ^{129}Xe of roughly 74 Hz at 313 K compared to approximately 40 Hz at 295 K. Hence, thermometric resolution based on direct observation of encapsulated Xe is reduced from ~0.15 to 0.28 K at 313 K.[3] While direct observation of caged xenon requires relatively high concentrations of the construct (or extensive signal averaging), thermometry via saturation transfer into the reservoir works at much lower concentrations. However, sweeping ω_{sat} to scan for maximum saturation revealing $\delta_2(T)$ is time-consuming and, due to the above-mentioned line broadening, becomes less accurate with increasing temperature. Detecting $I_{res}(T)$ instead of $\delta_2(T)$ yields higher sensitivity to temperature changes and is achieved in only two acquisitions.

To illustrate this approach, the temperature of the biosensor sample was varied over time, serving as a characteristic input function $T(t)$, and the change in $I_{res}(T)$ was observed. To compensate for line shape changes at high temperatures, $I_{res}(T)$ was determined by integrating over a bandwidth of 70 Hz, centered at δ_1, to guarantee reproducible observation of the Hyper-CEST

[3] When SNR is not limiting, it is estimated that resonance shifts of approximately 10% of the linewidth can be detected; thus, 4 Hz is the resolution limit at 295 K, yielding a thermal resolution of roughly 0.15 K. Using mathematical fitting routines, such as those described in Chapter 5, may improve the accuracy of such shift measurements.

response. Starting at $T = 287\,\mathrm{K}$ and $\omega_{sat} = 3906.7\,\mathrm{Hz}$, the sample was heated up to $T = 313\,\mathrm{K}$ in steps of $2\,\mathrm{K}$ using the variable temperature unit of the spectrometer. To allow for stabilization of the temperature within the solution, an acquisition was started every seven minutes. Cooling of the sample to $287\,\mathrm{K}$ was performed at twice the rate that it had been heated, followed by an adjustment to room temperature [Figure 7.2a].

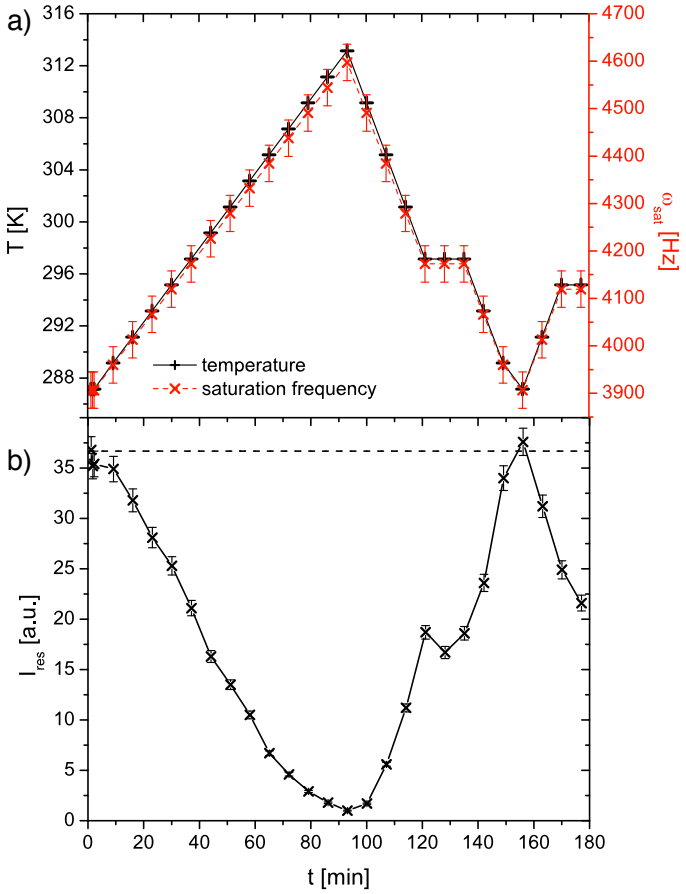

Figure 7.2: a) Input function $T(t)$ (black solid line) for Hyper-CEST signal transfer using the construct shown in Figure 7.1. The saturation frequency offset ω_{sat} (gray dashed line) is adjusted according to the resonance shift of $26.6\,\mathrm{Hz\ K^{-1}}$. Bars indicate the bandwidth of the saturation pulse of $\Omega = 76.7\,\mathrm{Hz}$ (0.925 ppm). b) Response $I_{res}(t)$ to $T(t)$. Varying the temperature changes ^{129}Xe signal transfer through the cage that is present at $27.2\,\mu\mathrm{M}$. The reference signal for no saturation transfer is illustrated by the dashed line.

Figure 7.2b shows the response of $I_{res}(T)$ to $T(t)$, quite clearly the inverse of the sawtooth input function, corresponding to increased depolarization transfer upon increasing temperatures and vice versa. To calibrate the temperature

sensitivity of this sensor, data from Figure 7.2b were used to plot I_{res} vs. T as shown in Figure 7.3a. Signal intensity from an acquisition without a saturation pulse [dashed line in Figure 7.2b] was used to normalize all data points. The temperature dependence can be modeled with an empirical fit to a sigmoidal Boltzmann function,

$$I_{res} = A_1 + \frac{A_2 - A_1}{1 + e^{(T-T_0)/dT}}; \tag{7.1}$$

with the parameters A_1= 0.04 ± 0.04, A_2 = 1.00 ± 0.05, T_0 = (297.5 ± 0.5) K, and dT = (3.9 ± 0.6) K^{-1}, the correlation coefficient R^2 was 0.98. The derivative of this sigmoidal Boltzmann function yields the differential temperature sensitivity, dI_{res}/dT, plotted in Figure 7.3b (solid line). This derivative function shows a maximum sensitivity of ∼6% decrease in signal intensity per kelvin at around 297.5 K. Since the systematic noise is about 3.6% (see below), this corresponds to temperature resolution of approximately 0.6 K.

The differential sensitivity is somewhat adjustable by adjusting certain system parameters. For example, lower cage concentrations, shorter saturation pulses, or lower saturation power would all yield less efficient saturation transfer at a given temperature, thus shifting the Boltzmann function to higher temperatures. This was demonstrated with a solution of 11.2 μM cage concentration (only one temperature sweep from 293 to 313 K in this case). As seen in Figure 7.3a, the overall saturation is decreased and the Boltzmann transition stretched over a wider temperature range (A_1= 0.11 ± 0.03, A_2 = 1.00 ± 0.03, T_0 = (303.7 ± 0.3) K, dT = (5.7 ± 0.5) K^{-1}, R^2 = 0.99). In addition, the range of maximum sensitivity is shifted by 6.2 K to give a high-temperature sensitivity [Figure 7.3b, dashed line]. Similarly, a low-temperature sensitivity could be achieved by opposite modifications.

The significant increase in saturation transfer upon increasing temperature shown in Figure 7.3a can be used to detect very low concentrations of caged xenon. To determine the detection threshold for this construct at body temperature (310 K), a solution of 10 nM EEEEK-CryA was prepared. Figure 7.4 illustrates that Hyper-CEST induces a signal decrease of ∼16% with this concentration after 20 s saturation with a pulse amplitude of B_1 = 25.8 μT (Ω = 544 Hz). The standard deviation of the signals detected in control experiments with off-resonance saturation was 3.6%.

To estimate the sensitivity gain compared to direct detection shown in Figure 7.1, parameters summarized in Table 7.2 were used. The xenon occupancy of the cages, calculated with a binding constant K = 6000 M^{-1} [99], is 53%. This information must be considered when designing cages with different affinity for the noble gas [75]. The saturation transfer observed in Figure 7.4 is caused by

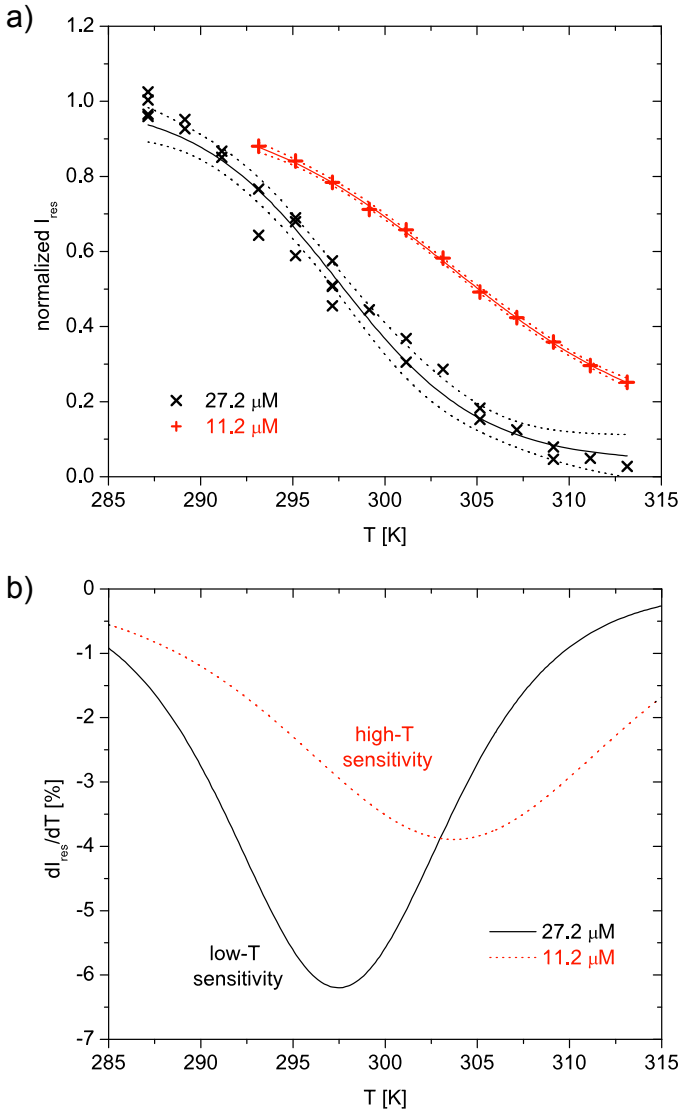

Figure 7.3: a) Calibration for temperature sensitivity of I_{res} shown in Figure 7.2b at 27.2 μM cage concentration ($\times$) and for 11.2 μM cage concentration ($+$). The signal intensity is normalized to a control experiment without saturation pulse. Data are fitted to Eq. 7.1 and shown with a 95% confidence band (dashed lines). b) The differential sensitivity of ^{129}Xe signal, intensity change per kelvin, is given by the first derivative of the fit results in (a). Reducing the concentration of the cage construct shifts the maximum sensitivity to higher temperatures. Since the experimental standard deviation in determining I_{res} is $\sim$3.6% (see below), the temperature resolution is limited to approximately 0.6 K for the 27.2 μM solution.

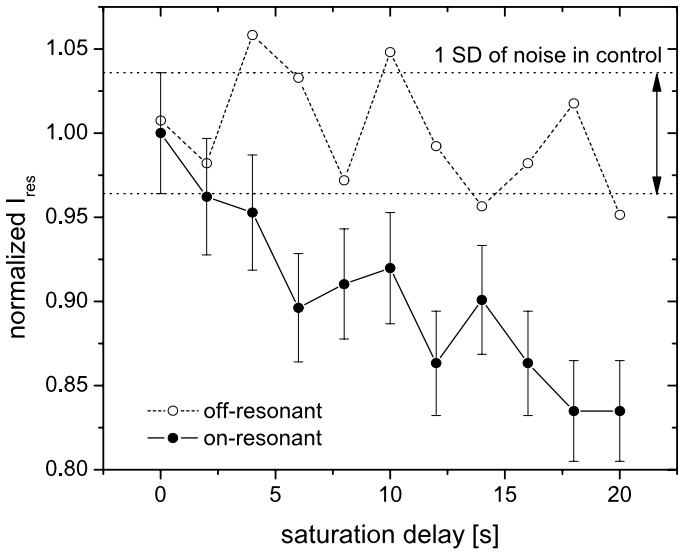

Figure 7.4: High-sensitivity detection of 1.4 nM encapsulated xenon signal (10 nM cage present) in D_2O at 310 K. The standard deviation in the control data set is 3.6% and is systematic noise due to imperfections in the xenon delivery. Maximum signal depletion is 16% of a resonance that was detected with a SNR of 110. However, the limiting factor for the Hyper-CEST detection is the variability of 3.6% in the off-resonance experiment, so SNR for indirect sensor detection is $16.5/3.6 = 4.6$.

Table 7.2: Experimental parameters for comparison of direct and indirect detection. The amount of detectable, encapsulated xenon, i.e., $[^{129}\mathrm{Xe}]_{\mathrm{cage}}$, is determined by the concentration of the cryptophane cage, the abundance of the isotope ^{129}Xe (26%), and the xenon partial pressure of the gas above the solution. The final acquisition time is determined by the number of scans and the repetition time TR.

	[cage] [nM]	max $[^{129}\mathrm{Xe}]_{\mathrm{cage}}$ [nM]	$[^{129}\mathrm{Xe}]_{\mathrm{cage}}$ at 58.4 mbar [nM]	No. of scans	TR [s]	SNR	T [K]
Direct detection	33 500	8710	4616	8	33	5.1	313.2
Hyper-CEST	10	2.6	1.38	2	53	4.6	310.2

a concentration of caged ^{129}Xe that is only 1.4 nM. Even though the SNR of direct detection at 310 K will be slightly higher than at 313 K, approximately 6 instead of 5.1,[4] this comparison still yields a sensitivity enhancement of roughly 4000 with respect to direct detection; the direct measurement time would be roughly 55 years to achieve the same SNR, rather than just under two minutes.

Under conditions described here the exchangeable, hp-^{129}Xe detection makes NMR much more sensitive than optical absorption methods in this specific case. Conventional, benchtop UV-visible absorbance detection of the cryptophane-A cage (ϵ_{287}= 8000 $\mathrm{M^{-1}\ cm^{-1}}$ [81]) requires a minimum concentration of $\sim$1 μM.[5] Thus the temperature-controlled depolarization transfer detection is very promising for new applications of high-sensitivity NMR with functionalized biosensors.

[4] Based on data in [112], the exchange rate increases by a factor of $\sim$14 as temperature increases from 22 °C to 40 °C, but only by $\sim$9 for as temperature increases from 22 °C to 37 °C; the corresponding line broadening would then reduce SNR from 11 to 6.

[5] Extinction coefficients can be as high as 100 000 $\mathrm{M^{-1}\ cm^{-1}}$ for many macromolecules, thus being approximately twelve times more sensitive than for cryptophane. However, this would still yield a minimum concentration of about 400 nM for detection with conventional UV-visible absorbance.

Chapter 8

Femtomolar Detection: MS2 Viral Capsids[1]

> "My mother made me a scientist without ever intending to. Every other Jewish mother in Brooklyn would ask her child after school, 'So? Did you learn anything today?' But not my mother. 'Izzy,' she would say, 'did you ask a good question today?' That difference—asking good questions—made me become a scientist."
> —Isidor Isaac Rabi, 1944

The refinement of targeted contrast agents is crucial for progress in molecular imaging. The primary contrast agents in use in magnetic resonance imaging (MRI) either modulate magnetic relaxation (e.g. gadolinium-based contrast agents [119]) or reduce bulk magnetization via exchange of saturated nuclei from a magnetically distinct site (e.g. CEST agents [120, 121]). While most contrast agents exploit strong proton signals from abundant water and fat, there are advantages to using exogenous nuclei. In particular, xenon is inert, relaxes slowly, can be reversibly dissolved in solution, and is amenable to hyperpolarization by optical pumping [38, 64, 102]. In this work, we present the development of an engineered nanoparticle that combines xenon-based molecular sensors with MS2 viral capsids, conferring dramatically increased solubility and CEST sensitivity to these contrast agents. Furthermore, previous reports have shown that MS2 viral capsids endowed with nucleotide aptamers [122] bind to specific cell receptors and are taken up by the cell, indicating probable biocompatibility. Because each capsid can be targeted to a molecule of interest, the incorporation of multiple sensor units into each individual capsid

[1] This chapter is based on [96].

could facilitate the detection of chemical targets at much lower concentrations than is possible using sensors without the capsid scaffold.

The MS2 viral capsid, composed of 180 monomers, is a porous, nearly spherical structure with icosahedral symmetry. After expression in *E. coli*, the coat protein monomers spontaneously assemble into genome-free, noninfectious capsids. The 32 pores in MS2, each ∼2 nm wide, facilitate access to the interior without disassembly of the capsid. The interior and exterior surfaces of the capsid can be independently modified, both to a high degree, enabling the simultaneous integration of many contrast agent molecules in the interior and cell-specific targeting units on the exterior [122–126].

The synthesis of an MS2 capsid scaffold for xenon MRI, shown in Figure 8.1, relies on attachment of a xenon-host molecule, cryptophane-A cage conjugated with acetate as a chemical handle (1), to the interior of an MS2 viral capsid. The technique used to attach hydrophobic cryptophane-A to the interior of MS2 has been previously used to attach taxol [127], another water-insoluble molecule. Attachment requires both a mutation (N87C) in MS2, introducing a solvent-accessible cysteine on the interior of the capsid, and a linker molecule (2). The linker contains a maleimide to react selectively with the interior cysteine, a taurine to increase the aqueous solubility of cryptophane-A, and an amine to react with cryptophane-A. (Synthetic protocols and characterization data are available in [96].) The purified cage-linker (3) was reacted with N87C MS2 for four hours at room temperature in 10 mM phosphate buffer at pH 7.2 to produce the MS2-cage construct, MS2CA. MS2CA was purified by size-exclusion chromatography, which also confirmed that the viral capsids were fully assembled; membrane-filter concentrated; and quantified using SDS-PAGE and optical densitometry. For analysis, ESI-MS was used to confirm that the cage had been attached to the viral capsid and to estimate the extent of modification—approximately 70% conversion was achieved, corresponding to ∼125 copies of cage per capsid.

The ^{129}Xe NMR spectrum of 1 μM cryptophane-A showed a clear peak from xenon dissolved in water (Xe_{aq}) at ∼190 ppm, consistent with previous observations [77]. However, no signal corresponding to xenon in cryptophane cage (Xe@cage) was observed directly. Consequently, we employed the Hyper-CEST detection method [1, 83]. By applying a selective-bandwidth saturation pulse and monitoring saturation transfer to the Xe_{aq} peak, we observed the presence of a Xe@cage peak at ∼60 ppm. Details of the frequency-selective saturation sequences and other experimental parameters used in these experiments are indicated in Table 8.1.

To compare the performance of the MS2CA sensor with that of unconjugated cage, we measured magnetization transfer in 7 nM MS2CA (assembled MS2CA

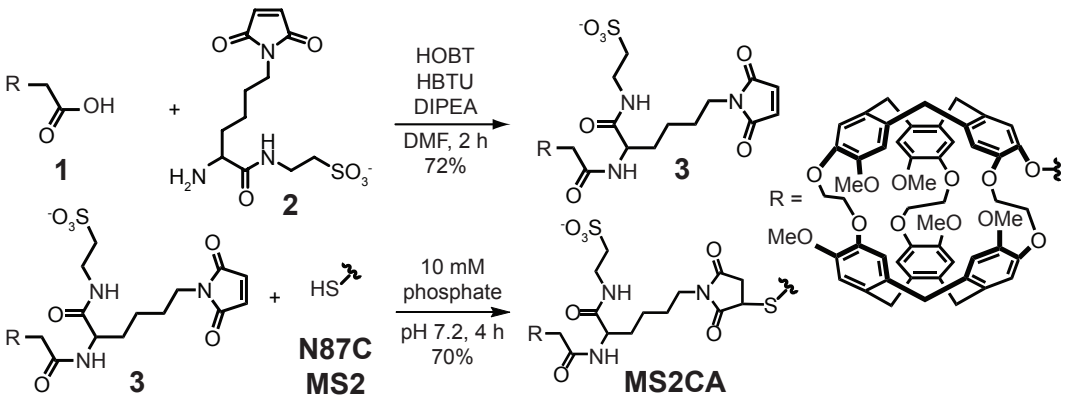

Figure 8.1: Synthesis of MS2CA.

units, corresponding to 1 μM coat protein monomers) and 1 μM cage solutions by incrementally varying the frequency of the applied saturation pulse. These spectra are shown in Figure 8.2. The contrast was comparable for both solutions. We note a downfield shift of the Xe@cage peak and a slight upfield shift of the Xe_{aq} peak in the MS2CA spectrum. Furthermore, we observe significant broadening of the Xe@cage saturation peak, from ∼1 kHz in the cage only system to ∼5 kHz in MS2CA. Achieving a strong Hyper-CEST effect in spite of line broadening of the Xe@cage in MS2CA is still possible by using saturation pulses with intentionally large bandwidths.

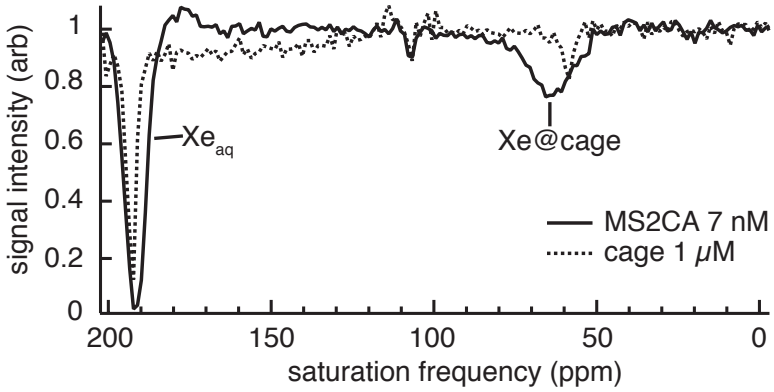

Figure 8.2: Saturation transfer spectra of the cage and MS2CA systems. The peaks at ∼190 ppm correspond to Xe_{aq}, while those at ∼60 ppm are Xe@cage. The feature at ∼110 ppm is anomalous.

To determine the detection threshold for MS2CA, we investigated dilutions of MS2CA to 700 pM, 70 pM, 7 pM, and 0.7 pM (assembled capsids), as well as

a control solution containing 10 mM phosphate buffer. For each sample, we collected saturation profiles by employing saturation pulses at the Xe@cage frequency for incremental saturation times. Three of these trials are summarized in Figure 8.3, with all trials represented individually in Figures 8.4–8.9, beginning on page 85. In addition, Table 8.1 indicates pulse parameters and calculated contrast for all concentrations of MS2CA studied. Magnetization transfer was apparent in all MS2CA cases; the 0.7 pM MS2CA represents the lowest concentration of detected xenon-based molecular sensors to date. The increased sensitivity over a measurement of 10 nM cryptophane-A reported by Schröder et al. [95], also presented in Chapter 7, is due both to the incorporation of ∼125 cages per MS2CA molecule and to various technical improvements,[2] including enhanced saturation transfer methods applicable to systems with broad NMR lines [87].

The incorporation of many xenon hosts into the MS2 viral capsid scaffold significantly lowers the detection threshold of binding targets and improves the solubility and potential biocompatibility of an otherwise hydrophobic host molecule. Although this is not the first application of a scaffold to produce an amplified molecular sensor [128], it has many more sensor molecules per targeting unit and demonstrates greater sensitivity than many previous multivalent scaffolds. While some multivalent gadolinium-based scaffolds produce greater contrast in ^{1}H MRI studies, there is growing concern over the *in vivo* toxicity of such contrast agents [129]. Additionally, other contrast mechanisms that rely on enzymes [130] or zeolites [131] show potential as sensitive molecular sensors. However, both of these methods rely on direct detection of xenon, requiring both high concentration and polarization of ^{129}Xe in the sample.

We are currently exploring the influence of solvent exposure on kinetics of both xenon exchange and saturation, properties that may be affected by the geometry of the MS2 capsid and that could improve saturation transfer-based detection techniques. In addition, one could further increase detection sensitivity of these molecular sensors by physical extraction of xenon through a phase change [119], by increasing the isotopic abundance of ^{129}Xe, or by increasing the xenon polarization [132]. We anticipate that a combination of these techniques will eventually permit detection of targets at femtomolar concentrations, finding application in portable analytical devices and greatly enhancing sensitivity for *in vivo* analytes.

[2] Refinements to the xenon delivery system plus an increase of the xenon gas concentration from 1% to 2% have reduced shot noise and increased signal considerably.

Table 8.1: Pulse parameters for detection of MS2CA. Both off resonance and on resonance saturation experiments were performed on each sample, all using d-SNOB pulses. In the table, Ω and B_1 refer to the bandwidth and peak power of of the applied pulse, respectively, duration is the length of each pulse, and delay is a waiting period between repeated pulses; a 0 ms delay indicates 100% duty cycle. The constants τ refer to exponential fits of the data, modeled by the function $f(t) = \exp(-t/\tau)$, with the error denoting the 90% confidence intervals. Using the fitted data, 20 s contrast indicates the contrast observed after saturation time $t = 20$ s under the indicated saturation conditions. The contrast of 8.9 ± 3.4% in the 0.7 pM MS2CA experiments reflects detection of the lowest concentration of contrast agent using NMR to date.

Figure	sample	T °C	Ω Hz	duration μs	delay ms	duty cycle %	B_1 kHz	$\tau_{\text{off-res}}$ s^{-1}	$\tau_{\text{on-res}}$ s^{-1}	20 s contrast
8.4	10 mM buffer	40	3000	940	0	100	3.962	36.432 ± 1.5055	36.852 ± 2.2294	-0.006 ± 0.040
8.5	700 pM MS2CA	37	5000	562.8	9.4482	5.62	6.280	28.241 ± 1.0158	14.161 ± 0.4649	0.505 ± 0.013
8.6	70 pM MS2CA	37	2500	1130	1.37	45.2	3.147	32.169 ± 1.3789	19.158 ± 0.714 65	0.344 ± 0.031
8.7	7 pM MS2CA	40	3000	940	0	100	3.962	31.615 ± 1.3571	23.346 ± 0.957 86	0.201 ± 0.036
8.8	0.7 pM MS2CA	40	5000	562.8	0	100	6.280	31.897 ± 1.1681	27.756 ± 1.1372	0.089 ± 0.034

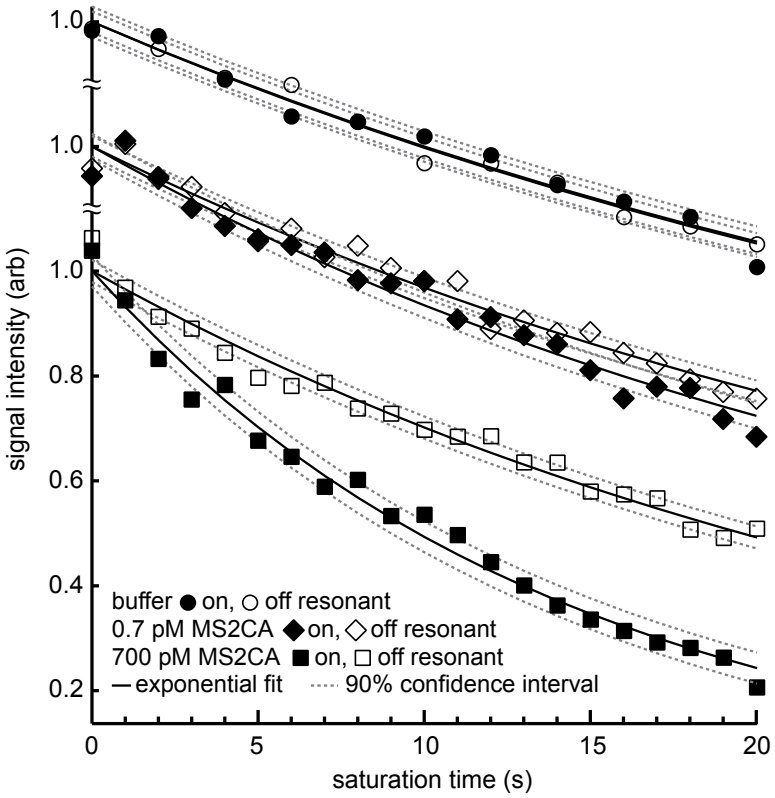

Figure 8.3: Saturation profiles of the buffer (top), 0.7 pM MS2CA (middle), and 700 pM MS2CA (bottom) solutions. After 20 s of saturation, contrast between the off and on resonance saturation experiments is evident in the MS2CA cases, indicating the presence of contrast agent. None of the experiments is corrected for relaxation, hence the decay in signal intensity in the off resonant saturation profiles. Exponential fits are given as solid lines. The three data sets are vertically offset for visibility.

Experimental Details

N87C MS2 was expressed and purified according to a previously published protocol [127]. To a solution of N87C MS2 (2 nmol, 6.7 μL, 300 μM) in 60 μL of 10 mM phosphate buffer at pH 7.2 was added the cage-linker construct (3) (50 nmol, 5.3 μL, 9.4 mM in DMF). The reaction mixture was incubated at room temperature for 4 h followed by purification by size exclusion chromatography. The amount of MS2 before and after purification was estimated using SDS-PAGE and optical densitometry analysis. The percent conversion was estimated using mass spectrometry analysis of similar samples. A control reaction was also run with wild type MS2, which lacked the N87C mutation, to test the reactivity of the native cysteine residues in the presence of (3).

No appreciable reaction product was observed when wild type MS2 was subjected to the conditions described above, demonstrating the low reactivity of the native cysteine residues. The purified MS2-cage conjugate (MS2CA) was spin-concentrated using Millipore Microcon®centrifugal filter devices with an Ultracel YM-100 membrane as specified and diluted into 0.9 mL 10 mM phosphate buffer at pH 7.2 to create solutions of approximately 1 μM capsid monomer (∼900 nM modified monomers, ∼7 nM assembled MS2 capsids).

For xenon NMR experiments, MS2CA was diluted to the specified concentration in 10 mM phosphate buffer at pH 7.2. The samples, each 0.9 mL, were loaded into a 5 mm NMR phantom that had been modified to allow introduction of hp-^{129}Xe, as previously described [99]. Each sample contained 50 μL of isopropyl alcohol to mitigate foaming as xenon was bubbled into the solution. Size exclusion chromatography was used to confirm that the MS2CA conjugate remains intact under these conditions. Data were recorded on a 7.05 T NMR spectrometer (Varian Inc., Palo Alto, CA) using a 5 mm probe. Hyperpolarized xenon ($P \approx 4\%$) was generated with a XenoSpin polarizer (Amersham Health, Durham, NC) from a gas mixture of 88% He, 10% N_2, and 2% natural-abundance xenon (26% ^{129}Xe; Airgas, Radnor, PA) at ∼70 psi. Gas containing hp-^{129}Xe was bubbled at a rate of 0.3 SLM for up to 20 s into the NMR tube. Gas flow was interrupted using a stopped-flow system, followed by a 4 s delay to allow the bubbles to dissipate. Frequency-selective saturation was applied using a series of d-SNOB pulses, with pulse duration and power calculated using the *pxshape* tool included in the VNMR software package (Varian Inc.). The applied pulse power was adjusted by up to ±1 dB to ensure that a single d-SNOB pulse generated spin inversion. Hyper-CEST [1] experiments were then conducted using saturation pulses (100 Hz bandwidth d-SNOB pulses, 28.2 ms each pulse, $B_1 = 6.65\,\mu$T, 10 s total saturation for indirectly detected saturation transfer spectra; parameters described in Table 8.1 for saturation profiles) and subsequent readout of a free induction decay (200 ms for saturation transfer spectra, 150 ms for saturation profiles). Data processing included application of an apodization filter and Fourier transformation (NMRPipe software) [100], and integration and normalization of the area under the peak corresponding to xenon dissolved in water (MATLAB®, The Math Works Inc., Natick, MA). Saturation profiles were fitted to exponential functions and error analysis was done using the *nlinfit* and *nlparci* functions of MATLAB®. The code detailing the exponential fitting routines is presented in Appendix D.

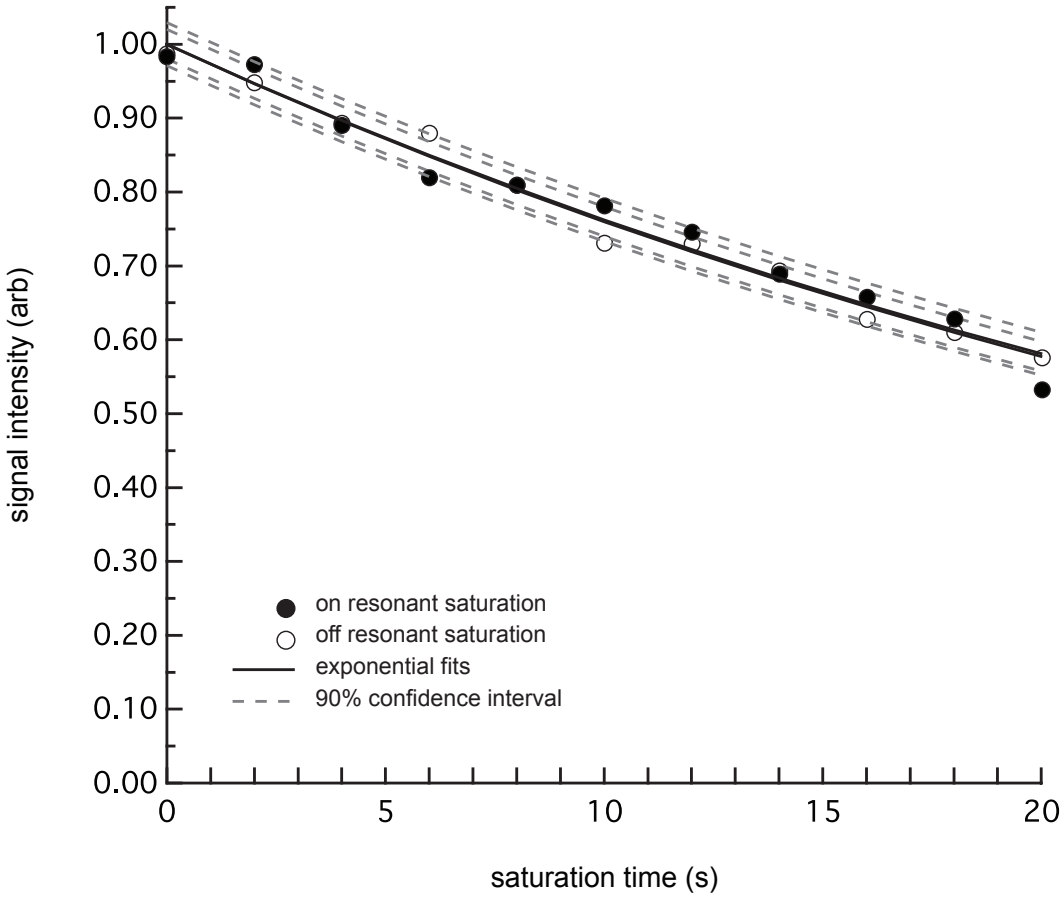

Figure 8.4: Saturation profiles of 10 mM phosphate buffer. Collected using d-SNOB saturation pulses centered at 4700 Hz (on resonant) and 25 763 Hz (off resonant).

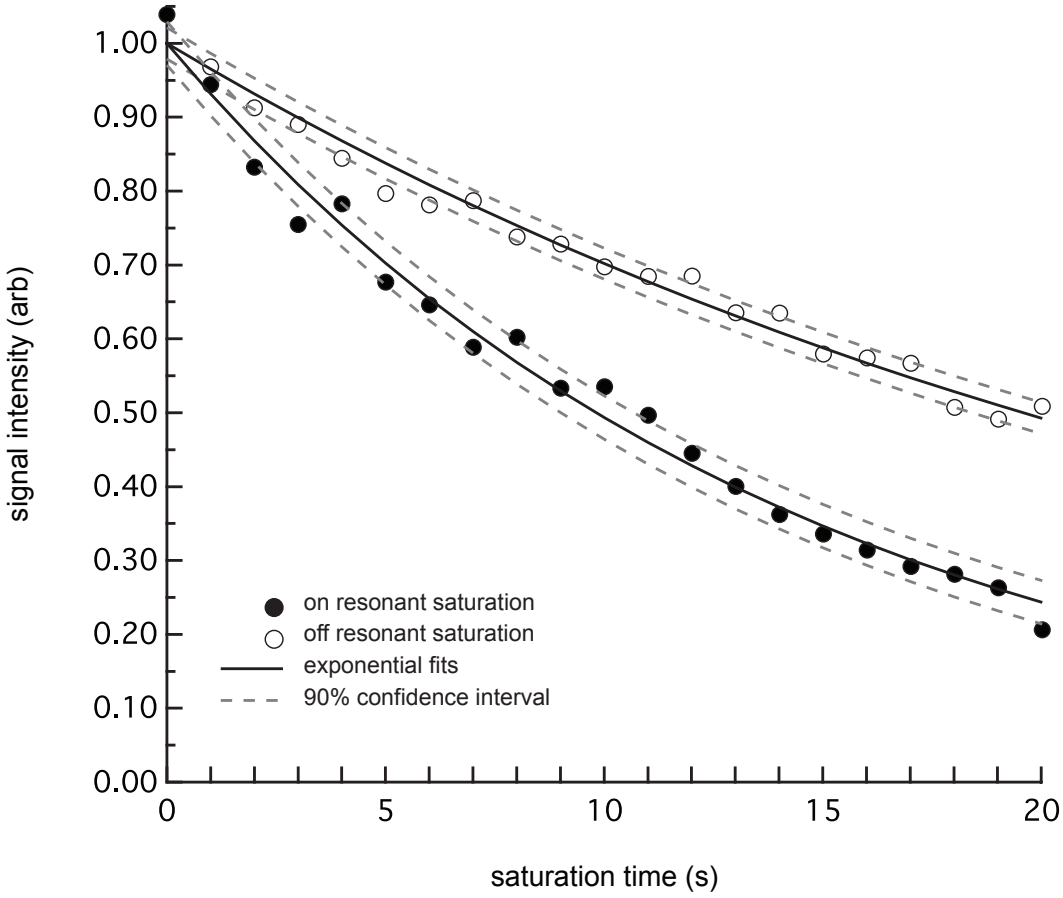

Figure 8.5: Saturation profiles of 700 pM MS2CA (assembled capsids, 125 nM coat protein monomers). Collected using d-SNOB saturation pulses centered at 4400 Hz (on resonant) and 25 502 Hz (off resonant).

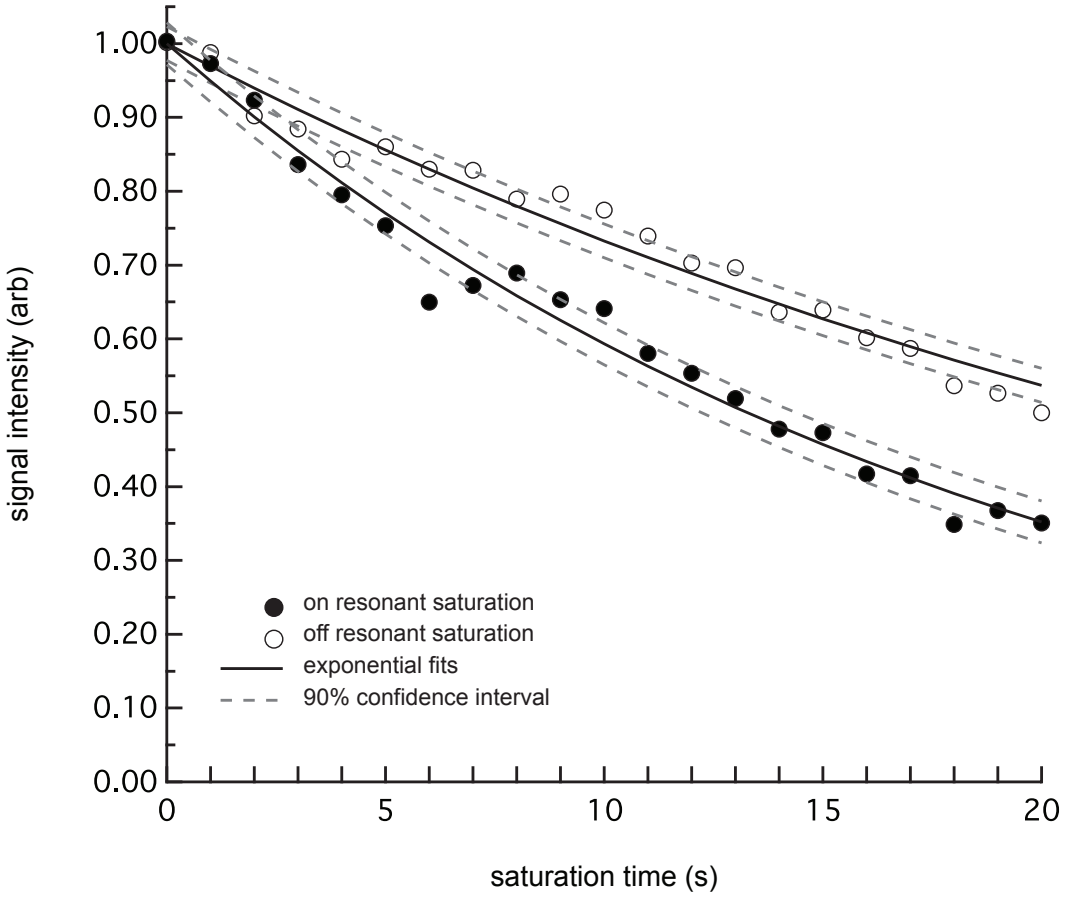

Figure 8.6: Saturation profiles of 70 pM MS2CA (assembled capsids, 12.5 nM coat protein monomers). Collected using d-SNOB saturation pulses centered at 4700 Hz (on resonant) and 25 763 Hz (off resonant).

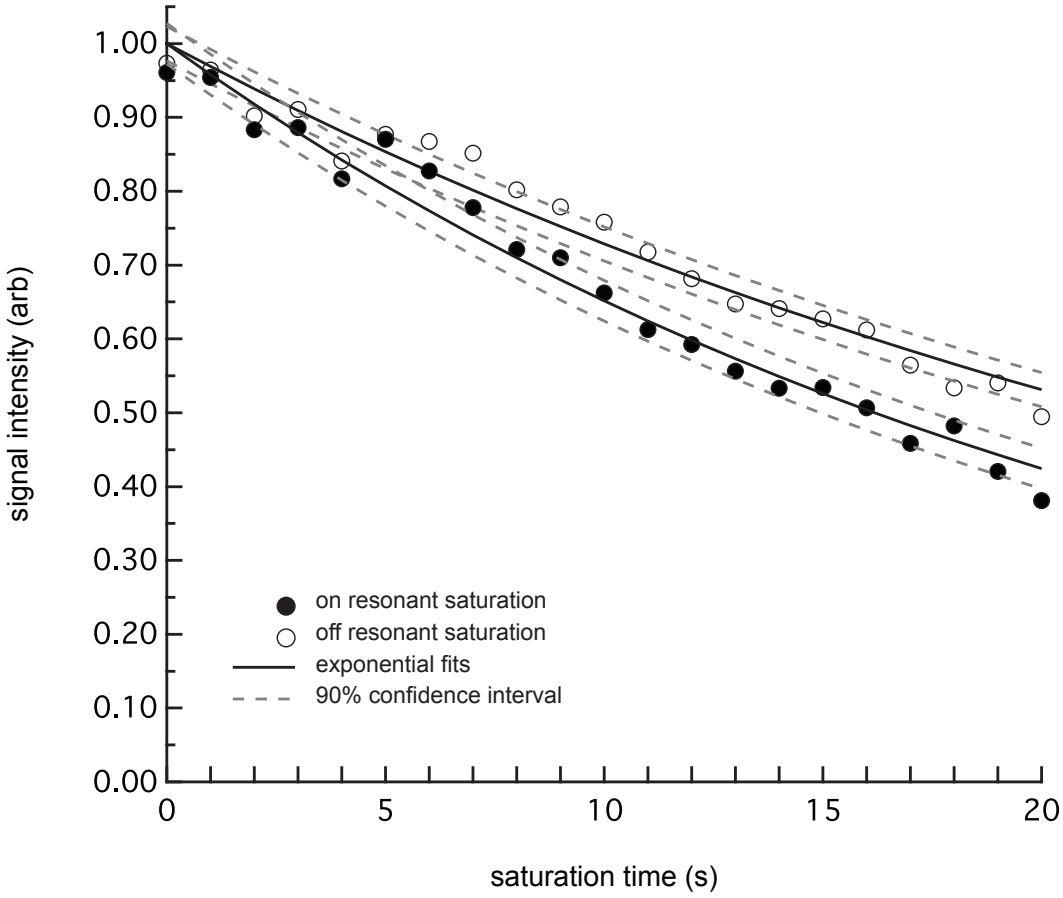

Figure 8.7: Saturation profiles of 7 pM MS2CA (assembled capsids, 1.25 nM coat protein monomers). Collected using d-SNOB saturation pulses centered at 4700 Hz (on resonant) and 25 763 Hz (off resonant).

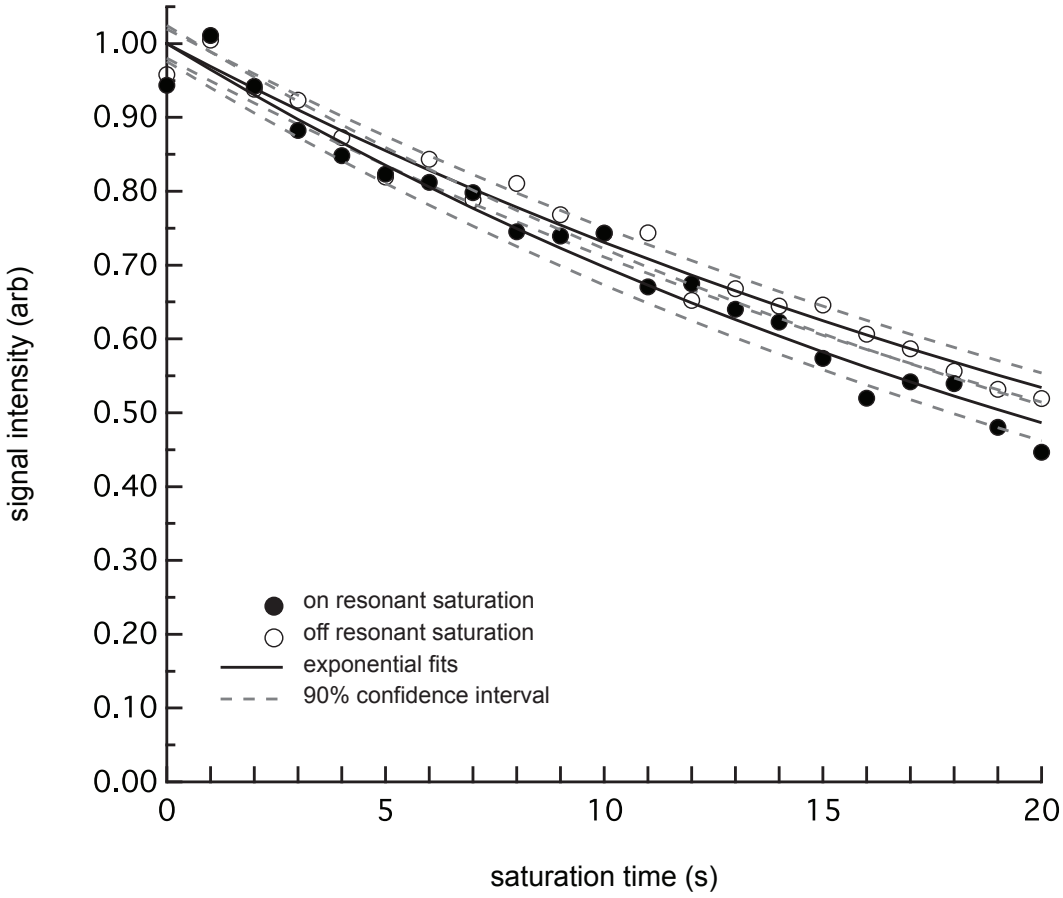

Figure 8.8: Saturation profiles of 0.7 pM MS2CA (assembled capsids, 125 pM coat protein monomers). Collected using d-SNOB saturation pulses centered at 4700 Hz (on resonant) and 25 763 Hz (off resonant).

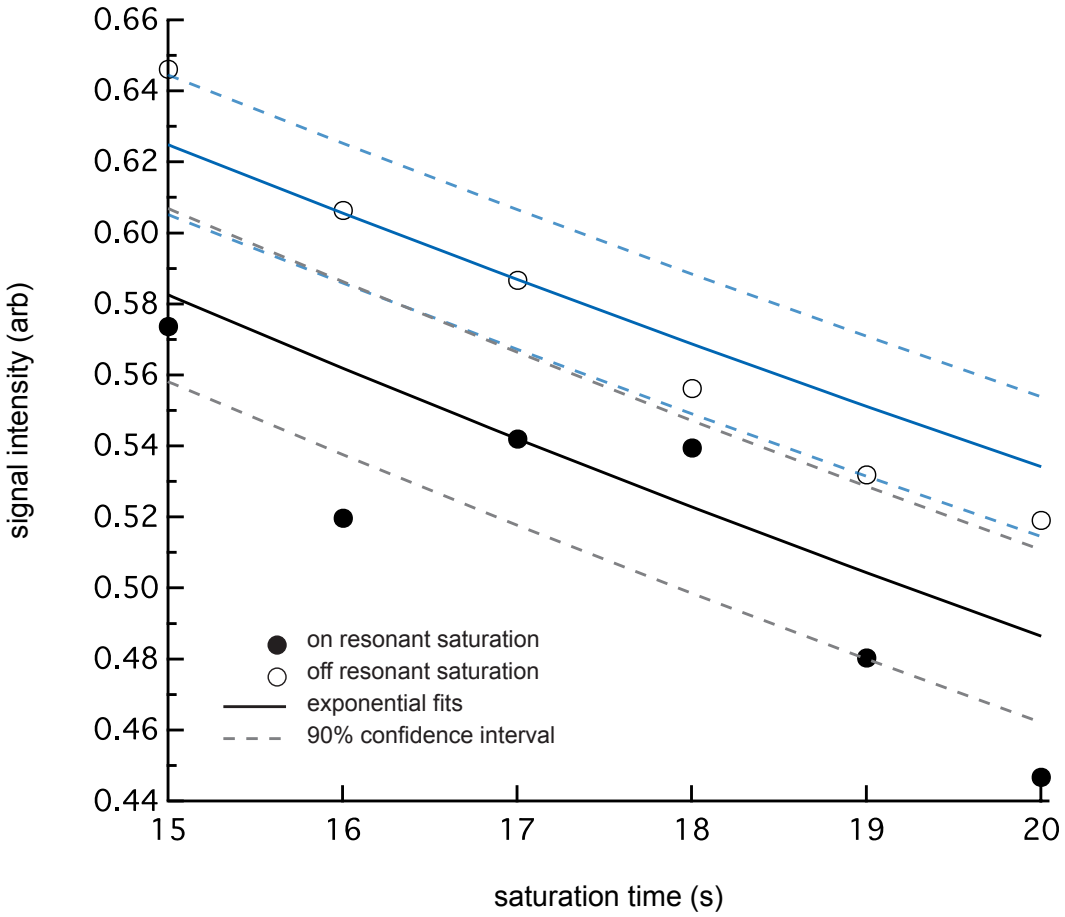

Figure 8.9: An inset of Figure 8.8, showing the contrast generated by 0.7 pM MS2CA.

Chapter 9

The Future of NMR-based Molecular Sensing

> "The most exciting phrase to hear in science, the one that heralds the most discoveries, is not 'Eureka!' but 'That's funny...' "
> —Isaac Asimov

Considering the techniques outlined in this dissertation so far, some clear advantages of xenon-based molecular sensors are apparent. In particular, the high spin-polarization of xenon nuclei leads to large contrast and consequent detection of analytes at low concentration, and the excellent sensitivity of the chemical shift of xenon to its environment, reporting on solvents, molecular hosts, and even temperature. Because of these properties, many resources are dedicated to investigating the application of xenon-based molecular sensors to *in vivo* molecular imaging. These efforts include SEOP apparatus capable of generating polarizations of up to 65% [48], agents for the delivery of hp-^{129}Xe that mitigate T_1 relaxation effects [106, 133, 134], and modifications to the cryptophane host that allow targeting to specific cellular receptors such as the epidermal growth factor receptor (EGFr).

While progress in *in vivo* molecular imaging using xenon-based molecular sensors would be a tremendous boon to medical physics, many *in vitro* analytical applications may benefit even more from xenon NMR. The same properties of chemical shift sensitivity and detection of dilute analytes are in effect and, since NMR does not require optically transparent samples, crude mixtures such as environmental samples, foodstuffs, and even municipal sewage could be analyzed using molecular sensors. In effect, coupling high-sensitivity molecular sensors to magnetic resonance analysis overcomes the sensitivity limitations of traditional

NMR while preserving the information-rich spectroscopic information and low-level sample preparation NMR affords.

Several advances in NMR methodology make such analytical applications of molecular sensors possible; namely miniaturization and remote detection. The primary goal for miniaturization is to make analysis by Xe-NMR widespread and affordable. Already, low-field NMR has found wide applications in spectroscopic [135–137] and relaxometric [138–140] analysis, as well as in imaging [141–144], all using magnets that are significantly less expensive and more portable than their traditional, superconducting counterparts. In addition, hyperpolarized gases have been imaged in both animal and human lungs at low fields [52]. Even the production of hyperpolarized gases is becoming miniaturized, with the laboratory of Dr. John Kitching at NIST (Boulder, Colorado) collaborating with the Pines group to produce microfluidic-scale xenon polarizers. The miniaturization of Xe-NMR will enable wide use of molecular sensors as analytical devices.

Remote detection, developed in the Pines lab over the past decade, has made possible the analysis of small quantities of spins in a flow path with high sensitivity. The fundamental mechanism underlying remote detection is the separation of the encoding and detection regions, and connecting those regions by some fluid flow. By separating the encoding and detection regions, each can be optimized for its particular geometry or other properties, thus enhancing the detected signal. Connecting these two regions via fluid flow allows one to acquire a time-of-flight dimension, making not only frequency (chemical shift) information available, but also information about velocity and acceleration, among others. More details on remote detection are available elsewhere [84]; it is sufficient to understand that remote detection allows one to analyze samples flowing in a microfluidic chip. This approach is highly compatible with the miniaturization of other aspects of xenon-based molecular sensing, and is crucial for applications in chemical analysis.

Combinatorial Analysis

The relatively long relaxation times involved in most NMR experiments lead to one of the most powerful aspects of NMR—multidimensional spectroscopy [6]. Because relaxation times are long, signals can be detected for a long time, allowing correlations between different spins to evolve, accumulate, and eventually be detected. Typical multi-dimensional experiments, such as COSY [145], explore correlations between spins in a given system; for example, the correlation between spins in a peptide. These experiments are routinely used to solve complicated problems such as the structures of proteins, but are

dependent on extremely high resolution, high signal measurements, usually performed in very strong magnetic fields.

An analog to the multidimensional spectroscopy described above is a statistical correlation between samples themselves. This pseudo-multidimensional spectroscopy, termed Statistical Total Correlation Spectroscopy (STOCSY) by Cloarec et al. [146], looks at correlations between large numbers of different samples to characterize sample properties. This approach, having obvious applications to metabolism, may also be applied to xenon-based molecular sensing. Because xenon-based sensors are sensitive to many parameters that characterize a sample—temperature, analyte size, hydrophobicity, and pH, to name a few—data from many samples could be analyzed to find features in Xe-NMR spectra that reflect particular chemical properties. In this case, it is perhaps advantageous that Xe-NMR is information-poor compared to its proton-based counterpart—more peaks may obscure correlations between spectra. These experiments may lead to a sort of chemical profiling of samples: no individual components are identified, but the composition of the sample as a whole is elucidated. Such analysis has strong implications for analysis of natural samples and waste streams in which many constituents comprise the samples.

A more evolved form of multidimensional spectroscopy associated with xenon-based molecular sensors relies on a combinatorial analysis of specific interactions between analytes in a sample and with the sensor itself. For example, a cryptophane cage attached to a metal-binding protein may experience a change in magnetic environment upon binding a metal, possibly due to either relaxation induced by the metal or a change in chemical shift caused by a conformational change in the peptide. Such a sensor could serve as a binary indicator of a sample, verifying the presence or absence of various analytes.[1] If a series of such sensors were placed in several channels of a microfluidic chip and the substance of interest flowed through the chip, one could quickly perform a binary assay for as many different constituents as there are channels in the chip. Each channel can be resolved either spectroscopically, if the frequency separation between the different sensor resonances is sufficient, or spatially using encoding gradients [85].

Such a combinatorial approach is amenable to recursive improvements by both a "forward" and "reverse" analysis. In the "forward" case, sensors designed *a priori* for binding with particular analytes are placed in a chip,

[1] It is conceivable that some quantitative results could be obtained using the same sensors, but dependence on Hyper-CEST based detection, which has a poorly understood quantitative response, is limiting.

then an analyte potentially containing those analytes is flowed through the chip and evaluated. In the "reverse" case, a library of sensors is generated, then a sample of a known analyte is flowed through the chip over the library of sensors. Those sensors that exhibit an MR response are then selected for that particular analyte. This process can be repeated until the sensors are refined for various physiochemical properties. In fact, the "reverse" process is under current study in the Pines lab: a twelve-amino acid peptide is conjugated to CryA and evaluated for presence of Rhodamine-6G, a fluorescent dye. So far, a change in chemical shift of approximately 0.5 ppm is observable.[2] With this as the first generation sensor, it seems highly probably that other sensors can be generated to produce even greater spectroscopic changes and, ultimately, a library of sensors for analytical applications.

[2] As these results are currently unpublished, please contact the author for more information at tyler.meldrum@gmail.com.

References

[1] Schröder L; Lowery T; Hilty C; Wemmer D; Pines A. Molecular imaging using a targeted magnetic resonance hyperpolarized biosensor. *Science* **2006**, *314*, 446–449.

[2] Blümich B. *Essential NMR for Scientists and Engineers*. Berlin: Springer, 1st ed. **2005**.

[3] Levitt MH. *Spin Dynamics: Basics of Nuclear Magnetic Resonance*. Chicester, England: Wiley, 2nd ed. **2008**.

[4] Nishimura DG. *Principles of Magnetic Resonance Imaging*. Palo Alto, California: Stanford University **2010**.

[5] Cavanagh J; Fairbrother WJ; Palmer AG; Skelton NJ; Rance M. *Protein NMR Spectroscopy: Principles and Practice*. Burlington, MA: Elsevier Academic Press, 2nd ed. **2006**.

[6] Ernst RR; Bodenhausen G; Wokaun A. *Principles of Nuclear Magnetic Resonance in One and Two Dimensions*. Oxford: Oxford University Press **1990**.

[7] Slichter CP. *Principles of Magnetic Resonance*. Berlin: Springer-Verlag, 2nd ed. **1989**.

[8] Abragam A. *Principles of Nuclear Magnetism*. Oxford: Oxford University Press **1961**.

[9] Ramsay W; Travers M. Argon and its companions. *Phil. Trans. R. Soc. Lond. A* **1901**, *197*, 47–89.

[10] Edgerton H; Cathou P. Xenon flash tube of small size. *Rev. Sci. Instrum.* **1956**, *27*, 821–825.

[11] Marx T; Schmidt M; Schirmer U; Reinelt H. Xenon anaesthesia. *J. R. Soc. Med.* **2000**, *93*, 513–517.

[12] Lawrence J; Loomis W; Tobias C; Turpin F. Preliminary observations on the narcotic effect of xenon with a review of values for solubilities of gases in water and oils. *J. Physiol.* **1946**, *105*, 197–204.

[13] Cullen SC; Gross EG. The anesthetic properties of xenon in animals and human beings, with additional observations on krypton. *Science* **1951**, *113*, 580–582.

[14] Bidabé A; de Beaufort D; Gin A; Caillé J. Measurement of cerebral blood flow by the stable xenon computerized tomography method. *J. Neuroradiol.* **1990**, *17*, 103–124.

[15] Lauterbur P. Image formation by induced local interactions: examples employing nuclear magnetic resonance. *Nature* **1973**, *242*, 190–191.

[16] Albert MS; Cates GD; Driehuys B; Happer W; Saam B; Springer CS; Wishnia A. Biological magnetic resonance imaging using laser-polarized ^{129}Xe. *Nature* **1994**, *370*, 199–201.

[17] Chupp T; Swanson S. Medical imaging with laser-polarized noble gases. *Adv. Atom. Mol. Opt. Phy.* **2001**, *45*, 41–98.

[18] Kouzes R. The ^{3}He supply problem. *PNNL-18388* **2009**.

[19] Lide DR (ed.). *CRC Handbook of Chemistry and Physics*. Boca Raton, Florida, USA: CRC Press, 77th ed. **1996**.

[20] Clever H (ed.). *Krypton, Xenon, and Radon—Gas Solubilities*, vol. 2. Oxford: Pergamon Press **1979**.

[21] Ladefoged J; Andersen A. Solubility of ^{133}Xe at 37 °C in water, saline, olive oil, liquid paraffin, solutions of albumin, and blood. *Phys. Med. Biol.* **1967**, *12*, 353–358.

[22] Möller H; Chawla M; Chen X; Driehuys B; Hedlund L; Wheeler C; Johnson G. Magnetic resonance angiography with hyperpolarized ^{129}Xe dissolved in a lipid emulsion. *Magn. Reson. Med.* **1999**, *41*, 1058–1064.

[23] Bifone A; Song Y; Seydoux R; Taylor R; Goodson B; Pietrass T; Budinger T; Navon G; Pines A. NMR of laser-polarized xenon in human blood. *Proc. Natl. Acad. Sci.* **1996**, *93*, 12932–12936.

[24] Abragam A; Goldman M. Principles of dynamic nuclear polarisation. *Rep. Prog. Phys.* **1978**, *41*, 395–467.

[25] Barnes A; Paëpe GD; van der Wel P; Hu K; Joo C; Bajaj V; Mak-Jurkauskas M; Sirigiri J; Herzfeld J; Temkin R; Griffin R. High-field dynamic nuclear polarization for solid and solution biological NMR. *Appl. Magn. Reson.* **2008**, *34*, 237–263.

[26] Maly T; Debelouchina G; Bajaj V; Hu K; Joo C; Mak-Jurkauskas M; Sirigiri J; van der Wel P; Herzfeld J; Temkin R; Griffin RG. Dynamic nuclear polarization at high magnetic fields. *J. Chem. Phys.* **2008**, *128*, 052211(19).

[27] Bowers C; Weitekamp D. Transformation of symmetrization order to nuclear-spin magnetization by chemical reaction and nuclear magnetic resonance. *Phys. Rev. Lett.* **1986**, *57*, 2645–2648.

[28] Bowers C; Weitekamp D. Parahydrogen and synthesis allow dramatically enhanced nuclear alignment. *J. Am. Chem. Soc.* **1987**, *109*, 5541–5542.

[29] Koptyug I; Kovtunov K; Burt S; Anwar M; Hilty C; Han S; Pines A; Sagdeev R. Para-hydrogen–induced polarization in heterogeneous hydrogenation reactions. *J. Am. Chem. Soc.* **2007**, *129*, 5580–5586.

[30] Adams R; Aguilar J; Atkinson K; Cowley M; Elliott P; Duckett S; Green G; Khazal I; Lopez-Serrano J; Williamson D. Reversible interactions with para-hydrogen enhance NMR sensitivity by polarization transfer. *Science* **2009**, *323*, 1708–1711.

[31] Atkinson K; Cowley M; Duckett S; Elliott P; Green G; López-Serrano J; Khazal I; Whitwood A. Para-hydrogen induced polarization without incorporation of para-hydrogen into the analyte. *Inorg. Chem.* **2009**, *48*, 663–670.

[32] Kastler A. Quelques suggestions concernant la production optique et la détection optique d'une inégalité de population des niveaux de quantifigation spatiale des atomes. Application à l'expérience de Stern

et Gerlach et à la résonance magnétique. *J. Phys. Radium* **1950**, *11*, 255–265.

[33] Happer W. Optical pumping. *Rev. Mod. Phys.* **1972**, *44*, 169–249.

[34] Walker T; Happer W. Spin-exchange optical pumping of noble-gas nuclei. *Rev. Mod. Phys.* **1997**, *69*, 629–642.

[35] Kastler A. Optical methods of atomic orientation and of magnetic resonance. *J. Opt. Soc. Am.* **1957**, *47*, 460–465.

[36] Happer W; Jau YY; Walker TG. *Optically Pumped Atoms*. Weinheim, Germany: Wiley-VCH Verlag GmbH & Co. KGaA **2010**.

[37] Appelt S; Baranga A; Erickson C; Romalis M; Young A; Happer W. Theory of spin-exchange optical pumping of ^{3}He and ^{129}Xe. *Phys. Rev. A* **1998**, *58*, 1412–1439.

[38] Goodson B. Nuclear magnetic resonance of laser-polarized noble gases in molecules, materials, and organisms. *J. Magn. Reson.* **2002**, *155*, 157–216.

[39] Wagshul M; Chupp T. Optical pumping of high-density Rb with a broadband dye laser and GaAlAs diode laser arrays: Application to ^{3}He polarization. *Phys. Rev. A* **1989**, *40*, 4447–4454.

[40] Bouchiat M; Carver T; Varnum C. Nuclear polarization in ^{3}He gas induced by optical pumping and dipolar exchange. *Phys. Rev. Lett.* **1960**, *5*, 373–375.

[41] Grover B. Noble gas NMR detection through noble gas-rubidium hyperfine contact interaction. *Phys. Rev. Lett.* **1978**, *40*, 391–392.

[42] Bhaskar N; Happer W; McClelland T. Efficiency of spin exchange between rubidium spins and ^{129}Xe nuclei in a gas. *Phys. Rev. Lett.* **1982**, *49*, 25–28.

[43] Happer W; Miron E; Schaefer S; Schreiber D; Wijngaarden WV; Zeng X. Polarization of the nuclear spins of noble-gas atoms by spin exchange with optically pumped alkali-metal atoms. *Phys. Rev. A* **1984**, *29*, 3092–3110.

[44] Knize R; Wu Z; Happer W. Optical pumping and spin exchange in gas cells. *Advances in atomic and molecular physics* **1988**, *24*, 223–267.

[45] Brunner E. Enhancement of surface and biological magnetic resonance using laser-polarized noble gases. *Concepts Magn. Reson.* **1999**, *11*, 313–335.

[46] Bouchiat M; Brossel J; Pottier L. Evidence for Rb–rare-gas molecules from the relaxation of polarized Rb atoms in a rare gas: Experimental results. *J. Chem. Phys.* **1972**, *56*, 3703–3714.

[47] Bouchiat C; Bouchiat M; Pottier L. Evidence for Rb–rare-gas molecules from the relaxation of polarized Rb atoms in a rare gas: Theory. *Phys. Rev.* **1969**, *181*, 144–165.

[48] Hersman F; Ruset I; Ketel S; Muradian I; Covrig S; Distelbrink J; Porter W; Watt D; Ketel J; Brackett J. Large production system for hyperpolarized ^{129}Xe for human lung imaging studies. *Acad. Radiol.* **2008**, *15*, 683–692.

[49] Cates G; Benton D; Gatzke M; Happer W; Hasson K; Newbury N. Laser production of large nuclear-spin polarization in frozen xenon. *Phys. Rev. Lett.* **1990**, *65*, 2591–2594.

[50] Gatzke M; Cates G; Driehuys B; Fox D; Happer W; Saam B. Extraordinarily slow nuclear spin relaxation in frozen laser-polarized ^{129}Xe. *Phys. Rev. Lett.* **1993**, *70*, 690–693.

[51] Ruppert K; Mata J; Brookeman J; Hagspiel K. Exploring lung function with hyperpolarized ^{129}Xe nuclear magnetic resonance. *Magn. Reson. Med.* **2004**.

[52] Venkatesh A; Zhang A; Mansour J; Kubatina L; Oh C; Blasche G; Ünlü MS; Balamore D; Jolesz F; Goldberg B. MRI of the lung gas-space at very low field using hyperpolarized noble gases. *Magn. Reson. Imaging* **2003**, *21*, 773–776.

[53] Albert M; Kacher D; Balamore D; Venkatesh A; Jolesz F. T_1 of ^{129}Xe in blood and the role of oxygenation. *J. Magn. Reson.* **1999**, *140*, 264–273.

[54] Wilson G; Santyr G; Anderson M; PM DeLuca J. T_2 of ^{129}Xe in rat tissue homogenates and blood at 9.4 T. *Proc. Intl. Soc. Mag. Reson. Med.* **1999**, *7*, 2102.

[55] Wolber J; Cherubini A; Santoro D; Payne G; Leach M; Bifone A. Linewidths of hyperpolarized ^{129}Xe NMR spectra in human blood at 1.5 T. *Proc. Intl. Soc. Mag. Reson. Med.* **2000**, *8*, 970.

[56] Blumgart HL; Weiss S. Studies on the velocity of blood flow. *J. Clin. Invest.* **1927**, *4*, 399–425.

[57] Goodson B. Using injectable carriers of laser-polarized noble gases for enhancing NMR and MRI. *Concepts Magn. Reson.* **1999**, *11*, 203–223.

[58] Pietraiss T; Gaede HC. Optically polarized ^{129}Xe in NMR spectroscopy. *Adv. Mater.* **1995**, *7*, 826–838.

[59] Lim Y; King, Jr A. NMR chemical shifts of ^{129}Xe dissolved in liquid *n*-alkanes and their mixtures. *J. Phys. Chem.* **1993**, *97*, 12173–12177.

[60] Miller K; Reo N; Uiterkamp ATMS; Stengle DP; Stengle TR; Williamson KL. Xenon NMR: Chemical shifts of a general anesthetic in common solvents, proteins, and membranes. *Proc. Natl. Acad. Sci.* **1981**, *78*, 4946–4949.

[61] Stengle TR; Reo NV; Williamson KL. Nuclear magnetic resonance solvent shifts of xenon: A test of the reaction field model. *J. Phys. Chem* **1981**, *85*, 3772–3775.

[62] Jameson A; Jameson C; Gutowsky H. Density dependence of ^{129}Xe chemical shifts in mixtures of xenon and other gases. *J. Chem. Phys.* **1970**, *53*, 2310–2321.

[63] Jameson C. An empirical chemical shielding function for interacting atoms from direct inversion of NMR data. *J. Chem. Phys.* **1975**, *63*, 5296.

[64] Berthault P; Huber G; Desvaux H. Biosensing using laser-polarized xenon NMR/MRI. *Prog. Nucl. Magn. Reson. Spectrosc.* **2009**, *55*, 35–60.

[65] Rubin S; Spence M; Dimitrov I; Ruiz EJ; Pines A; Wemmer DE. Detection of a conformational change in maltose binding protein by ^{129}Xe NMR spectroscopy. *J. Am. Chem. Soc.* **2001**, *123*, 8616–8617.

[66] Menger F; Takeshita M; Chow J. Hexapus, a new complexing agent for organic molecules. *J. Am. Chem. Soc.* **1981**, *103*, 5938–5939.

[67] Gabard J; Collet A. Synthesis of a (D_3)-bis(cyclotriveratrylenyl) macrocage by stereospecific replication of a (C_3)-subunit. *J. Chem. Soc. Chem. Comm.* **1981**, *1981*, 1137–1139.

[68] Garel L; Dutasta J; Collet A. Complexation of methane and chlorofluorocarbons by cryptophane-A in organic solution. *Angew. Chem. Int. Edit.* **1993**, *32*, 1169–1171.

[69] Garel L; Lozach B; Dutasta J; Collet A. Remarkable effect of the receptor size in the binding of acetylcholine and related ammonium ions to water-soluble cryptophanes. *J. Am. Chem. Soc.* **1993**, *115*, 11652–11653.

[70] Costante-Crassous J; Marrone T; Briggs J; McCammon J; Collet A. Absolute configuration of bromochlorofluoromethane from molecular dynamics simulation of its enantioselective complexation by cryptophane-C. *J. Am. Chem. Soc.* **1997**, *119*, 3818–3823.

[71] Bartik K; Luhmer M; Dutasta J; Collet A; Reisse J. ^{129}Xe and ^{1}H NMR study of the reversible trapping of xenon by cryptophane-A in organic solution. *J. Am. Chem. Soc.* **1998**, *120*, 784–791.

[72] Brotin T; Dutasta JP. Cryptophanes and their complexes—present and future. *Chem. Rev.* **2009**, *109*, 88–130.

[73] Fogarty H; Berthault P; Brotin T; Huber G; Desvaux H; Dutasta J. A cryptophane core optimized for xenon encapsulation. *J. Am. Chem. Soc.* **2007**, *129*, 10332–10333.

[74] Brotin T; Dutasta JP. Xe@cryptophane complexes with C_2 symmetry: Synthesis and investigations by ^{129}Xe NMR of the consequences of the size of the host cavity for xenon encapsulation. *Eur. J. Org. Chem.* **2003**, *2003*, 973–984.

[75] Huber G; Brotin T; Dubois L; Desvaux H; Dutasta J; Berthault P. Water soluble cryptophanes showing unprecedented affinity for xenon: candidates as NMR-based biosensors. *J. Am. Chem. Soc.* **2006**, *128*, 6239–6246.

[76] Meldrum T; Schröder L; Denger P; Wemmer D; Pines A. Xenon-based molecular sensors in lipid suspensions. *J. Magn. Reson.* **2010**, *205*, 242–246.

[77] Spence M; Rubin S; Dimitrov I; Ruiz E; Wemmer D; Pines A; Yao S; Tian F; Schultz P. Functionalized xenon as a biosensor. *Proc. Natl. Acad. Sci.* **2001**, *98*, 10654–10657.

[78] Huber G; Beguin L; Desvaux H; Brotin T; Fogarty H; Dutasta JP; Berthault P. Cryptophane-xenon complexes in organic solvents observed through NMR spectroscopy. *J. Phys. Chem. A* **2008**, *112*, 11363–11372.

[79] Ruiz EJ; Sears DN; Pines A; Jameson CJ. Diastereomeric Xe chemical shifts in tethered cryptophane cages. *J. Am. Chem. Soc.* **2006**, *128*, 16980–16988.

[80] Mecozzi S; Rebek, Jr J. The 55% solution: a formula for molecular recognition in the liquid state. *Chem. Eur. J.* **1998**, *4*, 1016–1022.

[81] Spence M; Ruiz E; Rubin S; Lowery T; Winssinger N; Schultz P; Wemmer D; Pines A. Development of a functionalized xenon biosensor. *J. Am. Chem. Soc.* **2004**, *126*, 15287–15294.

[82] Wolff S; Balaban R. Magnetization transfer contrast (MTC) and tissue water proton relaxation *in vivo*. *Magn. Reson. Med.* **1989**, *10*, 135–144.

[83] Ruppert K; Brookeman J; Hagspiel K; Mugler III J. Probing lung physiology with Xenon polarization Transfer Contrast (XTC). *Magn. Reson. Med.* **2000**, *44*, 349–357.

[84] Moulé A; Spence M; Han S; Seeley J; Pierce K; Saxena S; Pines A. Amplification of xenon NMR and MRI by remote detection. *Proc. Natl. Acad. Sci.* **2003**, *100*, 9122.

[85] Seeley J; Han S; Pines A. Remotely detected high-field MRI of porous samples. *J. Magn. Reson.* **2004**, *167*, 282–290.

[86] Grad J; Bryant R. Nuclear magnetic cross-relaxation spectroscopy. *J. Magn. Reson.* **1990**, *90*, 1–8.

[87] Bajaj VS; Meldrum T; Wemmer DE; Pines A. Band-selective chemical exchange saturation transfer imaging with hyperpolarized xenon-based molecular sensors. *Submitted* **2011**.

[88] Meyer C; Pauly J; Macovski A; Nishimura D. Simultaneous spatial and spectral selective excitation. *Magn. Reson. Med.* **1990**, *15*, 287–304.

[89] Tal A; Shapira B; Frydman L. Single-scan 2D Hadamard NMR spectroscopy. *Angew. Chem. Int. Ed.* **2009**, *121*, 2770–2774.

[90] Röschmann P. Radiofrequency penetration and absorption in the human body: Limitations to high-field whole-body nuclear magnetic resonance imaging. *Med. Phys.* **1987**, *14*, 922–931.

[91] Kupče E; Boyd J; Campbell I. Short selective pulses for biochemical applications. *J. Mag. Reson. Ser. B* **1995**, *106*, 300–303.

[92] Bauer C; Freeman R; Frenkiel T; Keeler J; Shaka A. Gaussian pulses. *J. Magn. Reson.* **1984**, *58*, 442–457.

[93] McCoy M; Mueller L. Selective decoupling. *J. Mag. Reson. A* **1993**, *101*, 122–130.

[94] Levitt M; Freeman R; Frenkiel T. Broadband heteronuclear decoupling. *J. Mag. Reson.* **1982**, *47*, 328–330.

[95] Schröder L; Meldrum T; Smith M; Lowery T; Wemmer D; Pines A. Temperature response of ^{129}Xe depolarization transfer and its application for ultrasensitive NMR detection. *Phys. Rev. Lett.* **2008**, *100*, 257603(4).

[96] Meldrum T; Seim K; Bajaj V; Palaniappan K; Wu W; Francis M; Wemmer D; Pines A. A xenon-based molecular sensor assembled on an MS2 viral capsid scaffold. *J. Am. Chem. Soc.* **2010**, *132*, 5936–5937.

[97] Pauly J; Roux PL; Nishimura D; Macovski A. Parameter relations for the Shinnar-Le Roux selective excitation pulse design algorithm. *IEEE T. Med. Imaging* **1991**, *10*, 53–65.

[98] Balchandani P; Pauly J; Spielman D. Designing adiabatic radio frequency pulses using the Shinnar-Le Roux algorithm. *Mag. Reson. Med.* **2010**, *64*, 843–851.

[99] Han SI; Garcia S; Lowery TJ; Ruiz EJ; Seeley JA; Chavez L; King DS; Wemmer DE; Pines A. NMR-based biosensing with optimized delivery of polarized ^{129}Xe to solutions. *Anal. Chem.* **2005**, *77*, 4008–4012.

[100] Delaglio F; Grzesiek S; Vuister G; Zhu G; Pfeifer J; Bax A. NMRPipe: A multidimensional spectral processing system based on UNIX pipes. *J. Biomol. NMR* **1995**, *6*, 277–293.

[101] Roy V; Brotin T; Dutasta J; Charles M; Delair T; Mallet F; Huber G; Desvaux H; Boulard Y; Berthault P. A cryptophane biosensor for the detection of specific nucleotide targets through xenon NMR spectroscopy. *ChemPhysChem* **2007**, *8*, 2082–2085.

[102] Seward GK; Wei Q; Dmochowski IJ. Peptide-mediated cellular uptake of cryptophane. *Bioconjugate Chem.* **2008**, *19*, 2129–2135.

[103] Aaron J; Chambers J; Jude K; Costanzo LD; Dmochowski I; Christianson D. Structure of a ^{129}Xe-cryptophane biosensor complexed with human carbonic anhydrase II. *J. Am. Chem. Soc.* **2008**, *130*, 6942–6943.

[104] Hilty C; Lowery TJ; Wemmer DE; Pines A. Spectrally resolved magnetic resonance imaging of a xenon biosensor. *Angew. Chem. Int. Edit.* **2006**, *45*, 70–73.

[105] Hill P; Wei Q; Eckenhoff R; Dmochowski I. Thermodynamics of xenon binding to cryptophane in water and human plasma. *J. Am. Chem. Soc.* **2007**, *129*, 9262–9263.

[106] Duhamel G; Choquet P; Grillon E; Lamalle L; Leviel J; Ziegler A; Constantinesco A. ^{129}Xe MR imaging and spectroscopy of rat brain using arterial delivery of hyperpolarized xenon in a lipid emulsion. *Magn. Reson. Med.* **2001**, *46*, 208–212.

[107] Smith R; Porter E; Miller K. The solubility of anesthetic gases in lipid bilayers. *Biochim. Biophys. Acta* **1981**, *645*, 327–338.

[108] Venkatesh A; Zhao L; Balamore D; Jolesz F; Albert M. Evaluation of carrier agents for hyperpolarized xenon MRI. *NMR Biomed.* **2000**, *13*, 245–252.

[109] Schilling F; Schröder L; Palaniappan K; Zapf S; Wemmer D; Pines A. MRI thermometry based on encapsulated hyperpolarized xenon. *ChemPhysChem* **2010**, *11*, 3529–3533.

[110] Cherubini A; Bifone A. Hyperpolarised xenon in biology. *Prog. Nucl. Magn. Reson. Spectrosc.* **2003**, *42*, 1–30.

[111] Schröder L; Chavez L; Meldrum T; Smith M; Lowery T; Wemmer D; Pines A. Temperature-controlled molecular depolarization gates in nuclear magnetic resonance. *Angew. Chem. Int. Edit.* **2008**, *47*, 4316–4320.

[112] Lowery T; Garcia S; Chavez L; Ruiz E; Wu T; Brotin T; Dutasta J; King D; Schultz P; Pines A. Optimization of xenon biosensors for detection of protein interactions. *ChemBioChem* **2006**, *7*, 65–73.

[113] Lowery T; Rubin S; Ruiz E; Spence M; Winssinger N; Schultz P; Pines A; Wemmer D. Applications of laser-polarized ^{129}Xe to biomolecular assays. *Magn. Reson. Imaging* **2003**, *21*, 1235–1239.

[114] Zhang S; Malloy C; Sherry A. MRI thermometry based on PARACEST agents. *J. Am. Chem. Soc.* **2005**, *127*, 17572–17573.

[115] Weidensteiner C; Quesson B; Caire-Gana B; Kerioui N; Rullier A; Trillaud H; Moonen C. Real-time MR temperature mapping of rabbit liver *in vivo* during thermal ablation. *Magn. Reson. Med.* **2003**, *50*, 322–330.

[116] Garcia C; Humilière D; Riva N; Collet A; Dutasta J. Kinetic and thermodynamic consequences of the substitution of SMe for OMe substituents of cryptophane hosts on the binding of neutral and cationic guests. *Org. Biomol. Chem.* **2003**, *1*, 2207–2216.

[117] Jameson C; Jameson A; Gerald II R; de Dios A. Nuclear magnetic resonance studies of xenon clusters in zeolite NaA. *J. Chem. Phys.* **1992**, *96*, 1676–1689.

[118] Merrifield R. Solid phase peptide synthesis. I. The synthesis of a tetrapeptide. *J. Am. Chem. Soc.* **1963**, *85*, 2149–2154.

[119] Zhou X; Graziani D; Pines A. Hyperpolarized xenon NMR and MRI signal amplification by gas extraction. *Proc. Natl. Acad. Sci.* **2009**, *106*, 16903–16906.

[120] Sherry A; Woods M. Chemical exchange saturation transfer contrast agents for magnetic resonance imaging. *Annu. Rev. Biomed. Eng.* **2008**, *10*, 391–411.

[121] Zhang S; Merritt M; Woessner D; Lenkinski RE; Sherry A. PARACEST agents: Modulating MRI contrast via water proton exchange. *Acc. Chem. Res* **2003**, *36*, 783–790.

[122] Tong G; Hsiao S; Carrico Z; Francis M. Viral capsid DNA aptamer conjugates as multivalent cell-targeting vehicles. *J. Am. Chem. Soc.* **2009**, *131*, 11174–11178.

[123] Allen M; Bulte J; Liepold L; Basu G; Zywicke H; Frank J; Young M; Douglas T. Paramagnetic viral nanoparticles as potential high-relaxivity magnetic resonance contrast agents. *Magn. Reson. Med.* **2005**, *54*, 807–812.

[124] Datta A; Hooker J; Botta M; Francis M; Aime S; Raymond K. High relaxivity gadolinium hydroxypyridonate—viral capsid conjugates: Nanosized MRI contrast agents. *J. Am. Chem. Soc.* **2008**, *130*, 2546–2552.

[125] Hooker J; Datta A; Botta M; Raymond K; Francis M. Magnetic resonance contrast agents from viral capsid shells: A comparison of exterior and interior cargo strategies. *Nano Lett.* **2007**, *7*, 2207–2210.

[126] Prasuhn, Jr D; Yeh R; Obenaus A; Manchester M; Finn M. Viral MRI contrast agents: coordination of Gd by native virions and attachment of Gd complexes by azide-alkyne cycloaddition. *Chem. Commun.* **2007**, pages 1269–1271.

[127] Wu W; Hsiao S; Carrico Z; Francis M. Genome-free viral capsids as multivalent carriers for taxol delivery. *Angew. Chem. Int. Edit.* **2009**, *48*, 9493–9497.

[128] Mynar J; Lowery T; Wemmer D; Pines A. Xenon biosensor amplification via dendrimer-cage supramolecular constructs. *J. Am. Chem. Soc.* **2006**, *128*, 6334–6335.

[129] Ersoy H; Rybicki F. Biochemical safety profiles of gadolinium-based extracellular contrast agents and nephrogenic systemic fibrosis. *J. Magn. Reson. Imaging* **2007**, *26*, 1190–1197.

[130] Wei Q; Seward G; Hill P; Patton B; Dimitrov I; Kuzma N; Dmochowski I. Designing ^{129}Xe NMR biosensors for matrix metalloproteinase detection. *J. Am. Chem. Soc.* **2006**, *9*, 13274–13283.

[131] Lerouge F; Melnyk O; Durand J; Raehm L; Berthault P; Huber G; Desvaux H; Constantinesco A; Choquet P; Detour J. Towards thrombosis-targeted zeolite nanoparticles for laser-polarized ^{129}Xe MRI. *J. Mater. Chem.* **2009**, *19*, 379–386.

[132] Schrank G; Ma Z; Schoeck A; Saam B. Characterization of a low-pressure high-capacity ^{129}Xe flow-through polarizer. *Phys. Rev. A* **2009**, *80*, 063424(10).

[133] Duhamel G; Choquet P; Grillon E; Leviel JL; Ziegler A; Constantinesco A. Rat brain perfusion measurements with hyperpolarized ^{129}Xe-NMR: study of biological fluids for the delivery of ^{129}Xe. *C. R. Acad. Sci. II C* **2001**.

[134] Duhamel G; Choquet P; Leviel J; Steibel J; Lamalle L; Julien C; Kober F; Grillon E; Derouard J; Décorps M; Ziegler Z; Constantinesco A. *In vivo* ^{129}Xe-NMR in rat brain during intra-arterial injection of hyperpolarized ^{129}Xe dissolved in a lipid emulsion. *C. R. Acad. Sci. III—Vie.* **2000**, *323*, 529–536.

[135] Danieli E; Mauler J; Perlo J; Blümich B; Casanova F. Mobile sensor for high resolution NMR spectroscopy and imaging. *J. Magn. Reson.* **2009**, *198*, 80–87.

[136] Appelt S; Häsing F; Kühn H; Perlo J; Blümich B. Mobile high resolution xenon nuclear magnetic resonance spectroscopy in the earth's magnetic field. *Phys. Rev. Lett.* **2005**, *94*, 197602(4).

[137] Perlo J; Demas V; Casanova F; Meriles C; Reimer J; Pines A; Blümich B. High-resolution NMR spectroscopy with a portable single-sided sensor. *Science* **2005**, *308*, 1279.

[138] Herrmann V; Unseld K; Fuchs H; Blümich B. Molecular dynamics of elastomers investigated by DMTA and the NMR-MOUSE. *Colloid Polym. Sci.* **2002**, *280*, 758–764.

[139] Blümich B; Anferova S; Sharma S; Segre A; Federici C. Degradation of historical paper: nondestructive analysis by the NMR-MOUSE. *J. Magn. Reson.* **2003**, *161*, 204–209.

[140] Blümich B; Casanova F; Buda A; Kremer K; Wegener T. Mobile NMR for analysis of polyethylene pipes. *Acta Phys. Pol. A* **2005**, *108*, 13–23.

[141] Dias M; Hadgraft J; Glover P; McDonald P. Stray field magnetic resonance imaging: a preliminary study of skin hydration. *J. Phys. D Appl. Phys.* **2003**, *36*, 364–368.

[142] Blümich B; Haber A; Casanova F; Federico E; Boardman V; Wahl G; Stilliano A; Isolani L. Noninvasive depth profiling of walls by portable nuclear magnetic resonance. *Anal. Bioanal. Chem.* **2010**, *397*, 3117–3125.

[143] Presciutti F; Perlo J; Casanova F; Glöggler S; Miliani C; Blümich B; Brunetti B; Sgamellotti A. Noninvasive nuclear magnetic resonance profiling of painting layers. *Appl. Phys. Lett.* **2008**, *93*, 033505(3).

[144] Perlo J; Casanova F; Blümich B. Profiles with microscopic resolution by single-sided NMR. *J. Magn. Reson.* **2005**, *176*, 64–70.

[145] Jeener J; Meier B; Bachmann P; Ernst R. Investigation of exchange processes by two-dimensional NMR spectroscopy. *J. Chem. Phys.* **1979**, *71*, 4546–4553.

[146] Cloarec O; Dumas M; Craig A; Barton R; Trygg J; Hudson J; Blancher C; Gauguier D; Lindon J; Holmes E; Nicholson J. Statistical total correlation spectroscopy: an exploratory approach for latent biomarker identification from metabolic ^{1}H NMR data sets. *Anal. Chem.* **2005**, *77*, 1282–1289.

Appendix A

Cryptophane Occupancy Calculations

For the chemical reaction

$$\mathrm{Xe} + \mathrm{cage} \rightleftharpoons \mathrm{Xe@cage},$$

thermodynamic equilibrium indicates that

$$K = \frac{[\mathrm{Xe@cage}]}{[\mathrm{Xe}]\,[\mathrm{cage}]}.$$

Knowing that free cage must be equal to the initial cage, $[\mathrm{cage}]_0$,

$$[\mathrm{cage}] = [\mathrm{cage}]_0 - [\mathrm{Xe@cage}]\,.$$

Likewise for xenon,

$$[\mathrm{Xe}] = [\mathrm{Xe}]_0 - [\mathrm{Xe@cage}]\,.$$

Algebraic manipulation results in the general solution for the occupancy of the cages:

$$\frac{[\mathrm{Xe@cage}]}{[\mathrm{cage}]_0} = \frac{1 + K\left([\mathrm{Xe}]_0 + [\mathrm{cage}]_0\right) \pm \sqrt{a}}{2K\,[\mathrm{cage}]_0},$$

where

$$a = 1 + 2K\left([\mathrm{Xe}]_0 + [\mathrm{cage}]_0\right) + K^2\left([\mathrm{Xe}]_0 - [\mathrm{cage}]_0\right)^2.$$

In many cases, the concentration of cryptophane cage is nearly equal to the concentration of xenon in solution, necessitating the use of the general solution. However, for the parameters mentioned above, the approximation that the amount of bound xenon is small relative to the total amount of xenon is valid,

and $[\mathrm{Xe}] = [\mathrm{Xe}]_0 - [\mathrm{Xe@cage}] \approx [\mathrm{Xe}]_0$. This assumption results in the much simpler formula

$$\frac{[\mathrm{Xe@cage}]}{[\mathrm{cage}]_0} = \frac{K[\mathrm{Xe}]_0}{1 + K[\mathrm{Xe}]_0}.$$

Using this simplification, the percent occupancy depends only on the binding constant K and the concentration of xenon in solution.

Assuming a binding constant of $6800\,\mathrm{M}^{-1}$, a xenon concentration of $367\,\mu\mathrm{M}$ (2% Xe at 60 psi), and a cryptophane concentration of $30\,\mu\mathrm{M}$, 70.2% of the cages are occupied as determined with the exact solution; the approximation slightly overestimates the occupancy at 71.4%.

Appendix B

Matlab code: Bloch simulations

MATLAB was used to simulate saturation pulses using cw, Gaussian, and d-SNOB shapes (see Chapter 4). Two scripts were generated, `powertesting.m`, which stores unique experimental parameters, and `blochsim.m`, which runs the actual simulation.

`powertesting.m`

```
% MASTER SIMULATION FILE for shaped pulses
% in an exchanging system.

% POWER REFERENCE —— this is for comparing rms powers
% of the pulses.

% cw = 0.5026 * dsnob
% cw = 0.3862 * gauss


clear
close all
clc



%% Initial parameters
%Pool 1 is Xe(aq) and Pool 2 is Xe@cage.

%Frequencies of the spin populations in Hz.
freq_1 = 15001.3;
freq_2 = 4050;

%Initial intensities of the signals.
Mz_1 = 0.999;
Mz_2 = 0.001;

%Relaxation times T1 and T2.
T1_1 = 14;
T1_2 = 14;
T2_1 = 0.125;
T2_2 = 0.0125;

```

```
%These files split up the shape of the pulses into pieces.
%CW is 1 piece,dsnob is in 200 pieces,
%and gauss is in 99 pieces.
load cw.mat;
load dsnob.mat;
load gauss.mat;

%These are the onres and offres saturation frequencies.
satfreq = [freq_2 ,freq_1 + (freq_1 - freq_2)];

%The list of residence times of "xenon in cage", given in s.
restimelist = [ 0.00005
                0.0001
                0.0005
                0.001
                0.005
                0.01
                0.02
                0.03
                0.04
                0.05
                0.06
                0.07
                0.08
                0.09
                0.10
                0.15
                0.20
                0.25
                0.30
                0.35
                0.40
                0.45
                0.50
                0.60
                0.70
                0.80
                0.90
                1.00];



%% CW
%This evaluates the Mz of the Xe(aq) peak following
%cw saturation at both the onres and offres frequencies.

pulsepat = cw;          %pulse pattern
b1max = (0:10:6000)';   %list of peak pulse powers in Hz
pulsetime = 1 ;         %pulse duration in s
satcycle = 1;           %number of saturation cycles

%These hold the final results of the simulation.
cwresult    = NaN(length(restimelist),1);
cwcontrast  = NaN(length(b1max),length(restimelist));
cwoffres    = NaN(length(b1max),length(restimelist));
cwonres     = NaN(length(b1max),length(restimelist));

%This loop is executed once for each residence time
%of Xe in cage, with the results stored in the four placeholder arrays at
%the end of the loop.
```

```
for i=1:1:length(restimelist)
    %tic                %can enable timing by uncommenting
                        %tic and toc below

    restime = restimelist(i);

    %blochsim is a function that performs the simulation. It is
    %explained separately.
    [simdata,contrast]  = blochsim(freq_1,freq_2,Mz_1,Mz_2,T1_1,T2_1,...
                            T1_2,T2_2,restime,pulsepat,pulsetime,b1max,...
                            satcycle,satfreq);

    %This identifies the maximum contrast generated in the simulation...
    [C,I] = max(contrast);
    %... and stores it in a vector with a point for each residence time.
    cwresult(i)     = 10*(I-1);

    %These hold the off-resonant, on-resonant, and contrast results from
    %the simulation.
    cwoffres(:,i)   = simdata(:,1,2);
    cwonres(:,i)    = simdata(:,1,1);
    cwcontrast(:,i) = contrast;

    %toc
end



%% dsnob 56.4 ms, one cycle
%This evaluates the Mz of the Xe(aq) peak following
%saturation with a single d-SNOB pulse of bandwidth 50 Hz
%(56.4 ms) at both the onres and offres frequencies.

pulsepat = dsnob;       %pulse pattern
b1max = (0:10:10000)';  %peak pulse power in Hz
pulsetime = 0.0564 ;    %pulse duration in s
satcycle = 1;           %number of saturation cycles

%These hold the final results of the simulation.
dsnob564oneresult   = NaN(length(restimelist),1);
dsnob564onecontrast = NaN(length(b1max),length(restimelist));
dsnob564oneoffres   = NaN(length(b1max),length(restimelist));
dsnob564oneonres    = NaN(length(b1max),length(restimelist));

%This loop is executed once for each residence time
%of Xe in cage, with the results stored in the four placeholder arrays at
%the end of the loop.
for i=1:1:length(restimelist)
    %tic                %can enable timing by uncommenting
                        %tic and toc below

    restime = restimelist(i);

    %blochsim is a function that performs the simulation. It is
    %explained separately.
    [simdata,contrast]  = blochsim(freq_1,freq_2,Mz_1,Mz_2,T1_1,T2_1,...
                            T1_2,T2_2,restime,pulsepat,pulsetime,b1max,...
                            satcycle,satfreq);

    %This identifies the maximum contrast generated in the simulation...
```

```
154      [C,I] = max(contrast);
155      %... and stores it in a vector with a point for each residence time.
156      dsnob564oneresult(i)     = (10*(I(satcycle)-1))';
157
158
159      %These hold the off-resonant, on-resonant, and contrast results from
160      %the simulation.
161      dsnob564oneoffres(:,i)   = simdata(:,satcycle,2);
162      dsnob564oneonres(:,i)    = simdata(:,satcycle,1);
163      dsnob564onecontrast(:,i) = contrast(:,satcycle);
164
165      %toc
166  end
167
168
169
170  %% dsnob 56.4 ms, one second
171  %This evaluates the Mz of the Xe(aq) peak following one second
172  %of saturation with d-SNOB pulse of bandwidth 50 Hz (56.4 ms)
173  %at both the onres and offres frequencies.
174
175  pulsepat = dsnob;        %pulse pattern
176  b1max = (0:50:10000)';   %peak pulse power in Hz
177  pulsetime = 0.0564 ;     %pulse duration in s
178  satcycle = 18;           %number of saturation cycles
179
180  %These hold the final results of the simulation.
181  dsnob564onesecresult    = NaN(length(restimelist),1);
182  dsnob564oneseccontrast  = NaN(length(b1max),length(restimelist));
183  dsnob564onesecoffres    = NaN(length(b1max),length(restimelist));
184  dsnob564oneseconres     = NaN(length(b1max),length(restimelist));
185
186  %This loop is executed once for each residence time
187  %of Xe in cage, with the results stored in the four placeholder arrays at
188  %the end of the loop.
189  for i=1:1:length(restimelist)
190      %tic                 %can enable timing by uncommenting
191                           %tic and toc below
192
193      restime = restimelist(i);
194
195      %blochsim is a function that performs the simulation. It is
196      %explained separately.
197      [simdata,contrast]  = blochsim(freq_1,freq_2,Mz_1,Mz_2,T1_1,T2_1,...
198                                T1_2,T2_2,restime,pulsepat,pulsetime,b1max,...
199                                satcycle,satfreq);
200
201      %This identifies the maximum contrast generated in the simulation...
202      [C,I] = max(contrast);
203      %... and stores it in a vector with a point for each residence time.
204      dsnob564onesecresult(i)     = (50*(I(satcycle)-1))';
205
206      %These hold the off-resonant, on-resonant, and contrast results from
207      %the simulation.
208      dsnob564onesecoffres(:,i)   = simdata(:,satcycle,2);
209      dsnob564oneseconres(:,i)    = simdata(:,satcycle,1);
210      dsnob564oneseccontrast(:,i) = contrast(:,satcycle);
211
212      %toc
213  end
```

```
214
215
216
217 %% dsnob 14.1 ms, one cycle
218 %This evaluates the Mz of the Xe(aq) peak following
219 %saturation with a single d-SNOB pulse of bandwidth 200 Hz
220 %(14.1 ms) at both the onres and offres frequencies.
221
222 pulsepat = dsnob;       %pulse pattern
223 b1max = (0:10:10000)'; %peak pulse power in Hz
224 pulsetime = 0.0141 ;    %pulse duration in s
225 satcycle = 1;           %number of saturation cycles
226
227 %These hold the final results of the simulation.
228 dsnob141oneresult   = NaN(length(restimelist),1);
229 dsnob141onecontrast = NaN(length(b1max),length(restimelist));
230 dsnob141oneoffres   = NaN(length(b1max),length(restimelist));
231 dsnob141oneonres    = NaN(length(b1max),length(restimelist));
232
233 %This loop is executed once for each residence time
234 %of Xe in cage, with the results stored in the four placeholder arrays at
235 %the end of the loop.
236 for i=1:1:length(restimelist)
237     %tic                %can enable timing by uncommenting
238                         %tic and toc below
239
240     restime = restimelist(i);
241
242     %blochsim is a function that performs the simulation. It is
243     %explained separately.
244     [simdata,contrast]  = blochsim(freq_1,freq_2,Mz_1,Mz_2,T1_1,T2_1,...
245                             T1_2,T2_2,restime,pulsepat,pulsetime,b1max,...
246                             satcycle,satfreq);
247
248
249     %This identifies the maximum contrast generated in the simulation...
250     [C,I] = max(contrast);
251     %... and stores it in a vector with a point for each residence time.
252     dsnob141oneresult(i)     = (10*(I(satcycle)-1))';
253
254     %These hold the off-resonant, on-resonant, and contrast results from
255     %the simulation.
256     dsnob141oneoffres(:,i)    = simdata(:,satcycle,2);
257     dsnob141oneonres(:,i)     = simdata(:,satcycle,1);
258     dsnob141onecontrast(:,i) = contrast(:,satcycle);
259
260     %toc
261 end
262
263
264
265 %% dsnob 14.1 ms, one second
266 %This evaluates the Mz of the Xe(aq) peak following one second
267 %of saturation with d-SNOB pulse of bandwidth 200 Hz (14.1 ms)
268 %at both the onres and offres frequencies.
269
270 pulsepat = dsnob;       %pulse pattern
271 b1max = (0:50:10000)'; %peak pulse power in Hz
272 pulsetime = 0.0564 ;    %pulse duration in s
273 satcycle = 71;          %number of saturation cycles
```

```
274
275 %These hold the final results of the simulation.
276 dsnob141onesecresult    = NaN(length(restimelist),1);
277 dsnob141oneseccontrast  = NaN(length(b1max),length(restimelist));
278 dsnob141onesecoffres    = NaN(length(b1max),length(restimelist));
279 dsnob141oneseconres     = NaN(length(b1max),length(restimelist));
280
281 %This loop is executed once for each residence time
282 %of Xe in cage, with the results stored in the four placeholder arrays at
283 %the end of the loop.
284 for i=1:1:length(restimelist)
285     %tic                %can enable timing by uncommenting
286                         %tic and toc below
287
288     restime = restimelist(i);
289
290     %blochsim is a function that performs the simulation. It is
291     %explained separately.
292     [simdata,contrast]  = blochsim(freq_1,freq_2,Mz_1,Mz_2,T1_1,T2_1,...
293                             T1_2,T2_2,restime,pulsepat,pulsetime,b1max,...
294                             satcycle,satfreq);
295
296     %This identifies the maximum contrast generated in the simulation...
297     [C,I] = max(contrast);
298     %... and stores it in a vector with a point for each residence time.
299     dsnob141onesecresult(i)     = (50*(I(satcycle)-1))';
300
301     %These hold the off-resonant, on-resonant, and contrast results from
302     %the simulation.
303     dsnob141onesecoffres(:,i)   = simdata(:,satcycle,2);
304     dsnob141oneseconres(:,i)    = simdata(:,satcycle,1);
305     dsnob141oneseccontrast(:,i) = contrast(:,satcycle);
306
307     %toc
308 end
309
310
311
312 %% dsnob 2.82 ms, one cycle
313 %This evaluates the Mz of the Xe(aq) peak following
314 %saturation with a single d-SNOB pulse of bandwidth 1000 Hz
315 %(2.82 ms) at both the onres and offres frequencies.
316
317 pulsepat = dsnob;       %pulse pattern
318 b1max = (0:10:10000)';  %peak pulse power in Hz
319 pulsetime = 0.00282 ;   %pulse duration in s
320 satcycle = 1;           %number of saturation cycles
321
322 %These hold the final results of the simulation.
323 dsnob282oneresult   = NaN(length(restimelist),1);
324 dsnob282onecontrast = NaN(length(b1max),length(restimelist));
325 dsnob282oneoffres   = NaN(length(b1max),length(restimelist));
326 dsnob282oneonres    = NaN(length(b1max),length(restimelist));
327
328 %This loop is executed once for each residence time
329 %of Xe in cage, with the results stored in the four placeholder arrays at
330 %the end of the loop.
331 for i=1:1:length(restimelist)
332     %tic                %can enable timing by uncommenting
333                         %tic and toc below
```

```
334
335     restime = restimelist(i);
336
337     %blochsim is a function that performs the simulation. It is
338     %explained separately.
339     [simdata,contrast]  = blochsim(freq_1,freq_2,Mz_1,Mz_2,T1_1,T2_1,...
340                           T1_2,T2_2,restime,pulsepat,pulsetime,b1max,...
341                           satcycle,satfreq);
342
343     %This identifies the maximum contrast generated in the simulation...
344     [C,I] = max(contrast);
345     %... and stores it in a vector with a point for each residence time.
346     dsnob282oneresult(i)     = (10*(I(satcycle)-1))';
347
348     %These hold the off-resonant, on-resonant, and contrast results from
349     %the simulation.
350     dsnob282oneoffres(:,i)   = simdata(:,satcycle,2);
351     dsnob282oneonres(:,i)    = simdata(:,satcycle,1);
352     dsnob282onecontrast(:,i) = contrast(:,satcycle);
353
354     %toc
355 end
356
357
358
359 %% dsnob 2.82 ms, one second
360 %This evaluates the Mz of the Xe(aq) peak following one second
361 %of saturation with d-SNOB pulse of bandwidth 1000 Hz (2.82 ms)
362 %at both the onres and offres frequencies.
363
364 pulsepat = dsnob;       %pulse pattern
365 b1max = (0:50:10000)';  %peak pulse power in Hz
366 pulsetime = 0.00282 ;   %pulse duration in s
367 satcycle = 355;         %number of saturation cycles
368
369 %These hold the final results of the simulation.
370 dsnob282onesecresult    = NaN(length(restimelist),1);
371 dsnob282oneseccontrast  = NaN(length(b1max),length(restimelist));
372 dsnob282onesecoffres    = NaN(length(b1max),length(restimelist));
373 dsnob282oneseconres     = NaN(length(b1max),length(restimelist));
374
375 %This loop is executed once for each residence time
376 %of Xe in cage, with the results stored in the four placeholder arrays at
377 %the end of the loop.
378 for i=1:1:length(restimelist)
379     %tic                %can enable timing by uncommenting
380                         %tic and toc below
381
382     restime = restimelist(i);
383
384     %blochsim is a function that performs the simulation. It is
385     %explained separately.
386     [simdata,contrast]  = blochsim(freq_1,freq_2,Mz_1,Mz_2,T1_1,T2_1,...
387                           T1_2,T2_2,restime,pulsepat,pulsetime,b1max,...
388                           satcycle,satfreq);
389
390     %This identifies the maximum contrast generated in the simulation...
391     [C,I] = max(contrast);
392     %... and stores it in a vector with a point for each residence time.
393     dsnob282onesecresult(i)     = (50*(I(satcycle)-1))';
```

```
394
395      %These hold the off-resonant, on-resonant, and contrast results from
396      %the simulation.
397      dsnob282onesecoffres(:,i)    = simdata(:,satcycle,2);
398      dsnob282oneseconres(:,i)     = simdata(:,satcycle,1);
399      dsnob282oneseccontrast(:,i) = contrast(:,satcycle);
400
401      %toc
402  end
```

blochsim.m

```
1  % The Bloch equation simulation function. Adapted from M. Ramirez.
2  % The inputs are as follows: frequency offres, frequency onres,
3  % magnetization intensity offres, magnetization intensity onres, T1 offres,
4  % T2 offres, T1 onres, T2 onres, residence time, pulse pattern, pulse
5  % time, peak pulse power, number of pulses in one saturation period,
6  % saturation frequency. These parameters are read from the powertesting.m
7  % file.
8  %
9  % The output is two arrays: simdata contains an array that is n x m x 2,
10 % where n is the number of peak pulse powers simulated, m is , and 2
11 % reflects two saturation frequencies, typically off and on (however, this
12 % could be used for generating z-spectra). Contrast is as uaually defined
13 % for Hyper-CEST: (off-on)/off.
14 function [simdata, contrast] = blochsim(freq_1,freq_2,Mz_1,Mz_2,T1_1,...
15                                 T2_1,T1_2,T2_2,restime,pulsepat,...
16                                 pulsetime,b1max,satcycle,satfreq)
17
18 %% Prepare
19 % Thermal equilibrium magnetization of spins.
20 Meq_1=0;
21 Meq_2=0;
22
23 % Convert T1 and T2 values into R1, R2 values.
24 R1_1=1/T1_1;
25 R1_2=1/T1_2;
26 R2_1=1/T2_1;
27 R2_2=1/T2_2;
28
29 % 1/t_c (units of Hz), the cage residence/exchange time
30 k_rev=1/restime;
31 % 1/t_w, the bulk water residence time
32 k_fwd=(Mz_2/Mz_1)*k_rev;
33
34 if k_fwd==0
35    k_rev = 0;
36 end
37
38
39 %% Initial Magnetization Matrices
40 %B accounts for relaxation of the z-component back to thermal polarization.
41 B =    [0;
42         0;
43      R1_2*Meq_2;
```

```
          0;
          0;
       R1_1*Meq_1];


%M0 is the initial magnetization vector.
M0 =    [0;
          0;
         Mz_2;
          0;
          0;
         Mz_1];


%% Shaped Pulses
% Start with the pulse shape you want in a two column format with relative
% amplitude (col 1) and relative time duration (col 2). Scale these as
% appropriate.

% Since the simulation must do each discrete step of the pulse as defined
% by the pulse shape (which, since it was take from the VNMR files, mimics
% the discretization of the spectrometer), t is an array that holds the
% length of time in seconds for each discrete step of the pulse.
t = ((pulsetime)/(sum(pulsepat(:,2)))).*(pulsepat(:,2));

% zspectrum is a placeholder that holds the output of the simulation until
% it is written to simdata.
zspectrum = NaN(length(b1max),satcycle,length(satfreq));

% This option is used for simulatneously varying saturation frequencies
% and saturation powers. It is computationally intensive——recommended only
% for use with cw pulse simulations. Its complement in the simulation code
% is found before the final end statement.
%
% powerarrayedzspec = NaN(size(b1max),satcycle,length(satfreq));


%% z—spectrum: vary sattof
% This part is the actual simulation.

for powerindex = 1:1:size(b1max);

    %This is the peak power applied for each discrete step of the shaped
    %pulse.
    p = b1max(powerindex).*pulsepat(:,1);

    %This initialiazes the Mz vector.
    M = NaN(length(satfreq),length(p),6);

    %For each frequency...
    for l=1:length(satfreq)

        %Reset the answer to zero so each saturation frequency point does
        %not use information from theprevious simulation.
        Mfinal = M0;

        tic

        %For each complete saturation pulse...
        for k=1:1:satcycle
```

```
104
105             %And for each discrete step of the pulse shape...
106             for j=1:length(p);
107
108                 %The peak power for the discrete step.
109                 power=p(j);
110
111                 %The length of time that power is applied.
112                 tt=t(j);
113
114                 %This matrix is a two-pool model showing exchange between
115                 %the two populations (freq_1 and freq_2), with the
116                 %exchange in the cross terms, longitudinal relaxation
117                 %along the diagonal, and coherences in the off diagonal
118                 %terms of the diagonal 3x3 block elements.
119                 A= [-(R2_2+k_rev)              2*pi*(freq_2-satfreq(l))...
120                     0                          k_fwd...
121                     0                          0;
122                     -2*pi*(freq_2-satfreq(l))  -(R2_2+k_rev)...
123                     2*pi*power                 0 ...
124                     k_fwd                      0;
125                     0                          -2*pi*power...
126                     -(R1_2+k_rev)              0 ...
127                     0                          k_fwd;
128                     k_rev                      0 ...
129                     0                          -(R2_1+k_fwd)...
130                     2*pi*(freq_1-satfreq(l))   0;
131                     0                          k_rev...
132                     0                          -2*pi*(freq_1-satfreq(l))...
133                     -(R2_1+k_fwd)              2*pi*power;
134                     0                          0 ...
135                     k_rev                      0 ...
136                     -2*pi*power                -(R1_1+k_fwd)];
137
138                 %This is the matrix multiplication that solves the Bloch
139                 %differential equations.
140                 M(l,j,:) = expm(A * tt) * (Mfinal + A\B) - A\B;
141
142                 %The result from the Bloch simulation of a discrete time
143                 %point is stored as Mfinal.
144                 Mfinal(:) = M(l,j,:);
145             end
146
147             %The result from the Bloch simulation of a complete saturation
148             %pulse is stored as Mfinal.
149             Mfinal(:) = M(l,j,:);
150
151             %zspectrum then holds the result of a complete saturation
152             %pulse
153             zspectrum(powerindex,k,l) = Mfinal(6);
154         end
155         toc
156         fprintf(' %i\n',l)
157     end
158
159     %This option is for arrayed powers as well as varied saturation
160     %frequencies.
161 %   powerarrayedzspec(powerindex,k,l) = [powerindex, zspectrum(:,1),...
162 %                                        zspectrum(:,2)];
163 end
```

```
164
165 %This vector holds the total saturation time.
166 time = (pulsetime):(pulsetime):(satcycle*pulsetime);
167
168 %The results are output.
169 simdata = zspectrum;
170 contrast = (simdata(:,:,2) - simdata(:,:,1))./simdata(:,:,2);
171
172 %If you are simulating saturation profiles, this option allows the total
173 %saturation time to be output, also.
174 % simdata = [time',zspectrum(:,:)];
```

As the matrices in the code are visually difficult to interpret, they are reproduced here.

Lines 41–46:

$$B = \begin{bmatrix} 0 \\ 0 \\ R_{1,\,cage} M_{eq,\,cage} \\ 0 \\ 0 \\ R_{1,\,aq} M_{eq,\,aq} \end{bmatrix}$$

Lines 50–55:

$$M_0 = \begin{bmatrix} 0 \\ 0 \\ M_{0,\,cage} \\ 0 \\ 0 \\ M_{0,\,aq} \end{bmatrix}$$

Lines 119–136:

$$A = \begin{bmatrix} a & b \\ c & d \end{bmatrix}$$

Here, a and d represent the populations of the two spin pools, together with coherences, saturation at frequency ω_{sat}, relaxation, and exchange out of the two pools, and b and c represent exchange into the two pools. Their mathematical forms are:

$$a = \begin{bmatrix} -R_{2,\,cage} - k_{rev} & 2\pi\left(\omega_{cage} - \omega_{sat}\right) & 0 \\ -2\pi\left(\omega_{cage} - \omega_{sat}\right) & -R_{2,\,cage} - k_{rev} & 2\pi B_{1,\,sat} \\ 0 & -2\pi B_{1,\,sat} & -R_{1,\,cage} - k_{rev} \end{bmatrix}$$

$$d = \begin{bmatrix} -R_{2,\,aq} - k_{fwd} & 2\pi\left(\omega_{aq} - \omega_{sat}\right) & 0 \\ -2\pi\left(\omega_{aq} - \omega_{sat}\right) & -R_{2,\,aq} - k_{fwd} & 2\pi B_{1,\,sat} \\ 0 & -2\pi B_{1,\,sat} & -R_{1,\,aq} - k_{fwd} \end{bmatrix}$$

$$b = \begin{bmatrix} k_{fwd} & 0 & 0 \\ 0 & k_{fwd} & 0 \\ 0 & 0 & k_{fwd} \end{bmatrix}$$

$$c = \begin{bmatrix} k_{rev} & 0 & 0 \\ 0 & k_{rev} & 0 \\ 0 & 0 & k_{rev} \end{bmatrix}$$

The general Bloch-McConnell equation

$$\frac{d}{dt} \begin{bmatrix} M_{cage} \\ M_{aq} \end{bmatrix} = A \begin{bmatrix} M_{cage} \\ M_{aq} \end{bmatrix}, \tag{B.1}$$

results in the mathematical operation, shown in line 140 of `blochsim.m`:

$$M(t_{sat}) = e^{(A \cdot t_{sat})} + \left(M + A^{-1}B\right) - A^{-1}B, \tag{B.2}$$

where M starts as M_0 and is constantly refreshed to be the most current magnetization of the system during the time course of the simulation.

Appendix C

Lipid Fit Parameters

Table C.1: Fit parameters for the 0% lipid suspension

T [°C]	peak number	x_0 [ppm]	I [arb]	γ [ppm]	*area* [arb]
25	1	189.2914 ± 0.0004	0.5677 ± 0.0023	0.1706 ± 0.0010	0.1521 ± 0.0007
25	2	61.9460 ± 0.1885	0.0033 ± 0.0008	1.4790 ± 0.5373	0.0077 ± 0.0020
25	3	3.1552 ± 0.0582	0.0045 ± 0.0020	0.2621 ± 0.1676	0.0018 ± 0.0008
25	4	-0.0589 ± 0.0378	0.0089 ± 0.0016	0.4273 ± 0.1072	0.0059 ± 0.0011
5	1	187.3914 ± 0.0004	1.0000 ± 0.0043	0.1631 ± 0.0010	0.2562 ± 0.0012
5	2	56.1392 ± 0.2112	0.0046 ± 0.0018	1.1046 ± 0.6009	0.0079 ± 0.0031
5	3	2.9660 ± 0.0840	0.0055 ± 0.0037	0.2457 ± 0.2332	0.0021 ± 0.0014
5	4	-0.1664 ± 0.0493	0.0106 ± 0.0032	0.3231 ± 0.1400	0.0054 ± 0.0017
10	1	187.8883 ± 0.0004	0.7453 ± 0.0026	0.1889 ± 0.0009	0.2211 ± 0.0008
10	2	57.4629 ± 0.1840	0.0039 ± 0.0010	1.4800 ± 0.5244	0.0092 ± 0.0023
10	3	3.0359 ± 0.0619	0.0051 ± 0.0023	0.2752 ± 0.1745	0.0022 ± 0.0010
10	4	-0.1222 ± 0.0280	0.0114 ± 0.0022	0.2840 ± 0.0789	0.0051 ± 0.0010
15	1	188.4713 ± 0.0004	0.7393 ± 0.0033	0.1598 ± 0.0010	0.1856 ± 0.0009
15	2	59.0655 ± 0.1989	0.0042 ± 0.0011	1.5023 ± 0.5672	0.0099 ± 0.0027
15	3	3.0337 ± 0.0888	0.0045 ± 0.0023	0.3495 ± 0.2516	0.0025 ± 0.0013
15	4	-0.0758 ± 0.0331	0.0106 ± 0.0027	0.2651 ± 0.0951	0.0044 ± 0.0011
20	1	188.9447 ± 0.0004	0.6399 ± 0.0030	0.1559 ± 0.0010	0.1567 ± 0.0007
20	2	60.8006 ± 0.1860	0.0039 ± 0.0009	1.6122 ± 0.5307	0.0099 ± 0.0023
20	3	3.1471 ± 0.0704	0.0043 ± 0.0021	0.2862 ± 0.2004	0.0019 ± 0.0010
20	4	0.0007 ± 0.0340	0.0093 ± 0.0021	0.3058 ± 0.0968	0.0045 ± 0.0010
25	1	189.3194 ± 0.0003	0.5676 ± 0.0027	0.1518 ± 0.0010	0.1354 ± 0.0006
25	2	62.2523 ± 0.1339	0.0043 ± 0.0008	1.4983 ± 0.3818	0.0101 ± 0.0018
25	3	3.1265 ± 0.0545	0.0044 ± 0.0018	0.2632 ± 0.1525	0.0018 ± 0.0008
25	4	-0.0515 ± 0.0326	0.0088 ± 0.0015	0.3727 ± 0.0923	0.0052 ± 0.0009

Continued on next page

Continued from previous page

T [°C]	peak number	x_0 [ppm]	I [arb]	γ [ppm]	area [arb]
30	1	189.5954 ± 0.0004	0.4431 ± 0.0018	0.1758 ± 0.0010	0.1224 ± 0.0005
30	2	63.7504 ± 0.1242	0.0043 ± 0.0006	1.8347 ± 0.3547	0.0123 ± 0.0017
30	3	3.1949 ± 0.0420	0.0047 ± 0.0016	0.2482 ± 0.1163	0.0018 ± 0.0006
30	4	0.0346 ± 0.0359	0.0073 ± 0.0012	0.4481 ± 0.1019	0.0051 ± 0.0008
35	1	189.8443 ± 0.0003	0.4012 ± 0.0017	0.1618 ± 0.0010	0.1020 ± 0.0004
35	2	65.4450 ± 0.0976	0.0040 ± 0.0004	1.8596 ± 0.2789	0.0118 ± 0.0013
35	3	3.2479 ± 0.0318	0.0048 ± 0.0011	0.2824 ± 0.0903	0.0021 ± 0.0005
35	4	0.1060 ± 0.0166	0.0097 ± 0.0010	0.3055 ± 0.0468	0.0046 ± 0.0005
40	1	190.0018 ± 0.0003	0.3226 ± 0.0012	0.1792 ± 0.0009	0.0908 ± 0.0003
40	2	66.8518 ± 0.0761	0.0040 ± 0.0004	1.7106 ± 0.2171	0.0108 ± 0.0010
40	3	3.2663 ± 0.0467	0.0034 ± 0.0007	0.4743 ± 0.1328	0.0026 ± 0.0005
40	4	0.1310 ± 0.0216	0.0071 ± 0.0007	0.4284 ± 0.0613	0.0048 ± 0.0005

Fit is a Lorentzian curve as defined by $f\left(x;\, x_0, \gamma, I\right) = I\left[\frac{\gamma^2}{4(x-x_0)^2+\gamma^2}\right]$.
γ is the full-width at half maximum (FWHM).

Table C.2: Fit parameters for the 1% lipid suspension

T [°C]	peak number	x_0 [ppm]	I [arb]	γ [ppm]	*area* [arb]
25	1	191.5632 ± 0.1561	0.0038 ± 0.0005	2.1349 ± 0.2352	0.0128 ± 0.0028
25	2	190.4567 ± 0.0048	0.0520 ± 0.0006	1.1729 ± 0.0174	0.0958 ± 0.0024
25	3	72.6129 ± 0.2458	0.0010 ± 0.0001	3.6890 ± 0.7200	0.0056 ± 0.0008
25	4	62.5298 ± 0.0393	0.0041 ± 0.0002	1.6878 ± 0.1134	0.0109 ± 0.0005
25	5	3.1765 ± 0.0128	0.0050 ± 0.0005	0.2628 ± 0.0363	0.0020 ± 0.0002
25	6	0.0192 ± 0.0139	0.0062 ± 0.0004	0.4811 ± 0.0394	0.0047 ± 0.0003
5	1	194.9009 ± 0.1791	0.0020 ± 0.0001	6.5685 ± 0.5648	0.0201 ± 0.0013
5	2	188.3064 ± 0.0025	0.0594 ± 0.0002	1.3764 ± 0.0080	0.1285 ± 0.0006
5	3	69.0816 ± 0.1908	0.0015 ± 0.0001	4.9410 ± 0.5596	0.0115 ± 0.0010
5	4	56.4293 ± 0.0242	0.0054 ± 0.0002	1.0652 ± 0.0693	0.0091 ± 0.0004
5	5	3.1132 ± 0.0469	0.0024 ± 0.0003	0.7967 ± 0.1341	0.0030 ± 0.0004
5	6	-0.1605 ± 0.0060	0.0146 ± 0.0004	0.4722 ± 0.0171	0.0109 ± 0.0003
10	1	193.0061 ± 0.1483	0.0028 ± 0.0001	5.8112 ± 0.4151	0.0260 ± 0.0016
10	2	188.9609 ± 0.0033	0.0481 ± 0.0002	1.4192 ± 0.0122	0.1073 ± 0.0009
10	3	69.9083 ± 0.2813	0.0011 ± 0.0001	6.1732 ± 0.8367	0.0111 ± 0.0011
10	4	57.6690 ± 0.0259	0.0053 ± 0.0002	1.1122 ± 0.0744	0.0092 ± 0.0004
10	5	3.1029 ± 0.0177	0.0045 ± 0.0004	0.3860 ± 0.0504	0.0027 ± 0.0003
10	6	-0.1325 ± 0.0078	0.0117 ± 0.0004	0.5048 ± 0.0222	0.0093 ± 0.0003
15	1	191.4616 ± 0.1088	0.0052 ± 0.0002	3.4982 ± 0.1988	0.0288 ± 0.0023
15	2	189.5888 ± 0.0045	0.0419 ± 0.0003	1.3425 ± 0.0195	0.0884 ± 0.0017
15	3	70.1586 ± 0.1860	0.0014 ± 0.0001	4.2225 ± 0.5443	0.0095 ± 0.0009
15	4	59.2458 ± 0.0282	0.0052 ± 0.0002	1.2572 ± 0.0808	0.0102 ± 0.0005
15	5	3.0477 ± 0.0174	0.0045 ± 0.0004	0.3556 ± 0.0492	0.0025 ± 0.0002
15	6	-0.1185 ± 0.0054	0.0155 ± 0.0004	0.4155 ± 0.0153	0.0101 ± 0.0003
20	1	191.8709 ± 0.1340	0.0045 ± 0.0003	3.7061 ± 0.2131	0.0265 ± 0.0023
20	2	190.1137 ± 0.0043	0.0409 ± 0.0004	1.3016 ± 0.0200	0.0837 ± 0.0017
20	3	71.6839 ± 0.1649	0.0016 ± 0.0001	4.3564 ± 0.4851	0.0108 ± 0.0009
20	4	60.9419 ± 0.0338	0.0046 ± 0.0002	1.5208 ± 0.0976	0.0109 ± 0.0005
20	5	3.1125 ± 0.0158	0.0048 ± 0.0004	0.3754 ± 0.0448	0.0029 ± 0.0002
20	6	0.0074 ± 0.0079	0.0095 ± 0.0004	0.3581 ± 0.0223	0.0054 ± 0.0002
25	1	192.3038 ± 0.1680	0.0031 ± 0.0002	3.1868 ± 0.3178	0.0156 ± 0.0021
25	2	190.5355 ± 0.0043	0.0416 ± 0.0003	1.2739 ± 0.0184	0.0833 ± 0.0016
25	3	73.0848 ± 0.2827	0.0011 ± 0.0001	6.4429 ± 0.8550	0.0116 ± 0.0011
25	4	62.2361 ± 0.0354	0.0044 ± 0.0002	1.4903 ± 0.1037	0.0102 ± 0.0005
25	5	3.1029 ± 0.0151	0.0044 ± 0.0005	0.2748 ± 0.0428	0.0019 ± 0.0002
25	6	-0.0316 ± 0.0056	0.0149 ± 0.0004	0.4353 ± 0.0159	0.0102 ± 0.0003
30	1	191.4395 ± 0.1459	0.0059 ± 0.0014	1.7079 ± 0.1365	0.0158 ± 0.0046
30	2	190.7431 ± 0.0084	0.0448 ± 0.0016	1.0478 ± 0.0268	0.0737 ± 0.0043
30	3	73.9446 ± 0.1775	0.0014 ± 0.0001	4.0975 ± 0.5252	0.0090 ± 0.0008
30	4	63.7364 ± 0.0464	0.0038 ± 0.0002	2.1207 ± 0.1354	0.0128 ± 0.0006
30	5	3.2523 ± 0.0130	0.0041 ± 0.0006	0.1779 ± 0.0355	0.0011 ± 0.0002

Continued on next page

Continued from previous page

T [°C]	peak number	x_0 [ppm]	I [arb]	γ [ppm]	area [arb]
30	6	0.0574 ± 0.0065	0.0110 ± 0.0004	0.3423 ± 0.0185	0.0059 ± 0.0002
35	1	191.3239 ± 0.1187	0.0072 ± 0.0031	1.0674 ± 0.1232	0.0120 ± 0.0064
35	2	190.8889 ± 0.0143	0.0464 ± 0.0032	0.9318 ± 0.0240	0.0679 ± 0.0063
35	3	74.1670 ± 0.1243	0.0014 ± 0.0002	2.1532 ± 0.3608	0.0046 ± 0.0006
35	4	65.6357 ± 0.0529	0.0033 ± 0.0002	2.2623 ± 0.1535	0.0117 ± 0.0006
35	5	3.2523 ± 0.0160	0.0040 ± 0.0004	0.3078 ± 0.0453	0.0019 ± 0.0002
35	6	0.1377 ± 0.0049	0.0125 ± 0.0004	0.2864 ± 0.0141	0.0056 ± 0.0002
40	1	192.0586 ± 0.1531	0.0009 ± 0.0003	0.8488 ± 0.4982	0.0012 ± 0.0007
40	2	190.9536 ± 0.0032	0.0488 ± 0.0003	0.9545 ± 0.0101	0.0732 ± 0.0008
40	3	75.3301 ± 0.4109	0.0011 ± 0.0001	9.9710 ± 1.2875	0.0169 ± 0.0017
40	4	67.0609 ± 0.0497	0.0034 ± 0.0002	1.8089 ± 0.1644	0.0096 ± 0.0007
40	5	3.3488 ± 0.0147	0.0044 ± 0.0005	0.2660 ± 0.0410	0.0018 ± 0.0002
40	6	0.1951 ± 0.0082	0.0094 ± 0.0004	0.3828 ± 0.0232	0.0057 ± 0.0002
25	1	191.7384 ± 0.0978	0.0056 ± 0.0005	2.0442 ± 0.1558	0.0179 ± 0.0026
25	2	190.6356 ± 0.0059	0.0407 ± 0.0006	1.1613 ± 0.0209	0.0743 ± 0.0022
25	3	72.3406 ± 0.1442	0.0019 ± 0.0001	5.0452 ± 0.4366	0.0150 ± 0.0010
25	4	62.9325 ± 0.0443	0.0038 ± 0.0002	1.9859 ± 0.1313	0.0120 ± 0.0006
25	5	3.1883 ± 0.0164	0.0038 ± 0.0005	0.2623 ± 0.0459	0.0016 ± 0.0002
25	6	0.0457 ± 0.0066	0.0105 ± 0.0004	0.3326 ± 0.0188	0.0055 ± 0.0002

Fit is a Lorentzian curve as defined by $f\left(x;\, x_0, \gamma, I\right) = I\left[\frac{\gamma^2}{4(x-x_0)^2+\gamma^2}\right]$.
γ is the full-width at half maximum (FWHM).

Table C.3: Fit parameters for the 2% lipid suspension

T [°C]	peak number	x_0 [ppm]	I [arb]	γ [ppm]	*area* [arb]
25	1	193.2512 ± 0.0545	0.0053 ± 0.0002	1.9111 ± 0.1538	0.0158 ± 0.0015
25	2	191.4587 ± 0.0066	0.0378 ± 0.0003	1.6814 ± 0.0203	0.0998 ± 0.0014
25	3	72.7587 ± 0.1336	0.0016 ± 0.0002	2.7914 ± 0.3860	0.0070 ± 0.0007
25	4	62.4385 ± 0.0501	0.0032 ± 0.0002	1.5439 ± 0.1437	0.0077 ± 0.0005
25	5	3.1463 ± 0.0134	0.0043 ± 0.0006	0.2047 ± 0.0398	0.0014 ± 0.0002
25	6	-0.0339 ± 0.0054	0.0175 ± 0.0003	0.5474 ± 0.0154	0.0151 ± 0.0003
5	1	194.2619 ± 0.1387	0.0039 ± 0.0001	7.1479 ± 0.3828	0.0438 ± 0.0022
5	2	189.1618 ± 0.0069	0.0316 ± 0.0002	2.2221 ± 0.0263	0.1105 ± 0.0013
5	3	69.3289 ± 0.1388	0.0020 ± 0.0001	4.1932 ± 0.4048	0.0135 ± 0.0009
5	4	56.6008 ± 0.0404	0.0040 ± 0.0002	1.3885 ± 0.1156	0.0088 ± 0.0005
5	5	2.9969 ± 0.0130	0.0059 ± 0.0005	0.3050 ± 0.0371	0.0028 ± 0.0002
5	6	-0.1686 ± 0.0084	0.0117 ± 0.0004	0.4992 ± 0.0238	0.0092 ± 0.0003
1	1	195.7431 ± 0.1342	0.0032 ± 0.0001	7.9035 ± 0.4242	0.0399 ± 0.0017
1	2	188.3955 ± 0.0054	0.0375 ± 0.0002	2.1880 ± 0.0181	0.1289 ± 0.0009
1	3	68.0171 ± 0.0842	0.0028 ± 0.0002	3.0606 ± 0.2431	0.0134 ± 0.0008
1	4	55.3295 ± 0.0392	0.0038 ± 0.0002	1.2603 ± 0.1118	0.0076 ± 0.0005
1	5	2.9071 ± 0.0111	0.0059 ± 0.0005	0.2323 ± 0.0305	0.0022 ± 0.0002
1	6	-0.2230 ± 0.0059	0.0135 ± 0.0005	0.3545 ± 0.0168	0.0075 ± 0.0003
10	1	193.8276 ± 0.1861	0.0026 ± 0.0001	5.0971 ± 0.4927	0.0205 ± 0.0021
10	2	189.9488 ± 0.0114	0.0209 ± 0.0002	2.4134 ± 0.0423	0.0792 ± 0.0015
10	3	69.2737 ± 0.1109	0.0022 ± 0.0001	3.6815 ± 0.3230	0.0129 ± 0.0008
10	4	57.7080 ± 0.0691	0.0024 ± 0.0002	1.6239 ± 0.1984	0.0061 ± 0.0005
10	5	2.9005 ± 0.0118	0.0054 ± 0.0005	0.2391 ± 0.0325	0.0020 ± 0.0002
10	6	-0.2989 ± 0.0068	0.0120 ± 0.0004	0.3961 ± 0.0192	0.0075 ± 0.0003
15	1	193.0775 ± 0.1916	0.0037 ± 0.0003	4.3880 ± 0.3377	0.0254 ± 0.0031
15	2	190.6327 ± 0.0142	0.0198 ± 0.0003	2.2043 ± 0.0551	0.0686 ± 0.0026
15	3	70.7424 ± 0.0664	0.0030 ± 0.0002	2.6283 ± 0.1915	0.0124 ± 0.0006
15	4	59.4372 ± 0.0690	0.0022 ± 0.0002	1.5804 ± 0.1975	0.0056 ± 0.0005
15	5	3.0492 ± 0.0152	0.0045 ± 0.0004	0.3086 ± 0.0429	0.0022 ± 0.0002
15	6	-0.0545 ± 0.0038	0.0188 ± 0.0004	0.3325 ± 0.0107	0.0098 ± 0.0002
20	1	192.5099 ± 0.4743	0.0013 ± 0.0006	2.3051 ± 0.8875	0.0046 ± 0.0037
20	2	191.0795 ± 0.0230	0.0223 ± 0.0007	2.0697 ± 0.0511	0.0724 ± 0.0036
20	3	71.3217 ± 0.1112	0.0022 ± 0.0001	4.0184 ± 0.3271	0.0141 ± 0.0008
20	4	61.1164 ± 0.0713	0.0023 ± 0.0002	1.7370 ± 0.2066	0.0062 ± 0.0005
20	5	3.0911 ± 0.0093	0.0063 ± 0.0005	0.2272 ± 0.0272	0.0022 ± 0.0002
20	6	-0.0994 ± 0.0065	0.0115 ± 0.0004	0.3701 ± 0.0185	0.0067 ± 0.0002
25	1	192.1904 ± 0.1610	0.0074 ± 0.0021	2.0222 ± 0.1419	0.0236 ± 0.0078
25	2	191.3953 ± 0.0345	0.0204 ± 0.0022	1.5120 ± 0.0786	0.0485 ± 0.0075
25	3	71.9092 ± 0.0965	0.0026 ± 0.0001	4.2886 ± 0.2872	0.0175 ± 0.0009
25	4	62.4937 ± 0.0623	0.0026 ± 0.0002	1.8281 ± 0.1823	0.0075 ± 0.0005
25	5	3.1611 ± 0.0177	0.0044 ± 0.0004	0.4157 ± 0.0501	0.0029 ± 0.0002

Continued on next page

Continued from previous page

T [°C]	peak number	x_0 [ppm]	I [arb]	γ [ppm]	area [arb]
25	6	-0.0537 ± 0.0061	0.0135 ± 0.0004	0.4582 ± 0.0172	0.0097 ± 0.0003
30	1	192.5945 ± 0.2993	0.0031 ± 0.0013	2.1003 ± 0.3240	0.0103 ± 0.0055
30	2	191.6707 ± 0.0234	0.0221 ± 0.0014	1.4942 ± 0.0599	0.0518 ± 0.0052
30	3	73.2144 ± 0.0990	0.0024 ± 0.0001	4.0705 ± 0.2928	0.0154 ± 0.0008
30	4	64.1111 ± 0.0743	0.0019 ± 0.0002	1.4973 ± 0.2158	0.0046 ± 0.0005
30	5	3.1147 ± 0.0129	0.0044 ± 0.0005	0.2154 ± 0.0347	0.0015 ± 0.0002
30	6	0.0376 ± 0.0038	0.0215 ± 0.0003	0.4734 ± 0.0107	0.0160 ± 0.0003
35	1	192.2530 ± 0.1543	0.0030 ± 0.0019	0.9998 ± 0.3612	0.0048 ± 0.0046
35	2	191.6662 ± 0.0373	0.0208 ± 0.0018	1.3310 ± 0.0407	0.0435 ± 0.0048
35	3	74.1817 ± 0.1510	0.0019 ± 0.0001	5.0684 ± 0.4786	0.0148 ± 0.0011
35	4	65.8153 ± 0.1394	0.0016 ± 0.0001	3.5061 ± 0.4407	0.0091 ± 0.0009
35	5	3.2074 ± 0.0147	0.0043 ± 0.0005	0.2805 ± 0.0414	0.0019 ± 0.0002
35	6	0.1929 ± 0.0055	0.0134 ± 0.0004	0.3837 ± 0.0157	0.0081 ± 0.0002
40	1	192.2706 ± 0.1994	0.0038 ± 0.0015	1.5517 ± 0.2660	0.0093 ± 0.0049
40	2	191.5139 ± 0.0343	0.0164 ± 0.0016	1.3016 ± 0.0700	0.0335 ± 0.0048
40	3	74.8913 ± 0.2739	0.0015 ± 0.0001	8.4754 ± 0.8656	0.0203 ± 0.0017
40	4	66.9710 ± 0.1346	0.0015 ± 0.0002	2.6242 ± 0.4578	0.0063 ± 0.0009
40	5	3.2847 ± 0.0200	0.0036 ± 0.0004	0.3374 ± 0.0568	0.0019 ± 0.0002
40	6	0.2069 ± 0.0054	0.0131 ± 0.0004	0.3356 ± 0.0154	0.0069 ± 0.0002
25	1	191.5595 ± 0.0412	0.0163 ± 0.0020	1.7115 ± 0.1143	0.0438 ± 0.0083
25	2	192.4731 ± 0.4066	0.0034 ± 0.0019	2.5537 ± 0.2844	0.0137 ± 0.0087
25	3	72.2868 ± 0.0786	0.0028 ± 0.0001	3.4695 ± 0.2391	0.0153 ± 0.0008
25	4	63.2122 ± 0.1923	0.0012 ± 0.0001	3.8760 ± 0.5865	0.0074 ± 0.0008
25	5	3.1500 ± 0.0113	0.0052 ± 0.0005	0.2551 ± 0.0326	0.0021 ± 0.0002
25	6	0.0972 ± 0.0034	0.0210 ± 0.0004	0.3753 ± 0.0097	0.0124 ± 0.0002
5	1	195.5966 ± 0.2126	0.0015 ± 0.0001	5.7737 ± 0.6791	0.0140 ± 0.0013
5	2	189.1442 ± 0.0107	0.0187 ± 0.0002	2.5670 ± 0.0357	0.0755 ± 0.0009
5	3	68.1040 ± 0.0769	0.0030 ± 0.0001	3.5904 ± 0.2234	0.0168 ± 0.0008
5	4	56.1650 ± 0.0736	0.0019 ± 0.0002	1.4007 ± 0.2107	0.0043 ± 0.0005
5	5	2.9306 ± 0.0091	0.0065 ± 0.0005	0.2484 ± 0.0264	0.0026 ± 0.0002
5	6	-0.1759 ± 0.0057	0.0121 ± 0.0004	0.3277 ± 0.0162	0.0062 ± 0.0002

Fit is a Lorentzian curve as defined by $f\left(x;\, x_0, \gamma, I\right) = I\left[\frac{\gamma^2}{4(x-x_0)^2+\gamma^2}\right]$.
γ is the full-width at half maximum (FWHM).

Table C.4: Fit parameters for the 5% lipid suspension

T [°C]	peak number	x_0 [ppm]	I [arb]	γ [ppm]	*area* [arb]
25	1	194.0256 ± 0.3217	0.0012 ± 0.0017	0.9921 ± 0.8487	0.0019 ± 0.0042
25	2	193.4220 ± 0.0142	0.0533 ± 0.0016	1.4261 ± 0.0142	0.1194 ± 0.0044
25	3	72.8897 ± 0.0998	0.0021 ± 0.0001	3.4946 ± 0.3126	0.0116 ± 0.0008
25	4	63.0208 ± 0.3854	0.0007 ± 0.0001	6.3073 ± 1.2185	0.0074 ± 0.0011
25	5	3.1287 ± 0.0133	0.0044 ± 0.0004	0.2798 ± 0.0374	0.0019 ± 0.0002
25	6	-0.0324 ± 0.0045	0.0134 ± 0.0004	0.2906 ± 0.0126	0.0061 ± 0.0002
5	1	196.1229 ± 0.0812	0.0063 ± 0.0002	4.7413 ± 0.2136	0.0472 ± 0.0027
5	2	192.1057 ± 0.0306	0.0137 ± 0.0002	3.9870 ± 0.0913	0.0861 ± 0.0026
5	3	68.6635 ± 0.1259	0.0021 ± 0.0001	4.1097 ± 0.4025	0.0136 ± 0.0011
5	4	56.9770 ± 0.8151	0.0005 ± 0.0001	8.7398 ± 2.6260	0.0068 ± 0.0016
5	5	2.9086 ± 0.0121	0.0063 ± 0.0004	0.3548 ± 0.0342	0.0035 ± 0.0002
5	6	-0.2172 ± 0.0035	0.0189 ± 0.0005	0.2646 ± 0.0100	0.0079 ± 0.0002
10	1	195.2874 ± 0.0799	0.0065 ± 0.0004	3.2796 ± 0.1909	0.0335 ± 0.0033
10	2	192.7918 ± 0.0342	0.0165 ± 0.0003	3.4656 ± 0.0763	0.0896 ± 0.0034
10	3	69.2112 ± 0.0995	0.0022 ± 0.0001	3.3453 ± 0.3045	0.0116 ± 0.0008
10	4	56.3719 ± 0.6117	0.0006 ± 0.0001	8.4047 ± 1.9233	0.0077 ± 0.0013
10	5	2.9829 ± 0.0165	0.0045 ± 0.0004	0.3851 ± 0.0469	0.0027 ± 0.0002
10	6	-0.1619 ± 0.0041	0.0161 ± 0.0004	0.3080 ± 0.0117	0.0078 ± 0.0002
15	1	194.8140 ± 0.0801	0.0085 ± 0.0008	2.6119 ± 0.1349	0.0350 ± 0.0046
15	2	193.3447 ± 0.0264	0.0234 ± 0.0008	2.4534 ± 0.0504	0.0901 ± 0.0045
15	3	70.2528 ± 0.0948	0.0023 ± 0.0001	4.3366 ± 0.2747	0.0160 ± 0.0007
15	4	3.0492 ± 0.0182	0.0039 ± 0.0003	0.4418 ± 0.0515	0.0027 ± 0.0002
15	5	-0.0861 ± 0.0027	0.0194 ± 0.0004	0.2504 ± 0.0079	0.0076 ± 0.0002
20	1	194.4813 ± 0.0963	0.0112 ± 0.0015	2.3472 ± 0.0872	0.0412 ± 0.0066
20	2	193.5390 ± 0.0185	0.0310 ± 0.0016	1.6491 ± 0.0475	0.0803 ± 0.0062
20	3	71.1811 ± 0.0835	0.0026 ± 0.0001	3.7937 ± 0.2413	0.0153 ± 0.0007
20	4	3.0617 ± 0.0164	0.0038 ± 0.0004	0.3166 ± 0.0465	0.0019 ± 0.0002
20	5	-0.0604 ± 0.0033	0.0174 ± 0.0004	0.2651 ± 0.0093	0.0072 ± 0.0002
25	1	194.0080 ± 0.0801	0.0139 ± 0.0027	1.5927 ± 0.0604	0.0349 ± 0.0077
25	2	193.4264 ± 0.0154	0.0424 ± 0.0028	1.1934 ± 0.0344	0.0795 ± 0.0074
25	3	71.5543 ± 0.1056	0.0023 ± 0.0001	4.8102 ± 0.3067	0.0174 ± 0.0008
25	4	3.0867 ± 0.0120	0.0046 ± 0.0004	0.2489 ± 0.0348	0.0018 ± 0.0002
25	5	-0.0228 ± 0.0030	0.0189 ± 0.0004	0.2586 ± 0.0085	0.0077 ± 0.0002
30	1	193.5037 ± 0.0688	0.0188 ± 0.0066	1.0489 ± 0.0488	0.0310 ± 0.0120
30	2	193.1702 ± 0.0197	0.0529 ± 0.0067	0.9394 ± 0.0268	0.0781 ± 0.0119
30	3	72.6549 ± 0.0820	0.0028 ± 0.0001	4.5991 ± 0.2379	0.0202 ± 0.0008
30	4	3.1743 ± 0.0423	0.0022 ± 0.0003	0.7335 ± 0.1205	0.0025 ± 0.0003
30	5	0.0964 ± 0.0024	0.0246 ± 0.0004	0.3162 ± 0.0069	0.0122 ± 0.0002
35	1	193.0804 ± 0.0900	0.0182 ± 0.0154	0.7961 ± 0.0848	0.0227 ± 0.0215
35	2	192.8647 ± 0.0307	0.0584 ± 0.0153	0.8322 ± 0.0190	0.0763 ± 0.0216
35	3	72.9685 ± 0.1208	0.0022 ± 0.0001	5.7762 ± 0.3526	0.0195 ± 0.0009

Continued on next page

Continued from previous page

T [°C]	peak number	x_0 [ppm]	I [arb]	γ [ppm]	area [arb]
35	4	3.2052 ± 0.0229	0.0030 ± 0.0003	0.3908 ± 0.0650	0.0018 ± 0.0002
35	5	0.0987 ± 0.0033	0.0178 ± 0.0004	0.2970 ± 0.0094	0.0083 ± 0.0002
40	1	192.8934 ± 0.1028	0.0083 ± 0.0031	1.0508 ± 0.0940	0.0137 ± 0.0061
40	2	192.4826 ± 0.0104	0.0565 ± 0.0032	0.8576 ± 0.0198	0.0761 ± 0.0060
40	3	74.5704 ± 0.1218	0.0023 ± 0.0001	6.1115 ± 0.3561	0.0218 ± 0.0009
40	4	3.2869 ± 0.0169	0.0039 ± 0.0004	0.3535 ± 0.0478	0.0022 ± 0.0002
40	5	0.2187 ± 0.0033	0.0176 ± 0.0004	0.2798 ± 0.0096	0.0077 ± 0.0002
25	1	194.1618 ± 0.0911	0.0088 ± 0.0018	1.4920 ± 0.0965	0.0207 ± 0.0053
25	2	193.5228 ± 0.0115	0.0466 ± 0.0019	1.1904 ± 0.0239	0.0871 ± 0.0052
25	3	70.7659 ± 0.0744	0.0030 ± 0.0001	4.5183 ± 0.2157	0.0215 ± 0.0007
25	4	3.1566 ± 0.0128	0.0046 ± 0.0004	0.3022 ± 0.0364	0.0022 ± 0.0002
25	5	0.0295 ± 0.0028	0.0216 ± 0.0004	0.3221 ± 0.0079	0.0109 ± 0.0002

Fit is a Lorentzian curve as defined by $f\left(x;\, x_0, \gamma, I\right) = I\left[\frac{\gamma^2}{4(x-x_0)^2+\gamma^2}\right]$.
γ is the full-width at half maximum (FWHM).

Table C.5: Fit parameters for the 10% lipid suspension

T [°C]	peak number	x_0 [ppm]	I [arb]	γ [ppm]	*area* [arb]
25	1	194.9105 ± 0.0303	0.0351 ± 0.0063	0.7217 ± 0.0158	0.0398 ± 0.0076
25	2	194.6823 ± 0.0044	0.1265 ± 0.0066	0.5119 ± 0.0110	0.1017 ± 0.0074
25	3	72.7815 ± 0.0902	0.0031 ± 0.0001	4.5148 ± 0.2615	0.0218 ± 0.0009
25	4	3.1103 ± 0.0162	0.0041 ± 0.0005	0.2555 ± 0.0455	0.0016 ± 0.0002
25	5	0.1207 ± 0.0044	0.0189 ± 0.0004	0.4099 ± 0.0125	0.0122 ± 0.0003
5	1	195.7666 ± 0.0507	0.0182 ± 0.0023	1.2649 ± 0.0436	0.0361 ± 0.0055
5	2	195.2690 ± 0.0057	0.0830 ± 0.0025	0.8670 ± 0.0151	0.1131 ± 0.0053
5	3	70.9397 ± 0.0763	0.0036 ± 0.0001	4.5688 ± 0.2214	0.0256 ± 0.0009
5	4	0.2930 ± 0.0103	0.0316 ± 0.0012	0.5243 ± 0.0146	0.0260 ± 0.0015
5	5	0.0280 ± 0.0074	0.0190 ± 0.0015	0.2995 ± 0.0257	0.0089 ± 0.0014
10	1	196.3453 ± 0.0824	0.0173 ± 0.0043	1.7479 ± 0.0966	0.0476 ± 0.0143
10	2	195.7041 ± 0.0572	0.0268 ± 0.0043	1.8123 ± 0.0557	0.0763 ± 0.0144
10	3	69.6838 ± 0.0887	0.0028 ± 0.0001	4.4722 ± 0.2572	0.0194 ± 0.0008
10	4	2.9763 ± 0.0103	0.0056 ± 0.0005	0.2462 ± 0.0284	0.0022 ± 0.0002
10	5	-0.0699 ± 0.0032	0.0198 ± 0.0004	0.3027 ± 0.0091	0.0094 ± 0.0002
15	1	195.8785 ± 0.0721	0.0242 ± 0.0083	1.2217 ± 0.0564	0.0464 ± 0.0179
15	2	195.5016 ± 0.0333	0.0472 ± 0.0084	1.1609 ± 0.0366	0.0861 ± 0.0178
15	3	70.5488 ± 0.0690	0.0035 ± 0.0001	3.8704 ± 0.1993	0.0213 ± 0.0008
15	4	3.0212 ± 0.0116	0.0054 ± 0.0005	0.2616 ± 0.0331	0.0022 ± 0.0002
15	5	0.0810 ± 0.0040	0.0215 ± 0.0004	0.4806 ± 0.0113	0.0162 ± 0.0003
20	1	195.7534 ± 0.0731	0.0107 ± 0.0024	1.1089 ± 0.0844	0.0186 ± 0.0054
20	2	195.2631 ± 0.0066	0.0878 ± 0.0025	0.9426 ± 0.0124	0.1300 ± 0.0053
20	3	70.8594 ± 0.0732	0.0036 ± 0.0001	4.4767 ± 0.2121	0.0250 ± 0.0009
20	4	0.0096 ± 0.0061	0.0168 ± 0.0013	0.2521 ± 0.0257	0.0066 ± 0.0011
20	5	0.2680 ± 0.0088	0.0339 ± 0.0010	0.5376 ± 0.0120	0.0286 ± 0.0013

Fit is a Lorentzian curve as defined by $f\left(x;\ x_0, \gamma, I\right) = I\left[\frac{\gamma^2}{4(x-x_0)^2+\gamma^2}\right]$.
γ is the full-width at half maximum (FWHM).

Table C.6: Fit parameters for saturation curves of the 1% lipid suspension

saturation	peak number	x_0 [ppm]	I [arb]	γ [ppm]	*area* [arb]
off res.	1	191.8017 ± 0.0128	0.3061 ± 0.0026	2.3098 ± 0.0362	1.1105 ± 0.0152
off res.	2	190.0614 ± 0.0016	1.0000 ± 0.0050	0.6569 ± 0.0060	1.0319 ± 0.0089
off res.	3	69.1324 ± 0.0850	0.0514 ± 0.0017	4.9751 ± 0.2588	0.4013 ± 0.0154
off res.	4	59.1155 ± 0.0738	0.0442 ± 0.0023	2.8092 ± 0.2215	0.1950 ± 0.0114
sym. right	1	191.7932 ± 0.0150	0.2547 ± 0.0025	2.2840 ± 0.0423	0.9137 ± 0.0149
sym. right	2	190.0735 ± 0.0019	0.8422 ± 0.0047	0.6776 ± 0.0070	0.8963 ± 0.0089
sym. right	3	69.0006 ± 0.1057	0.0449 ± 0.0015	6.1019 ± 0.3307	0.4304 ± 0.0175
sym. right	4	59.4181 ± 0.0827	0.0381 ± 0.0022	2.7826 ± 0.2544	0.1665 ± 0.0116
right	1	192.4186 ± 0.0146	0.1777 ± 0.0021	2.2984 ± 0.0454	0.6414 ± 0.0097
right	2	190.1321 ± 0.0211	0.0576 ± 0.0041	0.5857 ± 0.0685	0.0530 ± 0.0051
right	3	70.0912 ± 0.1528	0.0205 ± 0.0016	3.8244 ± 0.4791	0.1231 ± 0.0119
right	4	60.9283 ± 0.2883	0.0127 ± 0.0014	5.1302 ± 0.9080	0.1024 ± 0.0139
center	1	191.9382 ± 0.0255	0.1192 ± 0.0020	2.3475 ± 0.0743	0.4394 ± 0.0118
center	2	190.0761 ± 0.0034	0.3921 ± 0.0039	0.6715 ± 0.0120	0.4135 ± 0.0069
center	3	69.1151 ± 0.1591	0.0245 ± 0.0013	6.0207 ± 0.4960	0.2320 ± 0.0143
center	4	59.7784 ± 0.1502	0.0164 ± 0.0020	2.4964 ± 0.4595	0.0645 ± 0.0090
*center	5	0.0000 ± 0.0208	0.0441 ± 0.0052	0.3505 ± 0.0591	0.0243 ± 0.0029
left	1	193.6700 ± 0.0443	0.0426 ± 0.0024	1.5925 ± 0.1293	0.1066 ± 0.0062
left	2	190.0320 ± 0.0171	0.0651 ± 0.0040	0.5538 ± 0.0493	0.0567 ± 0.0036
sym. left	1	191.7457 ± 0.0189	0.2294 ± 0.0024	2.5414 ± 0.0488	0.9157 ± 0.0162
sym. left	2	190.0949 ± 0.0021	0.7249 ± 0.0049	0.6365 ± 0.0082	0.7248 ± 0.0092
sym. left	3	69.2038 ± 0.0955	0.0445 ± 0.0017	5.0257 ± 0.2950	0.3511 ± 0.0154
sym. left	4	59.3794 ± 0.1224	0.0284 ± 0.0020	3.4278 ± 0.3746	0.1532 ± 0.0126

Fit is a Lorentzian curve as defined by $f(x;\, x_0, \gamma, I) = I\left[\frac{\gamma^2}{4(x-x_0)^2+\gamma^2}\right]$.
γ is the full-width at half maximum (FWHM).

* This peak is used as a chemical shift reference for all other fitted peaks in Tables C.1–C.6. By convention, the Xe_{gas} peak is set to 0 ppm.

Appendix D

Matlab code: Exponential Decay Fitting

To fit the saturation profiles for the MS2CA data (Chapter 8), each experiment (a specific concentration and either off or on resonant saturation) is processed using NMRPipe to produce spectral data. Those files are listed in `List of fit files and parameters.m`, along with the final fit parameters (determined after the application of the following code).

`List of fit files and parameters.m`

```
%% onresonant 700 pM
mainpath='/Users/tyler/Documents/Research/Data/Capsids/MS2_data_May_2009/';
subpath = 'Raw_data/18may2009_1_Xe_125nM_MS2cage_37C_onres.fid/';
filename = '18may2009_1.txt';
savefilepath = 'Matlab Fits/18may2009_1_fitresults';
pulsetime = 0.0005628; %pulse time (s)
delaytime = 0.0094482; %ipdelay time (s)


End: tau = 14.160580 +/- 0.464900
     y0 = -0.002678 +/- 0.029454
     A = 3060922.831337 +/- 80144.228318


%% offresonant 700 pM
mainpath='/Users/tyler/Documents/Research/Data/Capsids/MS2_data_May_2009/';
subpath = 'Raw_data/18may2009_2_Xe_125nM_MS2cage_37C_offres.fid/';
filename = '18may2009_2.txt';
savefilepath = 'Matlab Fits/18may2009_2_fitresults';
pulsetime = 0.0005628; %pulse time (s)
delaytime = 0.0094482; %ipdelay time (s)

End: tau = 28.241128 +/- 1.015820
     y0 = 0.000696 +/- 0.021126
     A = 2973625.685989 +/- 60511.176511


```

```
%% onresonant 70 pM
mainpath='/Users/tyler/Documents/Research/Data/Capsids/MS2_data_May_2009/';
subpath = 'Raw_data/18may2009_7_Xe_12.5nM_MS2cage_37C_onres3.fid/';
filename = '18may2009_7.txt';
savefilepath = 'Matlab Fits/18may2009_7_fitresults';
pulsetime = 0.00113; %pulse time (s)
delaytime = 0.00137; %ipdelay time (s)

End: tau = 19.158433 +/- 0.714650
     y0 = -0.000587 +/- 0.028274
     A = 2674439.680768 +/- 70166.775630


%% offresonant 70 pM
mainpath='/Users/tyler/Documents/Research/Data/Capsids/MS2_data_May_2009/';
subpath = 'Raw_data/18may2009_8_Xe_12.5nM_MS2cage_37C_offres3.fid/';
filename = '18may2009_8.txt';
savefilepath = 'Matlab Fits/18may2009_8_fitresults';
pulsetime = 0.00113; %pulse time (s)
delaytime = 0.00137; %ipdelay time (s)

End: tau = 32.168898 +/- 1.378929
     y0 = -0.001230 +/- 0.022909
     A = 2654675.220080 +/- 59125.374847


%% onresonant 7 pM
mainpath='/Users/tyler/Documents/Research/Data/Capsids/MS2_data_May_2009/';
subpath = 'Raw_data/18may2009_13_Xe_1.25nM_MS2cage_40C_onres.fid/';
filename = '18may2009_13.txt';
savefilepath = 'Matlab Fits/18may2009_13_fitresults';
pulsetime = 0.00094; %pulse time (s)
delaytime = 0.0; %ipdelay time (s)

End: tau = 23.346154 +/- 0.957856
     y0 = -0.002918 +/- 0.027427
     A = 3712750.588510 +/- 96819.207414


%% offresonant 7 pM
mainpath='/Users/tyler/Documents/Research/Data/Capsids/MS2_data_May_2009/';
subpath = 'Raw_data/18may2009_12_Xe_1.25nM_MS2cage_40C_offres.fid/';
filename = '18may2009_12.txt';
savefilepath = 'Matlab Fits/18may2009_12_fitresults';
pulsetime = 0.00094; %pulse time (s)
delaytime = 0.0; %ipdelay time (s)

End: tau = 31.615209 +/- 1.357087
     y0 = -0.001489 +/- 0.023237
     A = 3926248.907139 +/- 88630.514488


%% onresonant 0.7 pM
mainpath='/Users/tyler/Documents/Research/Data/Capsids/MS2_data_May_2009/';
subpath = 'Raw_data/18may2009_15_Xe_125pM_MS2cage_40C_onres.fid/';
filename = '18may2009_15.txt';
savefilepath = 'Matlab Fits/18may2009_15_fitresults';
pulsetime = 0.00094; %pulse time (s)
delaytime = 0.0; %ipdelay time (s)

```

```
End: tau = 27.756113 +/- 1.137229
     y0 = -0.001418 +/- 0.024343
     A = 2724618.654268 +/- 63891.331726


%% offresonant 0.7 pM
mainpath='/Users/tyler/Documents/Research/Data/Capsids/MS2_data_May_2009/';
subpath = 'Raw_data/18may2009_16_Xe_125pM_MS2cage_40C_offres.fid/';
filename = '18may2009_16.txt';
savefilepath = 'Matlab Fits/18may2009_16_fitresults';
pulsetime = 0.00094; %pulse time (s)
delaytime = 0.0; %ipdelay time (s)

End: tau = 31.896691 +/- 1.168122
     y0 = -0.000605 +/- 0.019697
     A = 2770345.306137 +/- 53001.102906


%% onresonant buffer
mainpath='/Users/tyler/Documents/Research/Data/Capsids/MS2_data_May_2009/';
subpath = 'Raw_data/18may2009_21_Xe_buffer_40C_onres.fid/';
filename = '18may2009_21.txt';
savefilepath = 'Matlab Fits/18may2009_21_fitresults';
pulsetime = 0.00094; %pulse time (s)
delaytime = 0.0; %ipdelay time (s)

End: tau = 36.852098 +/- 2.229401
     y0 = -0.000563 +/- 0.029093
     A = 2963820.137016 +/- 84503.048751


%% offresonant buffer
mainpath='/Users/tyler/Documents/Research/Data/Capsids/MS2_data_May_2009/';
subpath = 'Raw_data/18may2009_22_Xe_buffer_40C_offres.fid/';
filename = '18may2009_22.txt';
savefilepath = 'Matlab Fits/18may2009_22_fitresults';
pulsetime = 0.00094; %pulse time (s)
delaytime = 0.0; %ipdelay time (s)

End: tau = 36.431538 +/- 1.505525
     y0 = -0.000226 +/- 0.020042
     A = 2992824.112759 +/- 58744.665129
```

The next four files are used in `startToFit.m` and are presented here for completeness. `readpar.m`

```
function p=readpar(filename,parname)

   %reads a parameter from vnmr parameter file
   %filename= path to vnmr procpar file
   %parname= name of parameter to read
   %p= returned parameter value

   f=fopen(filename,'r','b');
   line=fgetl(f);
   while (~strncmp(line,parname,length(parname)))&(~feof(f))
       line=fgetl(f);
   end
```

```
13      line=fgetl(f);
14      fclose(f);
15
16      secondnum=sscanf(line,'%d');
17      p=secondnum;
18  end
```

exponential1.m

```
1  % This function fits the data to an exponential with no y-axis shift, but
2  % only a scaling factor A and a decay constant tau.
3  function [y]=fun(v,x)
4  %y0=v(1);
5  A=v(1);
6  tau=v(2);
7  y=(A).*(exp(-x./tau));
```

exponential2.m

```
1  % This function fits the data to an exponential with no scaling factor, but
2  % only a y-axis offset y0 and a decay constant tau.
3  function [y]=fun(v,x)
4  y0=v(1);
5  tau=v(2);
6  y=y0 + (exp(-x./tau));
```

exponential3.m

```
1  % This function fits the data to an exponential with no y-axis shift nor
2  % scaling factor, but only a decay constant tau.
3  function [y]=fun(v,x)
4  tau=v(1);
5  y=(exp(-x./tau));
```

Once the spectral data has been generated, the `startToFit.m` file is amended to reflect the particular data set for fitting (lines 15–23).

startToFit.m

```
1  %Fit saturation profiles for MS2CA data to exponential decay functions.
2  %The data should already be processed into spectral format, rather than
3  %raw, Varian FIDs. This is typically done in NMRPipe.
4  %Remember to set the working directory to
5  %/Users/tyler/Documents/Research/Data/Capsids/MS2_data_May_2009/Matlab Fits
6
7  clear;
8  clc;
9  close all;
10
11 %% user-input values
12 % NOTE: Use the info in the file "List of fits and parameters.m" to get a
13 %quick listing of all the directories and the filenames for the MS2CA data.
14
```

```
15 %These reflect the data sets in the file "List of fits and parameters.m".
16 mainpath='/Users/tyler/Documents/Research/Data/Capsids/MS2_data_May_2009/';
17 subpath = 'Raw_data/18may2009_1_Xe_125nM_MS2cage_37C_onres.fid/';
18 filename = '18may2009_1.txt';
19 savefilepath = 'Matlab Fits/18may2009_1_fitresults';
20
21 % These values are manually entered from the pulse sequence.
22 pulsetime = 0.0005628; %pulse time (s)
23 delaytime = 0.0094482; %ipdelay time (s)
24
25
26 %% load data, read parameters
27 %Take the location of the data.
28 fullpath = strcat(mainpath,subpath,filename);
29 parname = strcat(mainpath,subpath,'procpar');
30 savefilename = strcat(mainpath,savefilepath);
31
32 % Use the file location and the script "readpar.m" to extract the number
33 % of satcycles in the saturation period.
34 satcycle = readpar(parname,'satcycle');
35
36 %omit first dummy value from VNMR's procpar output
37 satcycle = satcycle(2:size(satcycle(:,1)));
38
39 %total saturation time including ipdelays
40 sattime = (pulsetime + delaytime) * satcycle;
41
42 %Load the spectra data and rearrange it into appropriate matrices.
43 data=load(fullpath,'-ascii');
44 data2=data(:,3);
45
46 %Number of points
47 np = max(size(sattime));
48 pts = max(size(data2(:,1)))/np;
49
50 %Split into individual spectra.
51 data3=reshape(data2,pts,np);
52
53 %Find largest signal...
54 [C,I] = max(data3);
55 %...and integrate around it +/- 250 pts to get the integrated value
56 %of the Xe(aq) peak.
57 data4=squeeze(sum(data3((I(1)-250):(I(1) + 250),:)));
58 data4 = data4';
59
60 %% initial fit of raw points to get scaling
61 %data4 is the integrated signals as a function of saturation time. Make
62 %this the starting data set.
63 yOrig=data4;
64
65 %Make guesses at fit parameters. A is likely to be the amplitude of the
66 %first point.
67 A=max(yOrig);
68 tau=10; %this is totally random
69
70 %The initial fit parameter guesses.
71 vStart=[A,tau];
72
73 %Calculate data at appropriate saturation times using guessed fit
74 %parameters.
```

```
75  yStart=exponential1(vStart,sattime);
76
77  %Run the non-linear fitting routine using exponential1 (amplitude and
78  %tau), to get a first estimate of the scaling parameter A.
79  [vEnd, r, J, COVB, mse] = nlinfit(sattime,yOrig,@exponential1,vStart);
80
81  % Calculate data using these new parameters.
82  yEnd=exponential1(vEnd,sattime);
83
84  %Determine 90% confidence intervals for these parameters. This is only
85  %useful for A. The confidence interval can be changed by changing the last
86  %value--enter 1-(desired c.i.). Here, 0.1 is entered.
87  ci = nlparci(vEnd, r, 'covar', COVB,'alpha',0.1);
88
89  %Store the scaling value A as scaling and the +/- value as scalingError
90  scaling = vEnd(1);
91  scalingError = abs((ci(1,1)-ci(1,2))/2);
92
93  % scale data to max fit height
94  data5 = data4 ./ vEnd(1);
95
96  %% refit with y-offset
97  %start next fitting segment with scaled data
98  yOrig=data5;
99
100 %Enter new guesses for fit parameters
101 y0=0;
102 tau=10;
103 vStart=[y0,tau];
104
105 %Calculate data at appropriate saturation times using guessed fit
106 %parameters.
107 yStart=exponential2(vStart,sattime);
108
109 %Run the non-linear fitting routine using exponential2 (y0 and
110 %tau), to get an estimate of the y-shift, y0.
111 [vEnd, r, J, COVB, mse] = nlinfit(sattime,yOrig,@exponential2,vStart);
112
113 % Calculate data using these new parameters.
114 yEnd=exponential2(vEnd,sattime);
115
116 %Determine 90% confidence intervals for these parameters. This is only
117 %useful for y0. The confidence interval can be changed by changing the last
118 %value--enter 1-(desired c.i.). Here, 0.1 is entered.
119 ci = nlparci(vEnd, r, 'covar', COVB,'alpha',0.1);
120
121 %Store the shift value y0 as shift and the +/- value as shiftError
122 shift = vEnd(1);
123 shiftError = abs((ci(1,1) - ci(1,2)) / 2);
124
125 % shift data vertically
126 data6 = data5 - shift;
127
128 %% fit for tau
129 % start next fitting segment with scaled and shifted data
130 yOrig=data6;
131
132 %Enter new guesses for fit parameters
133 tau=10;
134 vStart=[tau];
```

```
135
136 %Calculate data at appropriate saturation times using guessed fit
137 %parameters.
138 yStart=exponential3(vStart,sattime);
139
140 %Run the non-linear fitting routine using exponential3 (tau only),
141 %to get a value for the decay constant, tau.
142 [vEnd, r, J, COVB, mse] = nlinfit(sattime,yOrig,@exponential3,vStart);
143
144 % Calculate data using these new parameters.
145 yEnd=exponential3(vEnd,sattime);
146
147 %Determine 90% confidence intervals for these parameters. This is only
148 %useful for tau. The confidence interval can be changed by changing the
149 %last value--enter 1-(desired c.i.). Here, 0.1 is entered.
150 ci = nlparci(vEnd, r, 'covar', COVB,'alpha',0.1);
151
152 %Store the decay constant tau as tauvalue
153 %and the +/- value as tauvalueError
154 tauvalue = vEnd(1);
155 tauvalueError = abs((ci(1,1) - ci(1,2))/2);
156
157 %% final results and plotting
158 %Make a final array containing the saturation time, the experimental data,
159 %the calculated data, plus the high-error and the low-error. Save this
160 %with the savefilename from above as an ascii text file.
161 finalFit = [sattime, data6, yEnd, yEnd - shiftError, yEnd + shiftError];
162 save(strcat(savefilename,'.txt'),'finalFit','-ascii');
163
164 %Make a final array the fit parameters and their errors. Append this
165 %to the savefilename from above as an ascii text file.
166 fitparams= [tauvalue, tauvalueError;shift,shiftError;scaling,scalingError];
167 dlmwrite(strcat(savefilename,'.txt'),finalFit, 'delimiter', '\t');
168 dlmwrite(strcat(savefilename,'.txt'),fitparams,'-append','delimiter','\t');
```

This file outputs an ASCII text file that contains all the relevant fit parameters as well as model data. Each data set is fit to an exponential decay function

$$y = y_0 + A \cdot e^{-t_{sat}/\tau} \tag{D.1}$$

in three iterations. First, the data is fit for the scaling parameter, A. Then, after normalizing the data to A, it is fit to the y-offset, y_0. The shift is the applied to the data and it is fit to the decay parameter, τ. This stepwise fitting routine is done to prevent the fitting routine from underestimating the decay and overestimating the y-offset in the data.

Appendix E

Symbols and Physical Constants

Symbols and Abbreviations

B_0	amplitude of the static, external magnetic field
B_1	amplitude of the applied, transverse magnetic field
K	thermodynamic binding constant
N	population
p	pressure
P	polarization
T	temperature
T_1	longitudinal (spin-spin) relaxation time
T_2	transverse (spin-lattice) relaxation time
δ	chemical shift frequency
γ	gyromagnetic ratio
Ω	saturation bandwidth

CEST	chemical exchange saturation transfer
CNR	contrast-to-noise ratio
cw	continuous wave
FT	Fourier transform
hp	hyperpolarized
ppm	parts per million
rf	radiofrequency
SAR	specific absorption rate
SLM	standard liters per minute
SNR	signal-to-noise ratio

Physical Constants

h	$= 6.626\,076 \times 10^{-34}$	J·s
$\hbar$	$= 1.054\,572 \times 10^{-34}$	J·s
k_B	$= 1.380\,658 \times 10^{-23}$	J·K^{-1}
γ (^{1}H)	$= 42.576$	MHz·T^{-1}
	$= 2.6752 \times 10^{8}$	T^{-1}·s^{-1}
γ (^{129}Xe)	$= -11.777$	MHz·T^{-1}
	$= 7.3997 \times 10^{7}$	T^{-1}·s^{-1}
1 T	$= 10\,000$	G
1 psi	$= 51.714\,933$	torr
	$= 6894.757\,29$	Pa
	$= 0.068\,045\,96$	atm
1 atm	$= 14.695\,949$	psi
	$= 760$	torr
	$= 101\,325$	Pa
R	$= 0.082\,057\,46$	L·atm·mol^{-1}·K^{-1}
	$= 1.205\,912\,23$	L·psi·mol^{-1}·K^{-1}
	$= 62.363\,67$	L·torr·mol^{-1}·K^{-1}
	$= 8314.472\,135$	L·Pa·mol^{-1}·K^{-1}
B_1 (Hz)	$= B_{1,ref}$ (Hz) $\cdot 10^{\left(B_1\ (\mathrm{dB}) - B_{1,ref}\ (\mathrm{dB})\right)/20}$	
B_1 (dB)	$= B_{1,ref}\,(\mathrm{dB}) + 20 \cdot log\frac{B_1\,(\mathrm{Hz})}{B_{1,ref}(\mathrm{Hz})}$	